

**DEVELOPMENT AND VALIDATION OF MRI-GUIDED DELIVERY OF AGENTS  
WITHIN CONVENTIONAL CLOSED-BORE SCANNERS**

by

Miles E. Olsen

A dissertation submitted in partial fulfillment of  
the requirements for the degree of

Doctor of Philosophy

(Medical Physics)

at the

UNIVERSITY OF WISCONSIN–MADISON

2021

Date of final oral examination: 2021-12-13

Pending approval by the following members of the Final Oral Committee:

Azam S. Ahmed, Assistant Professor, Neurological Surgery

Andrew L. Alexander, Professor, Medical Physics

Walter F. Block, Professor, Medical Physics

M. Elizabeth Meyerand, Professor, Medical Physics

Oliver Wieben, Professor, Medical Physics

*To my family*

## ACKNOWLEDGMENTS

---

*This is your life! Right here! Right now!*

*It's real time, you hear me? Real time!*

*Time to get real [...]*

— LORNETTE 'MACE' MASON, *STRANGE DAYS* (1995)

I could not have done this without the support of my family and the encouragement from many teachers along the way. At Hellgate High School, Byron Anderson and John Gebert were pivotal in inspiring me to pursue physics and computer programming. Thank you, Keith Parker, for connecting me with my senior project advisor, James Jacobs.

As an undergraduate at the University of Montana, I received excellent guidance from my advisors in the Physics and Astronomy Department: Michael Schneider and the late James Jacobs. I wish I could see you again, Dr. J, to talk about some of the wild stuff that has happened over the past decade. My decision to go to graduate school was influenced by my enormously positive experiences in physics research at UM with James Jacobs, Jennifer Fowler, Michael Schneider, and Andrew Ware; as well as Justin Shaw at NIST–Boulder, who supervised me during my time in the Summer Undergraduate Research Fellowship program in 2008 and again on return trips to NIST–Boulder. Thank you all for giving me a taste of the responsibilities and satisfaction that can be had in physics research.

I am grateful for the opportunity to study at UW–Madison, where I have had many treasured interactions with friends, mentors, and labmates. In approximately chronological order: Doug Brugger, Anne Baldwin, Akire Trestrail, Ethan Brodsky, Eric Bultman, Dave Niles, Sam Hurley, John Garrett, Svyat Vergun, Larry Hernandez, Leah Henze-Bancroft, Fang Liu, Rajeev Chaudhary, Nade Sritanyaratana, Barbara Bendlin, Adrien Joyner, Marissa Riedel, Jonathan Oler, Rothem Kovner, Jorge Jimenez, master machinist Gary Frank, Michael Simonson, Rob and Amelia Fontella, Rafael and Erin Hastey, Xiaojue Zhou, Sasha Rosser, Drew Sheldon, and

Anthony and Lindsay Nonhof-Fisher. I am honored to have known you all, and proud to see you achieving success in your careers, academic and otherwise.

Thanks as well to the crew of WIMR MRI technologists who were involved in this work, especially Jenelle Grogan, Kelli Hellenbrand, and Sara John. Thank you to the veterinary and animal care staff who enable this research, especially Kevin Brunner (a kindred spirit in the year-round bicyclist club!) and Vicki Elam. A big thank you to Ned Kalin and Marina Emborg for the long, ongoing collaboration that has taught me so much and helped demonstrate to the world some of the amazing things that are possible with interventional MRI.

This work would never have happened without the funding from the Kinetics Foundation and the UW–Madison Clinical Neuroengineering Training Program, which supported me during the early years of my research here. Thank you for funding me but, more importantly, thank you for funding Parkinson’s disease research and many other promising graduate students, respectively. I also appreciate GE Healthcare’s institutional support given to UW–Madison.

Thank you to the members of my committee. At various times you have been my teachers, advisors, and research collaborators. I am thankful for your deep expertise, thoughtful questions, and patience with me as I navigated the challenges of graduate school. Thank you, Drs. Meyerand and Weiben, for your MRI courses; thank you, Dr. Ahmed, for making time in your very busy schedule to meet with me on so many occasions over the years; thank you, Dr. Alexander, for your ongoing collaboration on the DEV project; and thank you, Wally, for your indefatigable positive outlook and all that you have taught me.

Many thanks to the developers of Vurtigo, especially Labonny Biswas, and the developers of RTHawk, especially Juan Santos and William Overall, for helping me to better understand those large software platforms and get to a point where I could make changes to the source and build on them in order to carry out my research.

My parents, Donna and Roger, have given me their love and the gifts of literacy and inquisitiveness, which have been absolutely foundational to making me the person I am today. I thank my sister, Maria, for all her support but especially the

fridge magnets, which have turned out to be surprisingly motivating.

I owe my greatest thanks to my wife, Hilary Joyner, for her love, encouragement, and support that has enabled me to complete this dissertation. I'm looking forward to the next chapter in our lives, and seeing the person that Niels grows up to be.

## CONTENTS

---

Contents v

List of Tables vii

List of Figures viii

Nomenclature xi

Abstract xiii

**1 Introduction 1**

1.1 *Motivation* 1

1.2 *Objectives* 4

1.3 *Summary of work* 5

**2 Angiography for Neurosurgical Planning 7**

2.1 *Abstract* 7

2.2 *Imaging basal ganglia vasculature with bSSFP* 9

2.3 *Prevalence of enlarged perivascular spaces* 19

2.4 *Effect of bSSFP angiography on DBS plans* 26

**3 Computational Device Tracking 36**

3.1 *Abstract* 37

3.2 *Introduction* 38

3.3 *Methods* 42

3.4 *Results* 52

3.5 *Discussion* 54

3.6 *Conclusions* 58

3.7 *Acknowledgments* 58

3.8 *Figures and Tables* 60

3.9	<i>Supporting Figures and Tables</i>	70
4	<b>Intracerebral Hemorrhage Evacuation</b>	73
4.1	<i>Abstract</i>	73
4.2	<i>Feasibility Study of MRI-Guided ICH Evacuation</i>	75
4.3	<i>Hardware fabricated for in vitro and swine in vivo experiments</i>	79
5	<b>Conclusions and Recommendations for Future Work</b>	90
5.1	<i>Aim 1: preoperative angiography for planning</i>	90
5.2	<i>Aim 2: intraoperative trajectory guide tracking</i>	91
5.3	<i>Aim 3: model of intracerebral hemorrhage</i>	94
A	<b>Appendices</b>	97
A.1	<i>Surgical map and symbols</i>	97
A.2	<i>Machining conical adapters</i>	98
A.3	<i>Navigus models in OpenSCAD</i>	112
A.4	<i>Additional IMRI experiments</i>	120
	<b>Colophon</b>	147
	<b>Bibliography</b>	148

**LIST OF TABLES**

---

2.1	Demographic data of subjects analyzed. . . . .	21
2.2	Parameters of MRI sequences analyzed for presence of EPVS. . . . .	23
2.3	DBS planning MRI sequences. . . . .	26
2.4	Changes to DBS planning trajectories. . . . .	30



## LIST OF FIGURES

---

2.1	Target region within basal ganglia . . . . .	10
2.2	X-ray atlas of lenticulostriate arteries . . . . .	11
2.3	X-ray, bSSFP, and TOF of LSAs . . . . .	13
2.4	Axial comparison of bSSFP and TOF . . . . .	14
2.5	Near-coronal comparison of bSSFP and TOF . . . . .	15
2.6	Near-sagittal comparison of bSSFP and TOF . . . . .	15
2.7	bSSFP vs. TOF in one subject . . . . .	16
2.8	bSSFP vs. TOF in four subjects . . . . .	17
2.9	Example CED plan . . . . .	18
2.10	Infusate diversion during CED . . . . .	20
2.11	Example EPVS in human brain . . . . .	22
2.12	Comparison of normal subject and atypical subjects . . . . .	24
2.13	Coronal and axial views after adjusting left trajectory . . . . .	31
2.14	Sagittal view after moving entry point posterior . . . . .	33
3.1	Existing methods for neurosurgical device alignment vs. the proposed MR-based computational tracking. . . . .	60
3.2	Prospective stereotaxy method and trajectory guide hardware. . . . .	61
3.3	Computation of the stem-plane intersection. . . . .	62
3.4	Computation of a refined pivot point. . . . .	63
3.5	Determination of tip placement error. . . . .	64
3.6	Preoperative plans for gene delivery into amygdala and cell delivery into substantia nigra. . . . .	65
3.7	In vitro precision and accuracy. . . . .	66
3.8	In vivo pivot computation and predicted inaccuracy. . . . .	67
3.9	Visualization of gene delivery infusions. . . . .	68
3.10	Visualization of cell delivery process. . . . .	69
3.11	NMR sample tubes and adapter cones used in place of original plastic alignment stems. . . . .	70

3.12	Example of a surgical map used for placing bases. . . . .	71
3.13	Geometric explanation of error distribution in pivot computation. . . . .	72
4.1	Vision for MR-Guided ICH Evacuation. . . . .	76
4.2	In vitro feasibility study of plasma extraction. . . . .	77
4.3	Assorted TPA delivery methods. . . . .	78
4.4	MR-compatible cannula with interchangeable tips. . . . .	80
4.5	Closeup of MR-compatible cannula and tips. . . . .	81
4.6	Poseable arms to hold fiducials during swine IMRI. . . . .	83
4.7	Tool for marking burr hole perimeter on swine skull. . . . .	85
4.8	Remote introducer. . . . .	86
4.9	Linear stage. . . . .	87
4.10	New introducer hardware. . . . .	88
4.11	New introducer hardware (close up). . . . .	89
A.1	Blank surgical map template. . . . .	97
A.2	A finished conical adapter on an NMR tube. . . . .	98
A.3	Suggested materials for machining adapters. . . . .	99
A.4	Face off end of stock, then center drill. . . . .	100
A.5	Drill with #45 bit, then #32. . . . .	101
A.6	Reduce outer diameter. . . . .	102
A.7	Set angle of top slide to achieve desired taper. . . . .	103
A.8	Cut off with parting tool. . . . .	104
A.9	Reverse part in collet, face off. . . . .	105
A.10	Remove from collet, finish drilling by hand. . . . .	106
A.11	Test fit with NMR tube. . . . .	107
A.12	Apply radial pressure at level of binding spots. . . . .	108
A.13	Test concentricity error. . . . .	109
A.14	Rendering of orthogonal Navigus base in OpenSCAD. . . . .	112
A.15	Rendering of angled Navigus base in OpenSCAD. . . . .	113
A.16	Block2019 Fig. 1 . . . . .	128
A.17	Block2019 Fig. 2 . . . . .	129

A.18 Block2019 Fig. 3 . . . . .	129
A.19 Block2019 Fig. 4 . . . . .	130
A.20 Block2019 Fig. 5 . . . . .	131
A.21 Brady2018 Fig. 1 . . . . .	135
A.22 Brady2018 Fig. 2 . . . . .	136
A.23 Brady2018 Fig. 3 . . . . .	137
A.24 Brady2018 Fig. 4 . . . . .	138
A.25 Brady2018 Fig. 5 . . . . .	139
A.26 Olsen2017 Fig. 1 . . . . .	143
A.27 Olsen2017 Fig. 2 . . . . .	144
A.28 Olsen2017 Fig. 3 . . . . .	144
A.29 Olsen2017 Fig. 4 . . . . .	145

**DISCARD THIS PAGE**

## NOMENCLATURE

---

AAV	Adeno-associated virus
AT	Anxious temperament
bSSFP	Balanced steady-state free precession
Cannula	Rigid tube inserted into the body for administration or removal of fluid (essentially a needle)
CED	Convection-enhanced delivery
CT	(X-ray) computed tomography
DBS	Deep brain stimulation
DREADDs	Designer receptors exclusively activated by designer drugs
EPVS	Enlarged perivascular space(s)
FLAIR	Fluid-attenuated inversion recovery
fMRI	Functional magnetic resonance imaging
FOV	Field of view
Gd	Gadolinium (contrast agent used in MRI)
GPI	Internal globus pallidus
ICH	Intracerebral hemorrhage
IMRI	Interventional magnetic resonance imaging
IPSC	Induced pluripotent stem cell
IR	Inversion recovery
LSA	Lenticulostriate artery

MISTIE	Minimally invasive surgery plus alteplase for intracerebral hemorrhage evacuation
MRI	Magnetic resonance imaging
NHP	Non-human primate
OR	Operating room
PD	Parkinson's disease
PET	Positron emission tomography
PFC	Prefrontal cortex
PVS	Perivascular space(s)
RF	Radio frequency
ROI	Region of interest
SN	Substantia nigra
SNR	Signal to noise ratio
SPGR	Spoiled gradient recalled
SSFP	Steady-state free precession
$T_1, T_2$	Longitudinal and transverse relaxation times
$T_1w, T_2w$	$T_1$ - and $T_2$ -weighted image contrast
$T_E, T_R, T_I$	Echo, repetition, and inversion times in MRI
TOF	Time of flight
TPA	Tissue plasminogen activator

## ABSTRACT

---

Most clinical neurosurgeries today are performed without intraoperative tomographic imaging, instead relying on preoperative images which may be hours or days old. An optical tracking system, used in the operating room while aiming interventional devices, renders updates of the predicted trajectory on the preoperative image by repeatedly measuring fiducials on the device and patient's head. This technique rests on the assumption that the brain does not shift inside the skull, but brain shift is observed. For procedures like biopsy of large tumors, this is acceptable because the shift is much smaller than the target size.

When targets are small and interventional devices must be placed very accurately, as in the studies we undertake in this work, the standard method is inadequate. The surgeries we focus on are: implantation of deep brain stimulation (DBS) electrodes, infusion of viral vectors carrying gene-therapy payloads, injection of neural progenitor cells, and intracerebral hemorrhage (ICH) evacuation by administration of thrombolytic drugs directly into clot.

The main findings of this work are: Perforating vessels of the basal ganglia are depicted well by bSSFP imaging (compared to TOF), have an enlarged appearance in 12% of the subpopulation near the age of typical Parkinson's disease onset (50–70 years), and influence the choice of trajectories when planning functional neurosurgeries such as DBS lead placement.

Complex and previously unachievable surgical goals are enabled by the development of a physically accurate method for preoperative planning of IMRI-guided surgeries. A computational approach to neurosurgical trajectory guide tracking (rather than an approach based on human interpretation of images) enables rapid interactive feedback, decreased subjectivity, and accurate aiming of the trajectory guide. The usefulness of the preoperative planning and IMRI device tracking methods are borne out by several preclinical studies (totaling over 80 IMRI neurosurgeries to date) in gene delivery, cell delivery, infusion monitoring, and causal fMRI.

In clotting blood, MRI is capable of sensing different contrast mechanisms than

CT (the standard modality used during intracerebral hemorrhage monitoring) and in vitro models of IMRI-guided clot lysing suggest there is value in applying IMRI to preclinical in vivo ICH evacuation studies.



## 1 INTRODUCTION

---

### 1.1 Motivation

In the domain of neurosurgery, magnetic resonance imaging (MRI) offers some noteworthy advantages over other modalities. Namely soft tissue contrast, the use of non-ionizing radiation, ability to penetrate the skull and ability to interrogate microscale properties of tissue depending on the MR sequence used. X-ray computed tomography (CT) and ultrasound enjoy some, but not all of these capabilities. MRI is not always used to its full potential in imaging for preoperative planning, however, and intraoperative MRI (IMRI) is especially difficult, with conventional diagnostic MRI systems being cramped and open/interventional MRI systems having drawbacks in image quality and cost. In this work, we aim to develop and demonstrate techniques and hardware that are useful for preoperative planning and intraoperative MRI monitoring of neurosurgeries.

The task of delivering agents to precise locations within the brain has been of interest to neuroscience researchers for decades. The technique of convection-enhanced delivery (CED) has emerged as a viable method for introducing agents to the parenchyma of an intact brain *in vivo* [1]. CED uses a constant gradual infusion (on the order of microliters/minute), through a cannula (essentially a hollow needle) inserted into the target tissue, driven by a mechanical pump to achieve more uniform distribution of agents than injection. Diffusion alone, with no pressure gradient, is insufficient to carry large agents far from their source, and injecting too quickly will push brain matter out of the way and subject the closest

cells to dangerous levels of pressure. In CED, injecting slowly and maintaining a pressure gradient allows for even high molecular weight agents to convect out farther from the source (the tip of a cannula in this case).

CED was developed, and much research has so far been conducted, with open end-port cannulas. The expectation is that in uniform tissue, the infusate distribution would grow in an approximately spherical shape around the tip of the cannula. Most tissue is not uniform, however, and the local microstructure has a large effect on fluid transport, such as increased advection along white matter tracts compared to within gray matter. If the infusion expands to reach an anatomical feature with high hydraulic conductivity (such as the perivascular spaces PVS surrounding blood vessels), the feature can act as a shunt pathway that diverts infusate and strongly affects the shape of the final infusate distribution. Preoperative imaging alone is insufficient to fully characterize these features and accurately predict the infusate distribution. More recent experiments are underway to characterize the behavior of multi-port or porous-tipped cannulas, which may offer better infusate distribution given the reality of heterogeneous tissue.

Intraoperative MRI enables the monitoring of gadolinium-doped infusate as it is delivered, which can be used as feedback to update models predicting the final infusate distribution [0]. The brain interstitial space is approximately 50 nm [2], easily permitting passage of the gadolinium contrast agent molecules (approx 1 nm), but good concordance has been observed between gadolinium signal shown on IMRI and expression of genes delivered by the larger AAV2 viral vector (approx 25 nm [3]) shown by histological staining and microscopy [0]. The challenge in CED is not

getting the agent to move with the infusate vehicle, but to ensure that the infusion cloud covers the intended target without unwanted diversion.

During deep brain stimulation (DBS) electrode implantation surgeries, the trajectories of inserted leads are likely to pass through the shrub-like formation of the lenticulostriate arteries (LSAs) in the putamen. It is possible that damage to these vessels is responsible for some of the rate of hematoma complications observed in DBS implantation surgeries (3.3% chance of hematoma per electrode insertion in a study of 481 total lead implantations [4]). Striking one of the perforating LSAs during a functional neurosurgery (or infusing near them during CED) is undesirable, and we propose an imaging method that may be used to plan surgeries so as to avoid striking these vessels.

To avoid missing small targets during neurosurgery, it is necessary to

- install interventional hardware on the skull such that the target falls within the reachable volume defined by the range of motion limits of the hardware.
- accurately identify the target location with as little delay as possible before device insertion (unlike current standard in neurosurgery, using imagery that is hours- or days-old)
- and accurately track the interventional device as it is aimed, to ensure it is aligned with the target, which is difficult in the scanner bore using conventional optical tracking means.

We present methods for preoperative planning and MR-based trajectory guide tracking to address these concerns.

Intracerebral hemorrhage (ICH) is the type of stroke with the highest mortality rate, and patient outcomes improve with prompt and thorough debulking of clot volume. MRI is positioned to offer preoperative planning and intraoperative monitoring information that cannot be obtained with conventional X-ray CT guidance now used clinically. We developed and tested hardware for in vitro and in vivo swine experiments relevant to intracerebral hemorrhage evacuation.

This work paves the way for further refinement of MRI sequences and protocols used for preoperative planning in functional neurosurgery and ICH evacuation procedures, and it demonstrates the development of successful methods for preoperative planning and intraoperative device tracking, as applied in preclinical gene and cell delivery neurosurgeries.

## 1.2 Objectives

We aim to provide MRI sequences and planning techniques that are useful in the realms of functional neurosurgery, gene- and cell-delivery, and ICH evacuation. Our specific aims are:

- 1. To carry out a study to determine whether bSSFP imagery of small scale vasculature will cause neurosurgeons to alter their DBS insertion plans once unblinded to bSSFP images.**
- 2. To develop and validate real-time imaging software and pulse sequences suitable for rapidly and accurately aligning a trajectory guide during device insertion procedures.**

- 3. To develop an in-vitro model of intracerebral hemorrhage and corresponding MR protocol to collect structural measures used to predict distribution of clot lysing drug injected directly into clot during minimally invasive surgery.**

Recommended future work includes a small study using high resolution angiography for planning surgeries of actual DBS patients; streamlining the task of preoperative planning for IMRI neurosurgeries; continuation of preclinical IMRI neurosurgeries for ongoing and upcoming projects (with the Parkinson's Disease Research Program, Department of Psychiatry, and off-campus collaborators); optimizing the IMRI protocol to reduce imaging time and procedure duration; and further exploration of new methods for delivery and monitoring of clot lysing agents.

## **1.3 Summary of work**

**Chapter 2:** Perforating vessels of the basal ganglia are better depicted by bSSFP imaging than TOF, have an enlarged appearance at the region of interest in 12% of subjects examined, and influence the choice of trajectories when planning functional neurosurgeries.

**Chapter 3:** A computational approach to neurosurgical trajectory guide tracking (rather than an approach based on human interpretation of images) enables rapid interactive feedback, decreased subjectivity, and accurate aiming of the trajectory guide.

**Chapter 4:** In clotting blood, MRI is capable of sensing different contrast mechanisms than CT—the standard modality used during intracerebral hemorrhage (ICH) monitoring—and in vitro models of IMRI-guided clot lysing suggest there is value in applying IMRI to preclinical in vivo ICH evacuation studies.

**Chapter 5:** Conclusions and recommendations for future work.

## 2 ANGIOGRAPHY FOR NEUROSURGICAL PLANNING

---

In this chapter I describe the use of a balanced steady-state free precession (bSSFP) sequence to image small, low-flow, deep vessels in the brain; a study of the prevalence of enlarged perivascular spaces (EPVS) in a cohort with age similar to that of Parkinson's disease onset; and a small exploratory trial to gauge whether unblinding a neurosurgeon to bSSFP imagery of the lenticulostriate arteries (LSAs) would result in adjustments to the trajectories for deep brain stimulation (DBS) electrode insertion.

Portions of this chapter have previously been presented as posters at the 2012 and 2013 ISMRM annual meetings:

- **Miles Olsen**, Benjamin Grabow, Ethan Brodsky, Karl Sillay, Andy Alexander, Labonny Biswas, Roey Flor, Perry Radau, Graham Wright, and Walter Block. "Imaging Tasks Useful in Convection-enhanced Drug Delivery in the Brain: Depicting Distal Cerebral Vasculature". In: *the 20th Annual Meeting of the International Society for Magnetic Resonance in Medicine*. Poster #1595. 2012
- **Miles Olsen**, Barbara Bendlin, Sterling Johnson, Jason Huston, Benjamin Grabow, Ethan Brodsky, and Walter Block. "Enlarged Perivascular Spaces: How Prevalence Might Influence Gene Therapy Trial Design". In: *the 21st Annual Meeting of the International Society for Magnetic Resonance in Medicine*. Poster #1840. 2013

### 2.1 Abstract

**Purpose:** To develop an imaging protocol suitable for depicting small lenticulostriate arteries (LSAs) and other vessels of the basal ganglia. To assess the prevalence of enlarged perivascular spaces (EPVSs) within the basal ganglia, in a cohort with

clinically relevant age (i.e., similar to the typical age of Parkinson's disease onset). And finally, to determine whether unblinding the surgeon to these bSSFP images of the LSAs results in adjustments to their deep brain stimulation (DBS) surgical plans that were created by viewing only images similar to those used in their standard clinical protocol for DBS planning.

**Methods:** We compared a novel application of balanced steady-state free precession (bSSFP) imaging against the standard time of flight (TOF) technique. Multiple TOF volumes were acquired, with sequence parameters set either to match the bSSFP sequence in imaging time (at lower spatial resolution) or to match the spatial resolution (with longer imaging time). To assess EPVS prevalence, we read MR images from an existing database of 155 cognitively normal research subjects and controls. Subjects were graded atypical if they had  $\geq 1$  large EPVS, or  $\geq 2$  medium EPVS inside (or immediately adjacent to) either putamen. Healthy subjects from the UW–Madison MRI group were scanned with a protocol mimicking the preoperative MRI protocol used for DBS planning at the UW hospital, with the addition of a bSSFP sequence to depict LSAs. An experienced functional neurosurgeon planned DBS surgeries while blinded to the bSSFP imagery, then was unblinded and permitted to alter the planned trajectories if there were concerns about the newly revealed vasculature.

**Results:** For depicting LSAs, bSSFP was superior to TOF imaging of the same scan time or resolution. The prevalence of atypical EPVS in or near the putamen was 19/155 or 12% (within putamen, 15 subjects; immediately adjacent, a further



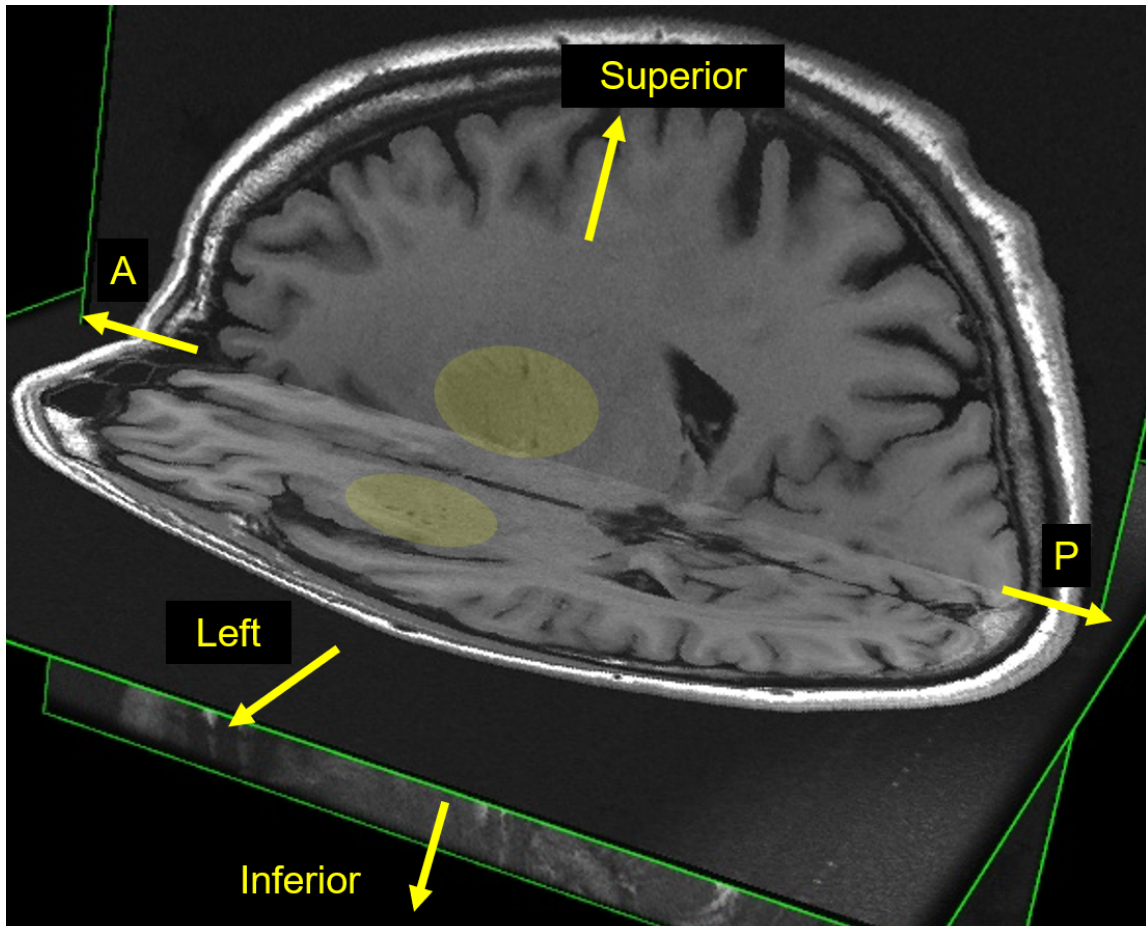
4 subjects) When planning trajectories into the internal globus pallidus (GPi), a common target for Parkinson's DBS therapy, unblinding the surgeon to the bSSFP imagery resulted in a change for 4/22 or 18% of trajectories.

**Conclusion:** Perforating vessels of the basal ganglia are better depicted by bSSFP imaging than TOF, have an enlarged appearance at the region of interest in 12% of PREDICT database subjects examined, and influence the choice of trajectories when planning DBS lead insertions into the GPi.

## 2.2 Imaging basal ganglia vasculature with bSSFP

### INTRODUCTION:

Convection-enhanced delivery (CED) [5] can drive therapeutic agents (infusates) through catheters and may one day slow or reverse neurodegenerative diseases like Parkinson's disease (PD). Research efforts have concentrated on quantifying the localized concentration of infusate delivered under the high pressure used during CED [6]. The high pressure delivery often increases the open, perivascular space running along the exterior of small, distal arteries in the target zone (yellow highlights in Fig. 2.1), creating unwanted escape routes for the infusate. Depicting this vasculature, and later correlating infusate concentration near it during CED, is thus of interest.

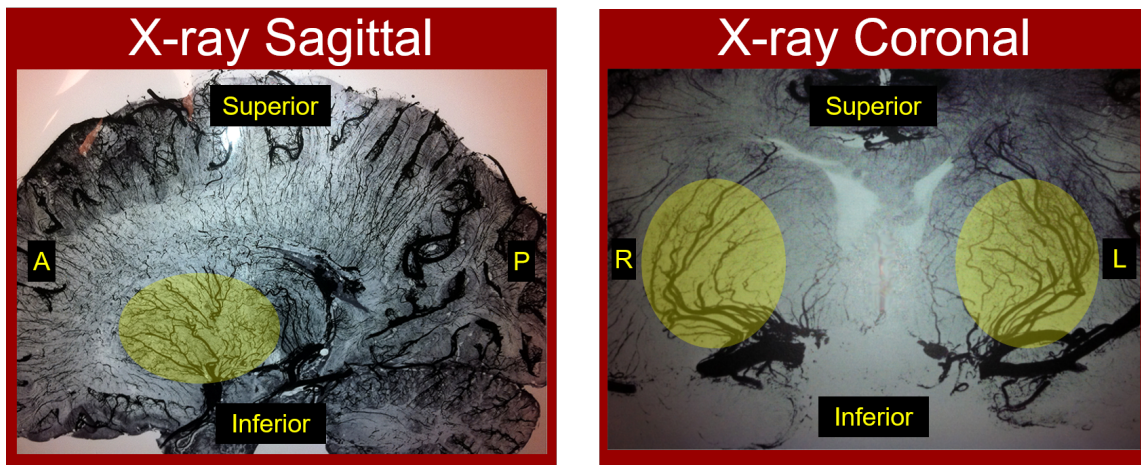


**Figure 2.1: Target region within basal ganglia**

The putamen locations within the basal ganglia are highlighted (yellow) in biplane rendering of two T1-weighted roadmaps (axial and sagittal) in Vurtigo.

We present a visualization platform to simplify the simultaneous viewing of T1-weighted brain roadmaps with vascular 3D data from the desired target zone. Current clinical imaging efforts seldom focus on these small ( $< 500$   $\mu\text{m}$  diameter) perforating arteries (see Fig. 2.2), so we investigate two protocols to image them: balanced SSFP (bSSFP) and Time Of Flight (TOF). Standard 3D TOF has poor

sensitivity for vessels of the putamen, which are of submillimeter caliber and small flow rate. We introduce a new use for bSSFP: visualizing this vascular territory, a task previously not necessary in diagnostic neuroradiology. The end goal of the platform is to help the interventionalist choose a catheter trajectory that is as distant as possible from local vasculature to minimize loss of infusate.



**Figure 2.2: X-ray atlas of lenticulostriate arteries**

A cadaver atlas [7] establishes the small caliber of the vessels we wish to image. High resolution contrast-enhanced, thin section X-ray images show the perforating appearance in the putamen (highlighted yellow).

## **METHODS:**

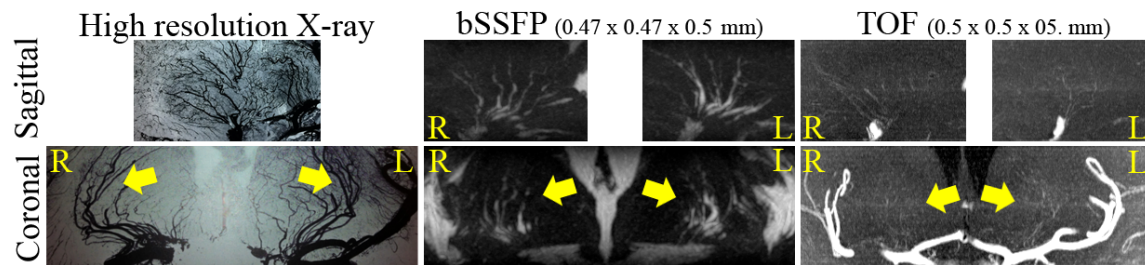
Using a 3T GE scanner and 32-channel head coil, a high-resolution 3D T1-weighted image volume is first acquired with gray/white matter contrast sufficient to identify the desired treatment region. We focus on a gray matter region, the putamen. The roadmap is loaded in Vurtigo, an open-source visualization platform, developed at the University of Toronto and the affiliated Sunnybrook Research Institute [8]. We

modified Vurtigo to allow us to render vascular data from constrained regions near the target simultaneously with the T1 roadmap. The Vurtigo-based visualization is compatible with a Vurtigo plug-in used to direct real-time targeting and monitoring in CED treatments [9].

Time of Flight (TOF) is a diagnostic standard for imaging the relatively large, high velocity feeding vessels crucial for perfusion of the brain. Imaging the much smaller, slower flow in the perforating vessels in the putamen led us to explore a comparison of three TOF protocols of varying resolution with a balanced steady-state free precession (bSSFP) acquisition in 10 healthy volunteers. Scan parameters were chosen to create TOF scans of similar and longer duration to the bSSFP scans, with the longest scan having similar resolution to the bSSFP scan. We acquired a bSSFP volume with  $0.47 \times 0.47 \times 0.5$  mm (64 slices total) with a 40 degree flip angle and 3 signal averages in a scan time of 6:16. The three TOF protocols utilized a 15 degree flip angle to image 2 slabs (50 slices total) to cover the putamen with voxel dimensions of a)  $0.86 \times 0.86 \times 0.8$ mm (5:18), b)  $0.57 \times 0.57 \times 0.6$  mm (6:45), and c)  $0.5 \times 0.5 \times 0.5$  mm (8:11). The inferior face of the imaging slabs was prescribed to maximize fresh inflow into the putamens in each case.

## **RESULTS:**

As a reference of the putamen vasculature, high resolution (200  $\mu$ m) atlas X-ray images of thin, fixed slices after iodinated contrast was injected in a cadaver are shown in the sagittal (top) and coronal planes (bottom) of Fig. 2.3.



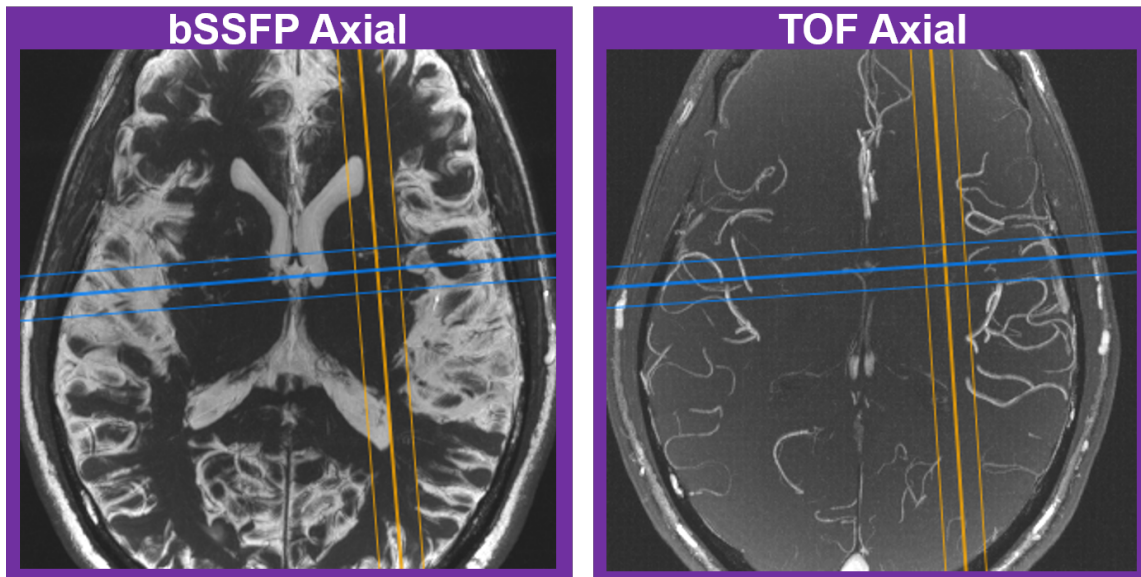
**Figure 2.3: X-ray, bSSFP, and TOF of LSAs**

Comparison of cadaver X-ray reference (left), bSSFP (center) and TOF (right) of the putamen in the sagittal (top) and coronal plane (bottom). bSSFP better depicts the vascular appearance (shrub-like in sagittal, at heads of yellow arrows in coronal).

The shrub-like appearance of the putamen's perforating vessels in the sagittal is clearly more visible with bSSFP than in the best depiction of the TOF data (the 8:11, highest resolution scan). The coronal frame bSSFP depiction also has much higher contrast than TOF, but the bright cerebrospinal fluid in bSSFP images complicates the rendering – hence the need for a restricted MIP volume.

Images in figures 2.4–2.6 show that large scale vasculature throughout the whole brain is well depicted with TOF, but bSSFP is needed in order to see more of the submillimeter vessels in the putamen.

The bSSFP depiction of the putamen vasculature, shown in figures 2.5 and 2.6 corresponds well to the perforating appearance in the hi-res X-ray atlas shown in figure 3.



**Figure 2.4: Axial comparison of bSSFP and TOF**

The thinnest yellow and blue lines indicate the extent of the MIPs shown in the following two views.

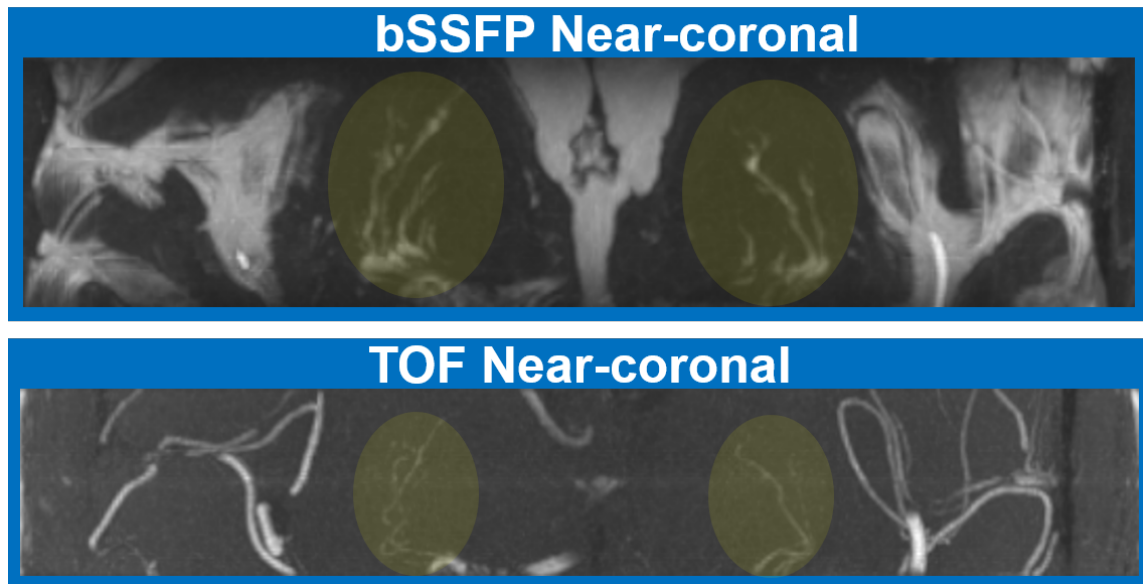


Figure 2.5: Near-coronal comparison of bSSFP and TOF  
Putamen highlighted in yellow.

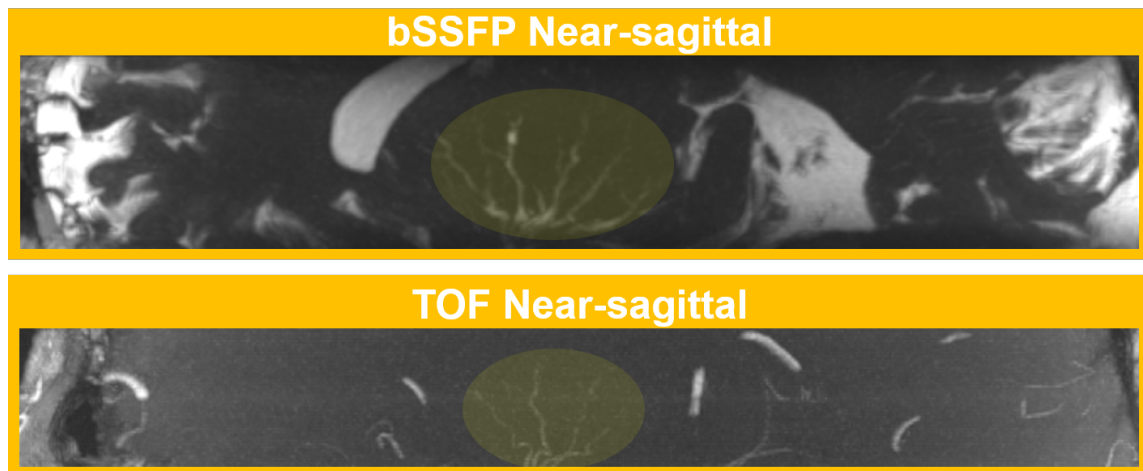
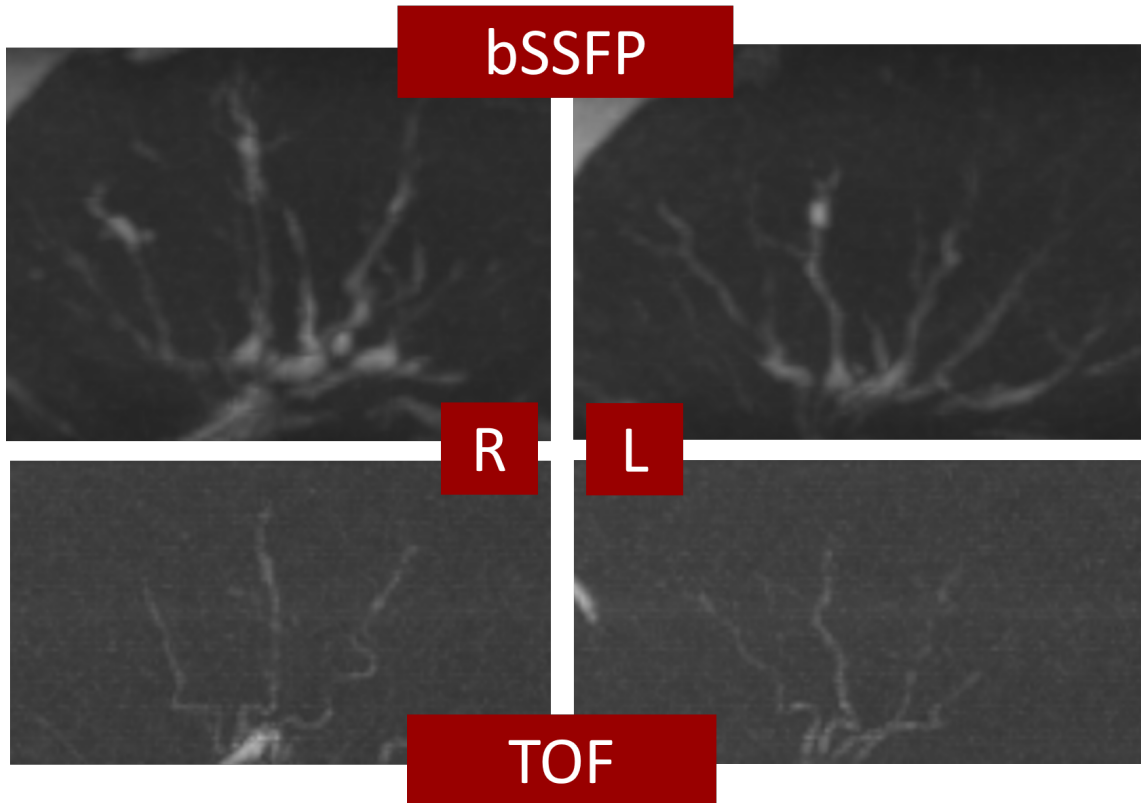


Figure 2.6: Near-sagittal comparison of bSSFP and TOF  
Putamen highlighted in yellow.

Side by side comparisons of one subject and four more subjects are shown in Figures 2.7 and 2.8, respectively.



**Figure 2.7: bSSFP vs. TOF in one subject**  
Near-sagittal views of both the right and left putamen, greatly magnified to facilitate comparison between bSSFP and TOF.



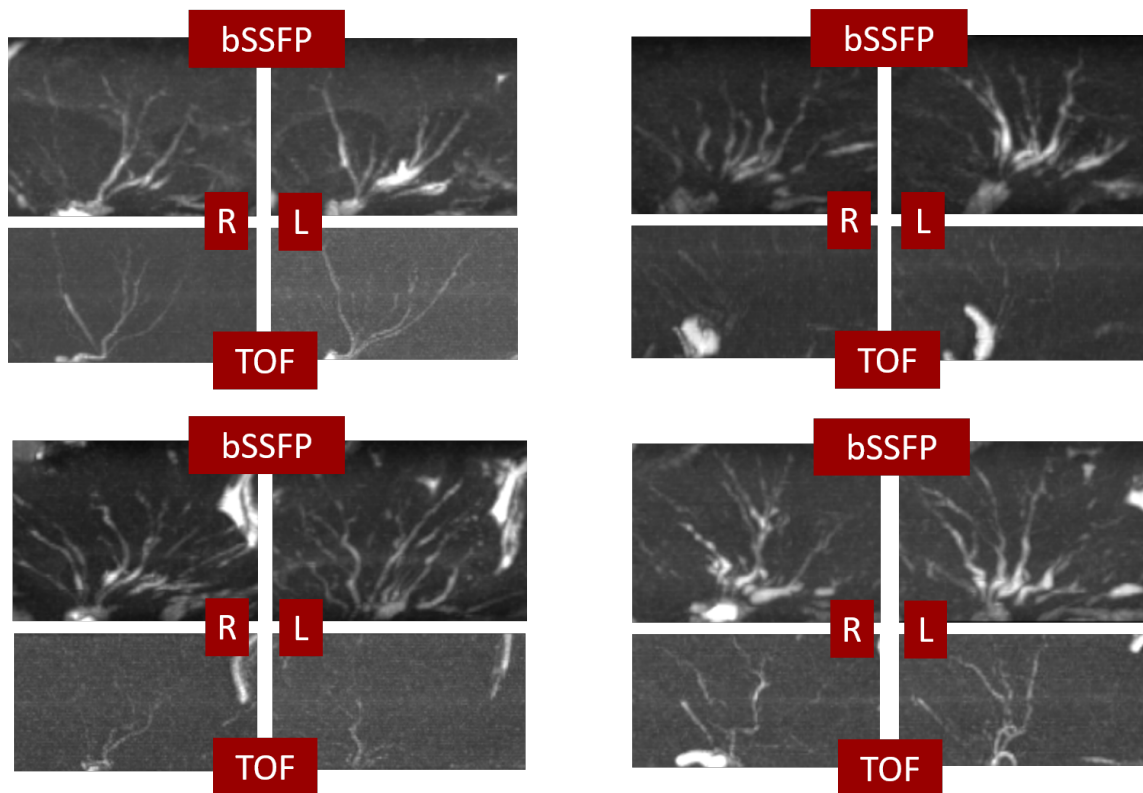


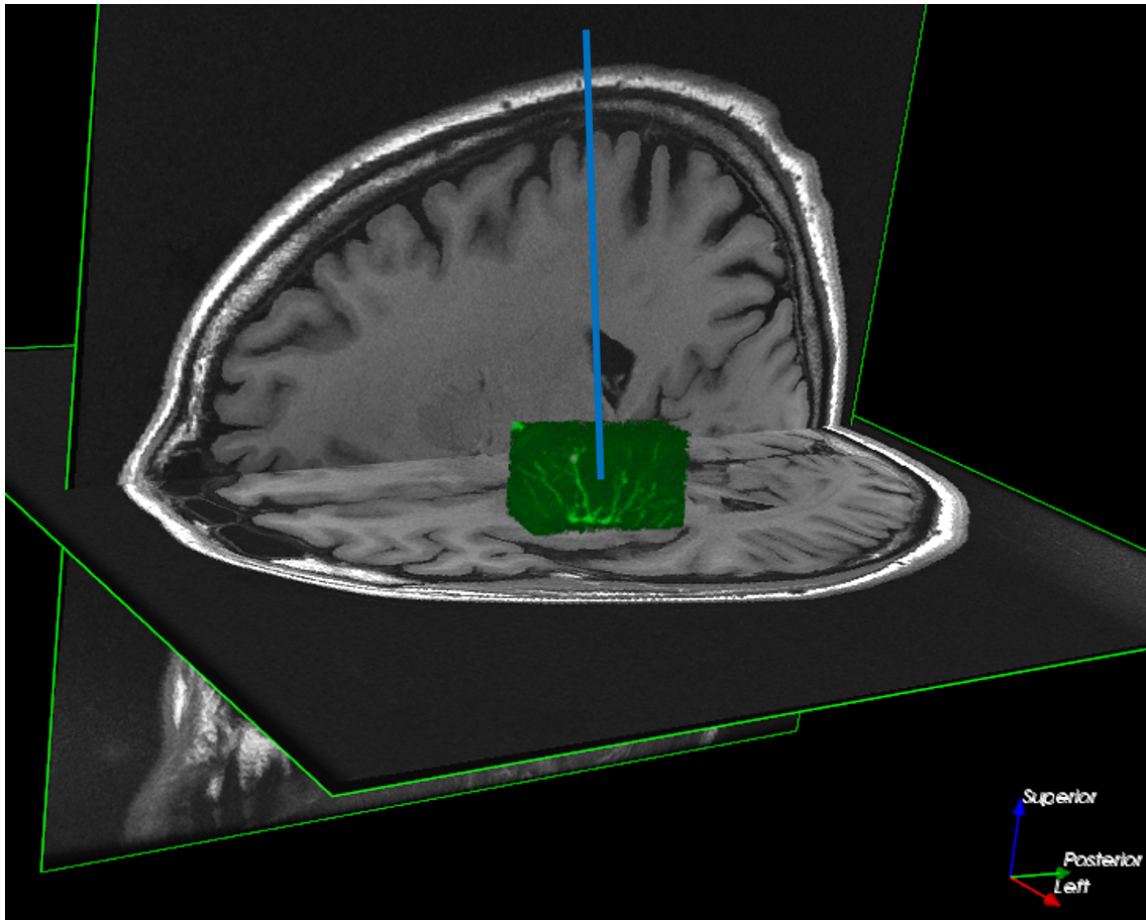
Figure 2.8: **bSSFP vs. TOF in four subjects**  
Near sagittal comparisons of bSSFP vs. TOF in four other volunteers.

This comparison demonstrates that bSSFP depicts the putamen vasculature with greater conspicuity than 3D TOF and in less scan time.

For imaging large cerebral feeding vessels, bSSFP should not be expected to perform better than TOF. Susceptibility artifacts at air-tissue interfaces, and confounding signal from CSF limit the useful domain of bSSFP. However, in regions that are sufficiently distant from sinuses or CSF, bSSFP shows vascular anatomy with greater sensitivity than a traditional TOF sequence.

## CONCLUSION:

A visualization platform has been developed for simultaneously visualizing brain structures and small vessels in the target area for CED.



**Figure 2.9: Example CED plan**

Restricted-volume MIP of vasculature (green) overlaid upon biplane rendering of two T1-weighted roadmaps in Vurtigo. A possible catheter trajectory, which avoids the largest vessels, is shown in blue.

We aim to compare bSSFP and TOF sequences on a cohort of Parkinson's pa-

tients. The visualization platform will next be utilized to drive real-time planning, targeting, and monitoring in an animal model in conjunction with the RTHawk real-time imaging platform.

### **ACKNOWLEDGEMENTS:**

We thank Sam Hurley, Kevin Johnson, Howard Rowley and Charles Strother of UW-Madison for their helpful input. This research is primarily supported by the Kinetics Foundation. We also acknowledge the UW's institutional support from GE Healthcare. Finally, many thanks to our volunteers from the MR group at UW-Madison.

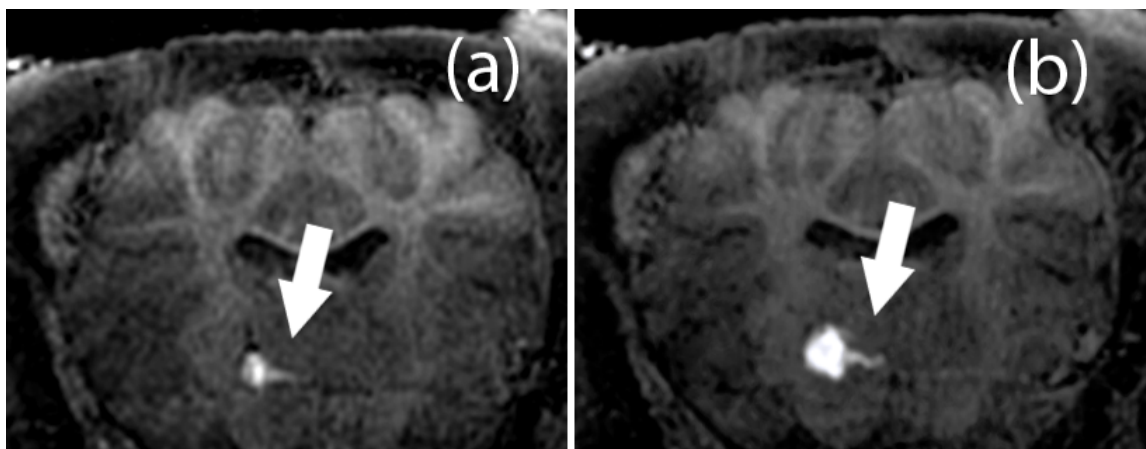
## **2.3 Prevalence of enlarged perivascular spaces**

### **TARGET AUDIENCE:**

This information will benefit scientists and clinicians working in the field of convection enhanced delivery (CED) of therapeutic drugs to the brain. It will be of particular interest to those who are focusing on gene therapy within structures of the basal ganglia, especially those targeting the putamen for Parkinson's disease (PD).

## INTRODUCTION:

Perivascular spaces (PVS) are cavities that surround blood vessels in the brain and contain cerebrospinal fluid. PVS have been shown to act as channels that affect the spatial distribution of infusate injected via convection enhanced delivery (CED) in rat [10] and non-human primate [11] animal models. Our group has also observed this effect in CED experiments with swine models, shown in Figure 2.10.



**Figure 2.10: Infusate diversion during CED**

Coronal time series of in-vivo CED experiment shows infusate doped with Gd-DTPA following unwanted medial leakage pathway (arrows) towards the midline near the start of infusion (a), and at the end, 7 minutes later (b).

Atypical enlarged PVS (EPVS) are present in an unknown percentage of human putamen, the gray matter structure commonly considered in gene therapy trials for Parkinson's disease, and may cause variability in the infusate distribution. This work aims to estimate their prevalence in the putamen in a cohort with age similar to PD patients. Knowledge of the prevalence would influence the effort expended to

detect and track their unwanted effects in dosage distribution in possible upcoming clinical trials.

Previous studies have investigated EPVS in pediatric to young adult [12] and elderly [13] populations. Though many studies of EPVS consider various substructures of the brain in their rating, it is rare to find one among them that has examined both our study's age cohort and the putamen specifically. Furthermore, most rating schemes in the literature are based on counting the number of EPVS in a particular slice, with reduced emphasis on the size of EPVS observed, which may affect the degree of infusate loss.

## **METHODS:**

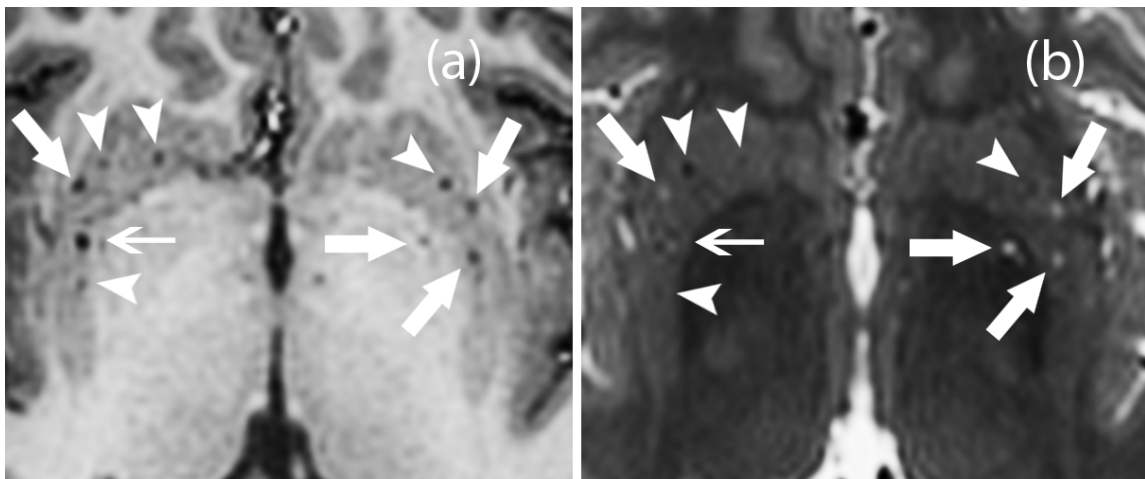
We utilized an existing database of cognitively normal, healthy adults enrolled in a longitudinal study on Alzheimer's disease, the Wisconsin Registry for Alzheimer's Prevention (WRAP). We examined data from the 155 subjects who had T1w, FLAIR, and T2w scans all performed in the same visit. Demographic data is shown in Table 2.1.

Subjects selected	155 (46 male)
Age at scan [years]	
Mean $\pm$ SD	59.8 $\pm$ 6.0
Range	46–71

**Table 2.1: Demographic data of subjects analyzed.**

Their mean age,  $59.8 \pm 6.0$  years, is similar to the mean age of onset in Parkinson's

disease. EPVS  $< 2$  mm are deemed small in a seminal review paper on EPVS [14]. We classified subjects as atypical if they had two or more medium (2-5 mm diameter), or one or more large ( $>5$  mm) EPVS in the putamen. Differentiation of EPVS from blood vessels is illustrated in Fig. 2.11, with EPVS appearing hyperintense in T2-W images (Fig. Fig. 2.11b) and both structures appearing hypointense in T1-W imaging (Fig. Fig. 2.11a).



**Figure 2.11: Example EPVS in human brain**

Axial T1-W (a) and T2-W (b) images of an example human brain showing EPVS, hypointense in T1 and hyperintense in T2 (arrows), and normal vessels, hypointense in both (arrowheads). The thin arrow indicates a structure in the right putamen that is possibly a confluence of multiple vessels. (Image contrast set very high for conspicuity).

The sequences examined in this study were 3D acquisitions with whole brain coverage and 256x256 voxels in plane (Table 2.2).

Seq. name	Voxel size [mm <sup>3</sup> ]	FOV [mm <sup>3</sup> ]	T <sub>E</sub> /T <sub>R</sub> /T <sub>I</sub> [ms]	NEX
3D Axial FSPGR T <sub>1</sub> w	1×1×1	256×256×160	3.18 / 8.16 / 450	1
3D Sagittal CUBE T <sub>2</sub> w	1×1×1	256×256×160	72.2 / 2500 / 0	1
3D Sagittal CUBE FLAIR	1×1×2	256×256×160	122.8 / 6000 / 1869	1

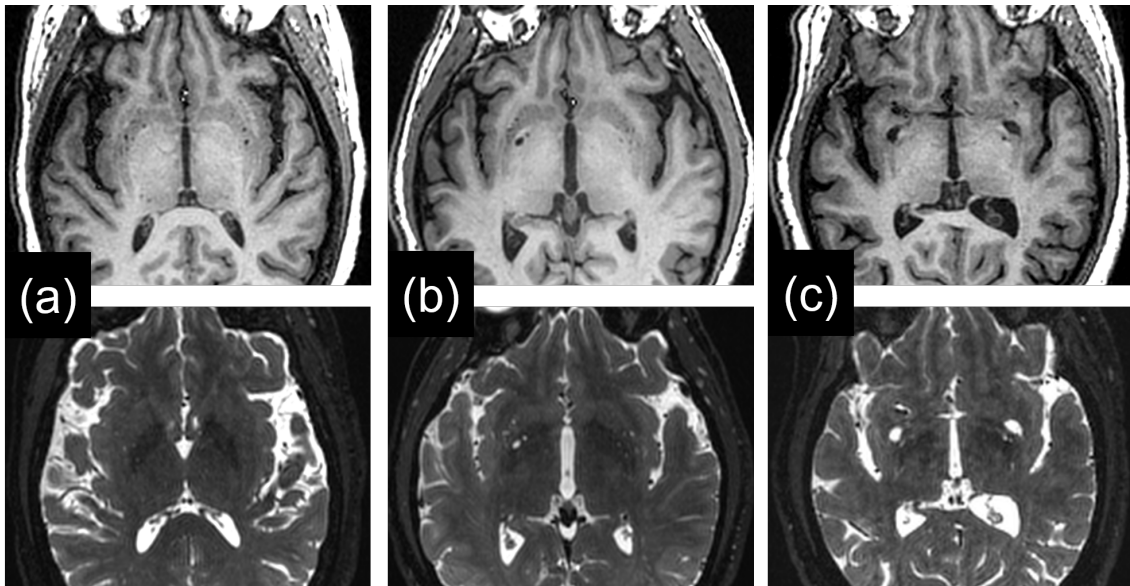
**Table 2.2: Parameters of MRI sequences analyzed for presence of EPVS.**

Sequence parameters of isotropic or near isotropic whole brain volumetric imaging used for detection of EPVS.

MRI datasets were viewed in the axial plane (with reformatting for T2 and FLAIR) and features suspected to be enlarged PVS were identified and confirmed by simultaneous viewing of T1 and T2 data for a given slice. In one instance, FLAIR images were used to rule out a feature that was not an EPVS but likely an old lacunar infarction [14].

## RESULTS:

Fifteen of 155 subjects were classified as having atypical EPVS in the putamen. Four had atypical vasculature near, but just outside the putamen, and 136 were deemed normal. Examples are shown in Figure 2.12.



**Figure 2.12: Comparison of normal subject and atypical subjects** (T1-w images on top row and T2-w images on the bottom row). A subject with a few small EPVS, rated normal (a). A subject with an EPVS just over 5 mm in diameter, rated atypical (b). And a subject with two large EPVS (7~8 mm), rated atypical (c).

## DISCUSSION:

Given that all subjects participating in a CED-based gene therapy drug trial would receive preoperative brain MRI, those Phase I subjects who have atypical EPVS would merit MR-based quantification of infusate distribution during the procedure. Depending on the degree of infusate loss, the presence of EPVS may be useful as an exclusion criterion during later phases of the clinical trials. A semi-quantitative rating scheme [13] assigns a grade based solely on a count of EPVS. Since the size of EPVS may be relevant to their role as channels for infusate loss, existing rating schemes may be inadequate for predicting likelihood of unwanted infusate loss.



## **CONCLUSIONS:**

We have shown the prevalence of atypical perivascular spaces in the putamen in a moderate-sized cohort of healthy subjects with average age similar to the average age of Parkinson's disease onset. Detecting EPVS in subjects prior to treatment and then monitoring infusion distribution in those subjects seems worthwhile, given a prevalence of 12% and the modest effort needed.

The size of EPVS may be relevant to their role as channels for infusate loss, thus, existing rating schemes which are based on a count instead of on a measured size may be inadequate for predicting likelihood of infusate loss. A measurement-based rating scheme may not be ideal, however, because of ambiguities that can arise from, for instance, the window and level settings when images are viewed.

The database used in this work also contains coregistered versions of the images, which could be used as inputs for a quantitative approach that eschews counts and human-made measurements for a computer vision alternative. A variety of computational methods appropriate for EPVS quantification have recently been cataloged [15]. Use of such a method could better standardize, and likely hasten, future analysis of EPVS.

## **ACKNOWLEDGEMENTS:**

We thank Howard Rowley, Amy Hawley, and Sam Hurley of UW-Madison for their helpful input. This research is primarily supported by the Kinetics Foundation. We also acknowledge the UW's institutional support from GE Healthcare.

## 2.4 Effect of bSSFP angiography on DBS plans

### Methods

Initially we sought to match the clinical DBS patient MRI protocol as closely as possible, but after preliminary testing with a couple of pilot volunteers, we moved from the standard 1.5 T scanner to a 3 T system.

We recruited 11 healthy subjects from within the MRI group at UW–Madison (7 male). Age at time of scan was  $32.6 \pm 6.3$  years (mean  $\pm$  SD). Scans were performed on a 3 T Discovery MR750 scanner (GE Healthcare, Waukesha, WI), using a 32-channel Nova head coil. The imaging protocol sequences are described in Table 2.3:

Seq. name	Time [m:ss]	FOV [mm <sup>3</sup> ]	Matrix	FA [deg.]	TE/TR/TI [ms]
T <sub>1</sub> BRAVO	2:14	256x256x146	256x256x200	12	3.2 / 8.2 / 450
CUBE T <sub>2</sub>	2:25	256x256x146	256x256x150	90	104 / 3000 / 0
CUBE T <sub>2</sub> FLAIR	4:57	256x256x146	256x256x200	90	130 / 7000 / 2033
SWAN	6:38	240x240x78	448x448x78	10	25 / 39 / 0
bSSFP	6:16	240x240x32	448x448x64	40	1.9 / 5.4 / 0
TOF	8:18	240x240x95	256x256x120	15	2.7 / 22 / 0

Table 2.3: **DBS planning MRI sequences.**

T1- and T2-weighted sequences had whole head coverage. Axial bSSFP and SWAN covered putamen. Axial TOF covered partial head, from inferior end of putamen to scalp. The TOF matrix dimension labeled “120” is made up of 4 slabs with 30 locations each.

The multi-slab TOF sequence with large coverage along the S–I axis is configured to mimic the coverage and information about cortical vessels to avoid. For clinical DBS patients, this information is obtained with a contrast-enhanced T1w scan that

cannot be performed on volunteers.

The procedure for preoperative planning is defined in a standard operating protocol document, a physical copy of which was referenced by the surgeon during each planning session. The procedure is as follows:

### **DBS planning SOP**

1. Create a folder with subject ID in the name for holding screenshots and PAK file output.
2. Start the trajectory planning software, *WayPoint Navigator*.
3. Load the T1 roadmap volume (likely series #4 with a name like “Sag FSPGR T1 BRAVO”).
4. Load whole-brain angiography volume (likely series #8, with a name like “TOF 1mm whole brain”)
5. Coregister TOF onto T1 volume. Run the “register by intensity” registration at least 3 times, until the changes become too slight to notice.
  - T1 and TOF image data will be used simultaneously to select the initial trajectories. Together, they approximately capture the information in the T1+Contrast sequence that is used on clinical DBS patients.
6. Manually identify Anterior Commissure (AC), Posterior Commissure (PC), and mid-sagittal plane.
7. Select target point in right side Globus Pallidus internal (GPi)

8. Select entry point for initial trajectory into GPi.
  - Remember to uncheck “Move Target and Entry in Parallel” checkbox.
  - Generally, entry will be near the coronal suture. Choice of entry point will be based on anatomical data, e.g. trying to come in at the crest of a gyrus while avoiding: surface vessels, sulci, and passing through ventricles.
9. Mirror the existing trajectory over the midline to get an initial guess for the contralateral trajectory.
10. Adjust target point onto desired location within GPi. (The target point probably won't need much adjustment after mirroring.)
11. Adjust entry point.
12. Take four screenshots to record: AC, PC, right, and left trajectories.
  - Make sure that “Reference” in upper right corner is set to “CT coordinates”.
  - In the planning interface, under “5. Add Trajectories...” select the “Trajectories” tab (which is on the bottom of the scrollable area, just above the button “6. Select Platform Model...” ) and scroll as needed to ensure that both the entry and target point coordinates are in view.
13. Load bSSFP volume (likely series #6 with a name like “Ax bSSFP 448”).
14. Coregister bSSFP volume onto roadmap volume. Run the registration at least 3 times, until the changes become too slight to notice.
15. With bSSFP volume visible, refine trajectories if desired.

16. If avoiding a specific vessel of concern, take a screenshot with the 3D cursor on the vessel to record its location.
17. Record new coordinates of final refined trajectories by taking screenshots.
18. Save PAK file which contains trajectory plans.
19. Close the trajectory planning software.

Example folder and filenames:

2017-01-25 plan - subject LV

Lab Volunteer LV pack.pak

Setup - AC.jpg

Setup - PC.jpg

Trajectory - before bSSFP - left.jpg

Trajectory - before bSSFP - right.jpg

Trajectory - following bSSFP - left.jpg

Trajectory - following bSSFP - right.jpg

Vessel avoided - left - moved entry posterior medial.jpg

Vessel avoided - right - moved entry posterior lateral.jpg

## Results

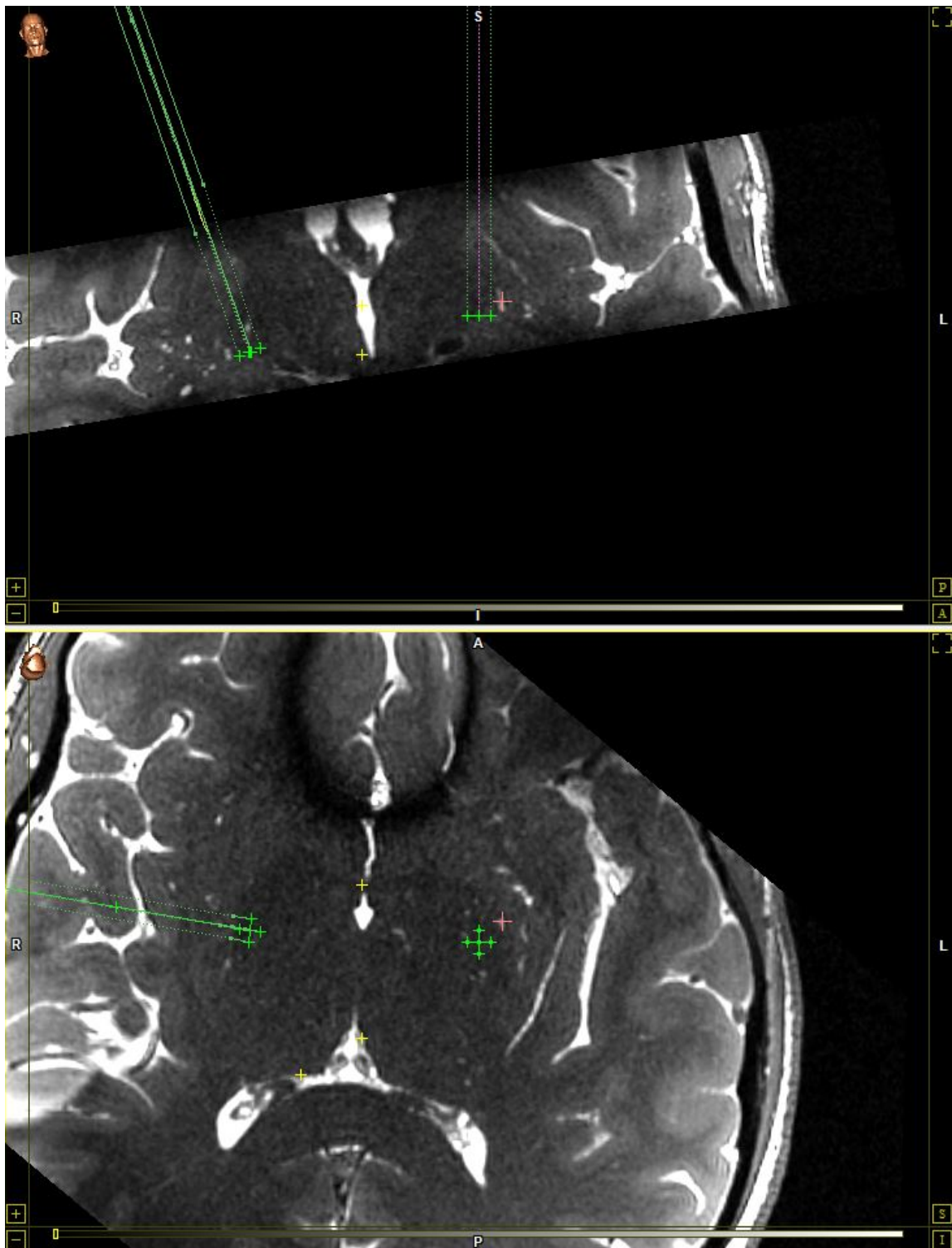
A total of 4/22 trajectories (18%) across 3/11 subjects were altered after unblinding the DBS planning surgeon to the bSSFP imagery, shown in Table 2.4.

Subject	$\Delta\text{Ent.}_L$ [mm]	$\Delta\text{Tgt.}_L$ [mm]	$\Delta\text{Ent.}_R$ [mm]	$\Delta\text{Tgt.}_R$ [mm]
1	9.9	0	17.3	0
2	0	0	0	0
3	4.6	0	0	0
4	0	0	0	0
5	0	0	0	0
6	0	0	3.5	2.0
7	0	0	0	0
8	0	0	0	0
9	0	0	0	0
10	0	0	0	0
11	0	0	0	0

**Table 2.4: Changes to DBS planning trajectories.**

Total 3D displacement of entry and target points for the left and right hemispheres after unblinding to bSSFP imagery.

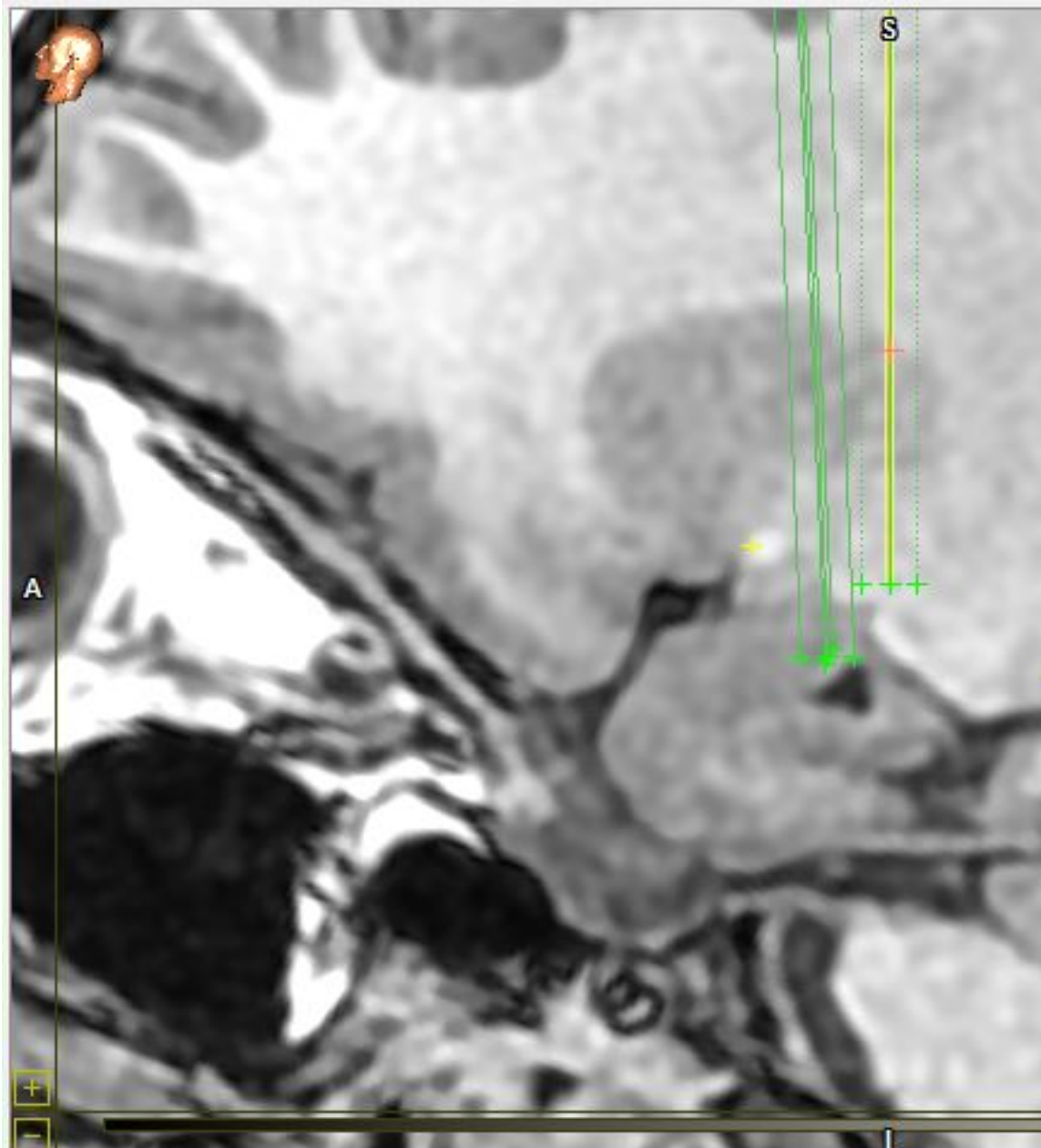
Among the four altered trajectories, entry points changed in all four cases and in one of those cases, the target point was also changed. Figure 2.13 shows an example after moving the entry point posterior and medial to avoid a vessel:



**Figure 2.13: Coronal and axial views after adjusting left trajectory**  
 Coronal (top) and axial (bottom) views of bSSFP imagery with planned trajectories overlaid in green and avoided vessel marked with a red crosshair. For each hemisphere, the solid green line is the central insertion path and the four dotted lines which are displaced from it in the cardinal directions are alternate paths allowed by the trajectory guide.

In another case (Fig. 2.14) the entry point was moved posterior to avoid a vessel and a note was made to discourage using the alternate track which is anterior to the main trajectory, as this track is nearly intersecting the vessel that was avoided.





**Figure 2.14: Sagittal view after moving entry point posterior**

Sagittal view of T1w scan shows the vessel avoided (hyperintensity under small yellow crosshair) and the planned trajectories posterior to the vessel. Of the alternate trajectories, the anterior one is especially close to the vessel and should not be used for DBS lead introduction.

## Conclusions

We have demonstrated that bSSFP depicts more of the vasculature in the basal ganglia, with higher conspicuity, and in less imaging time than arterial TOF. There are drawbacks to bSSFP such as banding artifacts and unwanted signal from ventricles, but these can be overcome by offsetting the RF phase to shift the location of the artifact, and by using visualization software such as we have developed, which can restrict the MIP rendered volume to limit it to just the region of interest around the LSAs.

We have also demonstrated that EPVS are present in or near the basal ganglia of approximately 12% of adults around the typical age of Parkinson's disease onset. Given this non-negligible fraction and the ease of EPVS detection, we recommend the use of a similar imaging protocol which may be useful to screen patients entering trials for experimental therapies administered by CED.

In all of these trajectories (into GPi from superior parietal bone) the LSA vasculature to be avoided is closer to the target point than the entry point. This means, for a fixed target point, to move the trajectory line 1 mm farther away from a nearby vessel requires that the entry point must be moved by more than 1 mm. For a given amount of point displacement, adjusting the target by that amount will cause the trajectory to move farther within the basal ganglia than the same amount of adjustment at the entry point. Targets, however, are small enough that there is much less freedom to adjust the targeted coordinates before compromising the clinical goal of treating that target. In contrast, the entry point may be varied much more freely if the trajectory requires adjustment. Thus, in practice, moving the entry point is the

more likely resolution when adjusting a trajectory to avoid hazards on the way in.

During the early stages of refining the MRI and DBS planning protocols, a SWAN sequence was included and the result incorporated into the planning workflow. The rationale was that SWAN might provide even more useful images than bSSFP: possessing high resolution, good volume coverage, and the ability to distinguish between arteries and veins. The images are detailed, but were described by the surgeon as “scary”. Taking the X-ray atlas images (Fig. 2.3) to be representative of the anatomical ground truth, one might reasonably conclude that reality is scary.

With any new procedure, user experience is an important consideration. It is undesirable to bombard the user—in this case, the surgeon planning a DBS procedure—with so much information that it leads to hesitancy or choice paralysis. A balance must be struck, and only showing the LSAs of intermediate size (smaller than TOF can depict, but larger than the smallest that SWAN can depict) and up may be the best option for this task.

### 3 COMPUTATIONAL DEVICE TRACKING

---

In the last chapter I described how the vasculature can present challenges during the sorts of surgeries we do, and how preoperative planning may allow us select trajectories that avoid the vasculature. In this chapter, I describe intraoperative MRI methods for tracking a trajectory guide as it is aimed inside a standard diagnostic MRI scanner, so that we can achieve the desired trajectories when inserting interventional devices.

Portions of this chapter have previously been presented at the 2016 ISMRM data sampling workshop and at the main meetings in 2016 and 2017, submitted as a patent in 2015, and are in preparation for a manuscript submission to *Magnetic Resonance in Medicine*.

- **Miles E. Olsen**, Ethan K. Brodsky, Jonathan A. Oler, Marissa K. Riedel, Sascha A. L. Mueller, Scott C. Vermilyea, Jeanette M. Metzger, Yunlong Tao, Kevin G. Brunner, Azam S. Ahmed, Su-Chun Zhang, Marina E. Emborg, Ned H. Kalin, and Walter F. Block. “Real-time trajectory guide tracking for intraoperative MRI- guided neurosurgery”. In: *prep. for submission to Magnetic Resonance in Medicine* (2022)
- **Miles Olsen**, Scott Vermilyea, Jianfeng Lu, Ethan Brodsky, Scott Guthrie, Yunlong Tao, Eva Fekete, Marissa Riedel, Kevin Brunner, Carissa Boettcher, Viktorya Bondarenko, Andrew Alexander, Su-Chun Zhang, Marina Emborg, and Walter Block. “Targeted Delivery of Stem Cells to the Brain using Real Time Interventional MRI”. in: *the 26th Annual Meeting of the International Society for Magnetic Resonance in Medicine*. Talk #0738. 2017
- **Miles Olsen**, Ethan Brodsky, Jonathan Oler, Marissa Riedel, Eva Fekete, Ned Kalin, and Walter Block. “Rapid Device Localization for Prospective Stereotaxy: Using Computation Instead of Imaging”. In: *the ISMRM Workshop on Data Sampling & Image Reconstruction*. Talk Session 2: Quick Talks on Fast Scans, 12:35 pm. 2016

- **Miles Olsen**, Ethan Brodsky, Jonathan Oler, Marissa Riedel, Eva Fekete, Ned Kalin, and Walter Block. "Rapid Device Localization for Prospective Stereotaxy: Using Computation Instead of Imaging". In: *the 24th Annual Meeting of the International Society for Magnetic Resonance in Medicine*. Talk #0197. 2016
- **Miles Olsen**, Ethan Brodsky, and Walter Block. *System and Method For Real-Time Interventional Device Localization Using Magnetic Resonance Imaging*. US 2016 0349335 A1, submitted to US Patent Office. May 2015

### 3.1 Abstract

**Purpose:** To develop a real-time interactive method for aiming MR-compatible trajectory guides used to insert interventional devices during neurosurgery. In current neurosurgery methods, an iterative approach is used to aim trajectory guides at intracerebral targets: image MR-visible markers, determine current trajectory by fitting model to image, manipulate device, repeat. Here, an interactive method is presented that exploits the simple cylindrical geometry of a trajectory guide's MR-visible alignment stem.

**Methods:** The current trajectory of the alignment stem was computed by determining two points along its central axis, rather than by imaging the entire stem. Points were determined by correlating 1D spokes from a radial sequence with the known cross-sectional projection of the stem. A real-time platform was utilized to control MR sequences and data acquisition. On-screen updates were viewed by the operator while simultaneously manipulating the trajectory guide to align it with the planned trajectory. Accuracy was quantitatively validated in a phantom, and in-vivo validation was demonstrated in nonhuman primates undergoing preclinical

gene (n=5) and cell (n=4) delivery surgeries to bilateral dorsal amygdala and unilateral substantia nigra, respectively.

**Results:** Interactive real-time aiming feedback was provided at five updates/second, achieving  $<0.68$  mm radial error at an average depth of 48 mm in 10 phantom experiments corroborated with high-resolution 3D MRI. Successful in-vivo delivery of payloads to all 14 targets was demonstrated across the 9 surgeries.

**Conclusion:** Real-time trajectory tracking permitted interactive device manipulation and resulted in sub-millimeter radial error. Intraoperative monitoring of brain shift and therapeutic delivery are additional benefits of in-bore MR procedures.

## 3.2 Introduction

When compared to stereotactic surgery using only preoperative images for the placement of interventional devices, intraoperative MRI (IMRI) device navigation provides for increased control and accuracy. Typically, preoperative MRI, the gold standard for planning neurosurgical procedures, is used in the conventional operating room (OR) setting by coregistering the coordinate system of the OR with a previously acquired MRI volume of the brain. A surgical workstation with an optical tracking camera, shown in Figure 3.1a, tracks multiple fiducial markers to overlay the orientation and position of the device onto the MR volume. While OR-based approaches without intraoperative tomographic imaging are unable to visualize brain shift, optical tracking methods are appealing as they provide near immediate updates of device position at video-like frame rates as the operator

manipulates the device's orientation.

IMRI procedures permit visualization of therapeutic delivery and can account for the anatomical brain shift that occurs when the skull is opened. MR guidance is now used clinically to guide biopsy needles and stimulation electrodes [16–19] to targets deep in the brain during surgeries performed completely under general anesthesia. This MR image-guided strategy enables clinicians to monitor a therapy as it occurs, rather than retrospectively, which allows for the possibility of detecting and correcting problems during the intervention and confirming success.

In clinical settings, such MR image-guided brain therapies have included ablation procedures [20, 21] and the delivery of chemotherapeutic agents [22]. In the research setting, MR image-guided surgery has been applied in chemotherapeutic agent delivery [23–25], as well as efforts to treat Parkinson's disease by delivery of viral vector gene therapy in humans [26, 27] and non-human primates (NHPs) [28–31]. As illustrated in Figure. 3.1b, the guiding of devices is normally performed using standard MRI sequences to image MR-visible fiducial markers (“fiducials”) on the device, such as a cylindrical annulus of water in a trajectory guide used to align a biopsy needle or cannula. Clinical alignment methods often iteratively collect a 2D multi-slice or 3D volume depicting the fiducials, fit a model of the device to the image to determine device orientation, and then inform the operator on how to modify the orientation to achieve the planned trajectory. This process continues until the device is oriented within some operator-defined error bound dependent on the application's need for accuracy [17]. Imaging time per iteration can often be sub-minute for the first pass but it grows in time as obtaining

finer precision in the alignment is pursued in subsequent iterations with higher resolution imaging.

A method termed “prospective stereotaxy” (Fig. 3.1b) was pioneered by Truwit and Liu [32]. Subsequent research efforts have streamlined the process of MRI plane prescription, acquisition, and reconstruction to provide updates to the operator using fully sampled Cartesian imaging [9] (Fig. 3.1c). An illustration of the prospective stereotaxy technique is shown in Figure 3.2a. The planned trajectory is formed by two points: the target point within the body and the pivot point at the center of the ball joint. The line from target to pivot is extended to determine an “aim point” at some offset away from the pivot, outside the body. Imaging is performed in a plane containing that aim point and perpendicular to the planned trajectory. Alignment is achieved when the MR-visible stem is collinear with this trajectory (i.e., when the image of the stem’s cross-section is centered on the aim point), at which point the locking ring is tightened to immobilize the ball joint. The stem is then removed and the cannula is introduced into the brain, coaxially to the trajectory guide. An example of such an MR-compatible trajectory guide, the FDA-approved Navigus (Medtronic, Minneapolis, MN), is shown in Figure 3.2. This trajectory guide, used throughout the gene and cell delivery studies described herein, consists of a skull-mounted base containing a fixed (non-translatable) ball joint that allows the trajectory to be oriented  $\pm 18^\circ$  off center.

Imaging and manipulation of the trajectory guide are normally done iteratively in clinical procedures today. An interactive implementation, using real-time imaging of the aiming plane in Figure 3.2a, was introduced by Brodsky et al. [9, 33].



The operator viewed the aiming plane images on a monitor while reaching into the MRI bore to manipulate the trajectory guide. To accurately target small structures, higher spatial resolution imaging is needed. This, in turn, decreases the rate of updates during the aiming of the trajectory guide.

Rather than image the entire device, the identification of the trajectory guide's central axis can be accelerated by only acquiring a subset of 1D MR readouts and exploiting a priori information about the trajectory guide's dimensions. We propose a method that uses a computational (rather than image-based) approach to provide real-time interactive feedback to the operator at a rate of 5 Hz, which is closer to the rate of the optical systems with which stereotactic surgeons are familiar. The proposed method replaces 2D imaging with an overdetermined subset of rapid 1D readouts, and here we provide methodological details for implementation using simple trajectory guides [34]. In addition to in vitro validation experiments, we present in vivo targeting results from NHP subjects undergoing preclinical gene and cell delivery experiments with post-operative observation periods of months to years. We have applied the proposed computational device tracking and presurgical planning methods during our NHP work on cell delivery for Parkinson's disease [35–37] and viral vector gene delivery to study pathological anxiety [38, 39].

### 3.3 Methods

#### Computational approach to real-time device tracking

In this section we describe how to compute the current alignment of the MR-visible trajectory guide in real time and report it to the operator. The cylindrical alignment stem used in this work is physically simple and its central axis is indicative of the current trajectory. The current alignment can be determined from two points along the stem's central axis. A limited set of 1D spokes are acquired within a known aiming plane to determine the location of the central axis in that plane, referred to as the "stem-plane intersection point" (Fig. 3.3). Repeating this process in a second plane yields the second point necessary to determine the current alignment.

The operator selects a target point and estimates the pivot point of the trajectory guide. Our system prescribes a plane orthogonal to the planned alignment stem orientation (Figure 3.3a). Since the manufactured cross-section of the circularly symmetric alignment stem is known precisely a priori, a precomputed projection of the cross-section can be correlated with each 1D readout (Fig. 3.3b). The location of the peak in the correlation then indicates the stem center location within the radial projection. In practice, rather than perform a correlation in image space, each readout in frequency space is multiplied with the precomputed Fourier transform of the theoretical stem projection. That product is then zero padded and inverse Fourier transformed to yield a sinc-interpolated correlation of the line scan and theoretical stem projection, before processing by the peak finder. A series of radial readouts at different angles is acquired and processed to compute the stem-plane

intersection point (Fig. 3.3c). With typical TRs of 10–12 ms, by acquiring 10–20 radial readouts, the system can compute a new stem-plane intersection point every 100–200 ms.

Repeating this process at one or more additional offset planes defines the central axis of the stem. Finally, the real-time control computer outputs to a monitor that the operator can view while standing beside the scanner bore. This monitor displays the planned aim point and current trajectory to provide visual feedback while the operator is reaching into the bore and adjusting the aim.

### **Pivot point Computation**

Identifying the pivot point is critical; if the pivot coordinates are misidentified, extrapolating the line from the target through the pivot will yield an incorrect aim point (Fig. 3.4a). A further improvement in the rate of updates can be achieved when the mechanical design of the trajectory guide incorporates a fixed (non-translatable) pivot point. In that case, the pivot point can be used as one of the two points that defines the trajectory. Thus, after a precise one-time calculation of that pivot point, only one other point along the alignment stem is needed to determine the trajectory. This offers an update rate advantage over trajectory guide designs that have no fixed pivot, or no MR-visible fiducial at the pivot point.

The trajectory guide is manipulated into multiple distinct orientations (Figure 3.4b–d). At each orientation, the software performed the above process to determine the current trajectory by computing the stem-plane intersection in two distinct planes. This yields a collection of lines that are physically constrained to

pass through the pivot point at the center of the ball joint. These lines do not all intersect exactly (due to noise, physical imperfection, etc.), but a linear least squares method can compute their approximate intersection [40]. This computed pivot point and a single real-time acquisition plane are then used to perform the final aiming step of the prospective stereotaxy procedure.

Precision manufactured glass NMR sample holder tubes (Wilmad-LabGlass, Vineland, New Jersey) were used in place of the plastic alignment stems originally supplied with Navigus bases due to the NMR tubes' excellent physical cylindricity and low cost (Fig. 3.11). The NMR tubes were manufactured to have an outer diameter of 3 mm and we cut them to lengths of approximately 10 cm. We fabricated custom acrylic adapters (Fig. 3.11c,d) to securely couple the NMR tube to the Luer taper inside the distal end of the Navigus ball joint guide tube. All in vitro and in vivo guidance experiments were completed on a 3 T Discovery MR750 scanner (GE Healthcare, Waukesha, WI), using a 10 cm single-channel loop coil (MR Instruments, Inc. Minneapolis, MN).

## **In vitro testing**

We performed in vitro targeting studies using a phantom to characterize the accuracy of pivot point computation and cannula tip placement across multiple trials.

**Pivot point computation** Precision was determined by performing 10 trials of computing a pivot point: manually manipulating the trajectory guide into five different orientations as shown in Figure 3.4b–d, recording the computed trajectory

at each orientation, then computing a pivot from those five trajectories. Neither the patient table nor the phantom platform were moved during the 10 trials, to ensure consistency of the true physical pivot. While it would be ideal if these measurements could be compared to a known-true measurement of the pivot position, it is impossible to ensure that the proximal tip of the fluid-filled cavity in the alignment stem is exactly at the center of the ball joint, so another method is needed to determine the pivot with sub-mm accuracy. Accuracy of the pivot point computation was determined indirectly, by measuring the overall targeting accuracy of the entire guidance procedure, as described next.

**Targeting accuracy** Cannula tip placement accuracy was measured by repeating a guidance procedure 10 times. In each case, a cannula was guided to a target (Fig. 3.5c) consisting of a cylinder machined down to an outer diameter of 1 mm at the tip. The target fits precisely in a target array module inside a small, fluid-filled box ( $55 \times 55 \times 75 \text{ mm}^3$ ) which has a Navigus trajectory guide base attached to its lid (Fig. 3.5d). The box was clamped in a wide, 7.5 kg acrylic platform to prevent the box from moving, which is especially important when manipulating the trajectory guide.

The guidance procedure began with identifying the MR coordinates of the target spike on a 3D roadmap scan. Roadmap volumes were produced by a 3D T1-weighted, Cartesian gradient-recalled echo sequence with inversion recovery preparation, a  $256 \times 224 \times 124$  acquisition matrix ( $0.7 \times 0.8 \times 0.8 \text{ mm}^3$  voxels) in a coronal slab, TE 3.9 ms, TR 9.1 ms, TI 450 ms, and flip angle of  $12^\circ$  with a scan time of 6 min 4 s (hereafter referred to as the “3DT<sub>1</sub>W” sequence).

The approximate pivot point was next manually identified on the roadmap and then refined using the previously described pivot point computation procedure. With the target point and pivot point (red and yellow dots respectively, Fig. 3.2a), our software calculated the planned aim point at which the central axis of the alignment stem would intersect the acquisition plane at an operator-selected slice offset from the pivot (green dot, Fig. 3.2a). In the experiments presented here, the real-time MR device tracking presented five updates per second, displayed on a monitor visible to the operator as they aim the trajectory guide.

Once the trajectory guide was aimed and the locking ring secured, the MR-visible alignment stem was removed and replaced by the remote introducer (RI), a precise linear stage (Medtronic, Minneapolis, MN) used to drive the cannula to the target depth. The linear stage moves smoothly but, when not in motion, the control wheel locks into detents that correspond to 0.5 mm of stage travel. Our software calculated the planned insertion depth using the pivot point, target point, and device-specific information such as the offset between the cannula tip and the physical pivot point when the depth gauge on the RI is zeroed. Finally, the RI was used to advance the cannula to the planned insertion depth (rounded to the nearest multiple of 0.5 mm). After insertion, the 3DT<sub>1</sub>W sequence was repeated to validate the cannula tip location.

To measure the final cannula tip location, the post-insertion 3DT<sub>1</sub>W volumes were opened in 3D Slicer [41, 42] (slicer.org) and the three view planes were reformatted such that the cannula laid in the peri-sagittal and peri-coronal planes, and passed perpendicularly through the peri-axial plane. The 3 mm section of

shaft-tip overlap (illustrated in Fig. 3.5b) creates the darkest negative contrast, with fainter contrast in the shaft above it, and even fainter contrast in the 3 mm tip below it, as seen on MRI in Figure 3.5f. Slicer's ruler tools were used to measure these two 3 mm features to confirm that the cannula tip location had been correctly identified. A point mark was placed at the center of the end of the tip and its 3D coordinates recorded. The retrospective determination of cannula tip placement using reformatted slices [43] and referencing off MRI-visible features based on precisely measured cannula dimensions [44] has been previously described.

## **Preoperative surgical planning**

The anatomy that can be reached is highly affected by skull shape at the site where the base is installed. Careful preoperative planning is critical to ensure that targets will be reachable. Reinstalling bases if targets are unreachable is time-consuming, or impossible if new screw locations would fall inside the initial burr hole. Trajectory guide geometry determines the solid angle of the reachable cone (orange, in Fig. 3.6a,c) and, for orthogonal bases, the cone's central axis will be approximately parallel to the skull outer surface normal vector, depending on which of the base corners are high vs. screwed down flush. To enable the desired trajectories in vivo, we usually employ bases which have the ball joint cylinder angled 15° off orthogonal. Rotating an angled base about the skull surface normal vector also affects the direction of the reachable cone. To ensure targets are reachable, we have developed 3D models and an iterative workflow (described below), the output of which is a map used by the surgeon to install bases on the skull (Fig. 3.12).

When available, subject-specific preoperative MRI volumes were used to model suitable locations on the skull for burr holes and installation of trajectory guide bases. Otherwise, planning was performed using existing MRI volumes from similar age-, sex-, and weight-matched NHPs. When possible, trajectory guides were placed so that each inserted cannula would avoid hazards (such as ventricles, sulci, and the motor cortex) while being able to reach the planned target despite each trajectory guide's limited range of motion [35, 45].

We created physically accurate 3D models of the trajectory guide bases after careful measurement with calipers. A cone with apex angle  $\pm 18^\circ$  was added to the 3D models to indicate the reachable volume given the ball joint's range of motion limits. To create each surgical plan, the preoperative MRI volume and models were loaded in 3D Slicer. Each base was rigidly transformed to orient its bottom surface tangent to the skull, and positioned so that the anatomical target was centered within the base's reachable cone. We determined which corners should be flush or high so that installation of the base would direct the cone axis closer to the target. The resulting map (Supp. Fig. 3.12) shows burr hole coordinates (relative to midsagittal plane and frame ear bars), base rotation, and the direction to each target.

## **In vivo applications**

The proposed guidance method was applied in two distinct experimental surgical protocols requiring precise cannula placement in NHP models: **1)** convection-enhanced delivery of viral vectors to a subregion of the amygdala, intended to



alter anxious temperament in 5 rhesus macaques (3 male, age at surgery =  $2.19 \pm 0.23$  years) [39] and 2) delivery of engineered cells to the substantia nigra to test cell-based dopamine replacement for Parkinson's disease in 4 rhesus macaques with MPTP-induced hemiparkinsonism (4 male, age at surgery =  $15.31 \pm 5.85$  years). The experiments were performed according to the federal guidelines on animal use and care [46] with approval of University of Wisconsin–Madison Institutional Animal Care and Use Committees.

On the day of surgery, before transport to the MRI suite, experimental subjects were anesthetized, placed in an MRI-compatible stereotactic frame, and bases were installed at the stereotactic coordinates determined in the 3D preoperative plan. The surgical procedure and equipment are described in our previous work [6]. The loop coil was secured to the subject's head with the trajectory guide at its center. As described above for the *in vitro* studies, a refined pivot point was computed by sampling multiple trajectory guide orientations. The trajectory guide was then aimed at the anatomical target. However, during *in vivo* experiments, a 3DT<sub>1</sub>W aim confirmation scan was acquired after aiming and, if the aim was deemed acceptable, the cannula was inserted to a partial depth approximately 5–10 mm short of the target. The purpose of the partial insertion was to place the cannula tip in a uniform region of gray or white matter and not in a transitional region, which enabled us to identify the tip and determine the remaining distance to insert without overshooting the target. The partial depth was determined for each insertion by making measurements on the aim confirmation scan after reformatting to yield a peri-coronal plane containing the anticipated trajectory. The 3DT<sub>1</sub>W

scan was repeated after partial insertion, and the volume reformatted to yield a peri-coronal slice showing the cannula in plane. The location of the cannula tip was visually identified and the remaining insertion depth to the target was measured. Finally, the cannula was advanced to the target before payload delivery and confirmatory imaging. These two surgical protocols primarily used the same hardware and methods, but the ways in which they differ are described in the following paragraphs.

**Viral vector gene delivery for treatment of anxiety disorders:** The amygdala has a recognized role in the expression of NHP anxiety [47], and amygdala dysfunction in humans has been linked to psychopathology [48]. To understand the effects of amygdala inhibition on the expression of primate anxiety, we performed MRI-guided infusions [39] using the proposed computational guidance method to deliver a viral vector carrying a chemogenetic payload. The dorsal amygdala region and the planned location for one of the trajectory guide bases are shown in the preoperative planning visualization of Figure 3.6a,b.

Bilateral 24  $\mu\text{L}$  infusions were delivered at 1  $\mu\text{L}/\text{min}$  to the target site in the dorsal amygdala, encompassing the central nucleus and dorsal aspects of the basolateral nuclei of the amygdala. As described in our previous publication [39], infusate consisted of adeno-associated virus AAV5-hSyn-HA-hM4Di (at titer of  $6.28 \times 10^{13}$  genome copies/mL) in saline vehicle with 0.66 mM gadolinium contrast agent (gadobenate dimeglumine) to visualize the spatial distribution of infusate by making it appear hyperintense on intraoperative monitoring 3DT<sub>1</sub>W MRI. Gadolinium contrast agent signal on intraoperative MRI is highly correlated with expression

of genes delivered by AAV2 vector [49]. We report post-operative analysis of the effects of gene therapy and post-mortem analysis of the tissue to confirm localized gene delivery [39].

**Engineered cell delivery for treatment of parkinsonism:** The proposed computational guidance method was also used to deliver engineered cells into the substantia nigra (SN) with the goal of successful implantation. The delivered cells were allogeneic induced pluripotent stem cell-derived midbrain dopaminergic neuroprogenitor cells (mDA-IPSCs). Cells were delivered in two deposits of 5  $\mu$ L each, along a single cannula track, to precise locations inside the medial border of the SN, unilaterally in the dopamine depleted hemisphere. Approximately 10–15 million cells were delivered to each subject. Because this study used live mDA-IPSCs, one goal was to minimize the idle time cells spent in the cannula, which necessitated rapid delivery from lab bench to brain. No gadolinium contrast agent was co-infused with the cells, thus the 3DT<sub>1</sub>W scan has less sensitivity to depict injections, but a T<sub>2</sub>W sequence could be used to better depict the fluid around the cells. The SN and planned trajectory guide base location for this experiment are shown in the preoperative planning visualization of Figure 3.6c,d. In our previous work, we describe the in vivo PET and postmortem histology methods that were used to show successful implantation of similar cells after delivery to the putamen using this IMRI method [36].

## 3.4 Results

### Pivot point computation

#### In vitro experiments

Computing the pivot from several lines, which are in turn determined by precisely computed stem-plane intersection points, allows us to repeatedly compute pivot points with variation across trials well below 0.1 mm (smaller than the voxel dimensions of the 3DT<sub>1</sub>W scan used for imaging). The repeatability of pivot point computation in vitro is visualized by plotting the de-measured point cloud in Figure 3.7a,b. In the radial plane, Bessel's corrected sample standard deviation  $s = 0.03$  mm, with no point deviating from the mean by more than 0.05 mm. Along the depth direction,  $s = 0.05$  mm, with no point deviating from the mean by more than 0.08 mm. For these guides, it is expected that variation will be greater in depth than in the radial direction (Fig. 3.13).

#### In vivo experiments

Across the nine in vivo experiments, the cannula tip was successfully placed at all 14 targets after a total of 18 rounds of aiming. For 12 targets, the planned aim was achieved and the cannula inserted after the first round of aiming. The remaining two targets required six rounds of aiming before insertion due to the following issues: 2× replacing faulty hardware; 1× target anatomy shifted to different scanner coordinates; and 1× the 3DT<sub>1</sub>W aim confirmation scan predicting  $\approx 1.1$  mm lateral error (the experimental protocol entailed re-aiming if predicted lateral error

>1 mm). One round of aiming was performed without computing a pivot, using the manually selected pivot, for a total of 17 computed pivots. Examining the 17 instances of pivot computation (Fig. 3.8a,b), the manually identified approximate pivots differ from the computed pivots in the radial direction by  $0.53 \pm 0.43$  mm (mean  $\pm$  s), with a maximum deviation of 1.71 mm.

## Targeting results

### In vitro experiments

Figure 3.7c–e shows targeting results from 10 experiments aiming to place the cannula tip on a 1.0 mm cylindrical target at a depth of 48.3 mm from the pivot. The first trial shows the greatest radial error, <0.7 mm, which is still less than the voxel size of the 3DT<sub>1</sub>W scan used for intraoperative planning and monitoring. The subsequent nine trials are more tightly clustered together, with the greatest radial error in that group being <0.4 mm. No depth error exceeded 0.6 mm. Expressed in angular units, which are independent of depth, the radial error of the first trial is 14 mrad, and the subsequent group of nine has error ranging from 3.4–7.7 mrad. Inset in lower left quadrant of Figure 3.7d highlights the pivot precision by resizing the pivot computation repeatability plots of Figure 3.7a,b to match the scale of tip placement results in Figure 3.7d,e for direct visual comparison.

### In vivo experiments

Results of the five gene-delivery surgeries are shown in Figure 3.9. The objective was to deliver viral vector to the dorsal amygdala, encompassing the central nucleus

and dorsal aspects of the basolateral nuclei of the amygdala, as shown in Figure 3.9b. A typical infusion in a single subject is shown in Figure 3.9a and Figure 3.9c shows the infusion overlap across all subjects, indicating thorough coverage of the target region. Postmortem verification of the infusate delivery, transfection by the viral vector, and subsequent expression of delivered genes is demonstrated by the histology, autoradiography, and in vivo deschloroclozapine PET imaging in our previous work [39].

Cells were injected unilaterally in the SN of four NHP subjects. Peri-coronal views during a representative surgery show the aligned trajectory guide and targeted SN prior to cannula insertion (Fig. 3.10a), after partial insertion (Fig. 3.10c), and after full insertion and deposit of the cells (Fig. 3.10d,e). In the 3DT<sub>1</sub>W validation scan, due to the artificial CSF in which the cells were suspended, the inversion recovery sequence causes negative contrast in the region where the cells were delivered. Subjects were maintained for  $1.37 \pm 0.30$  years (mean  $\pm$  SD) of observation before necropsy. Analysis of PET, histology, and parkinsonism symptoms will be reported elsewhere.

### 3.5 Discussion

In this work, a computational tracking method was developed for aiming neurosurgical trajectory guides in conventional diagnostic MRI scanners, and the method was validated in vitro and in vivo. Rather than imaging the entire device and fitting a 3D model of the trajectory guide to the image volume, the proposed method uses

a priori information about the hardware and a small set of MR measurements to compute the trajectory indicated by the alignment stem. After a one-time computation of the non-translatable pivot point, the system then presents the operator with real-time interactive feedback about the adjustments needed to precisely align the trajectory guide with the intended target.

The proposed method has been successfully applied to achieve sub-millimeter accuracy in preclinical procedures including gene and cell delivery. The proposed IMRI method enables researchers to monitor the infusate delivery and verify that the intended target was successfully treated. Without IMRI, such verification would not typically be achieved until post-mortem histological assessment of the brain tissue.

### **Applicability to other trajectory guides**

We expect that the proposed method could be applied to other trajectory guides that have a linear MR-visible feature indicative of the current trajectory. The ball-joint guide array [50] is mechanically similar to the Navigus, and the version that has an MR fiducial along its central axis [51] should be readily adaptable to this method. For trajectory guides that have both translational and rotational degrees of freedom such as the SmartFrame [52] or GantryMate [43], this method would require two acquisition planes along the trajectory guide fiducial, with a proportionally slower update rate.

### **Predicted tip error**

The differences between manual and computed pivots in vivo are shown in Figure. 3.8a,b. Taking the computed pivot to be representative of the true physical pivot, if a refined pivot had not been computed and the trajectory guide had been aimed based only on the manually selected pivot (with our typical aiming offset of 50 mm), the radial error of the inserted cannula tip would be expected to range from 0.07–3.13 mm, with mean radial error of 0.95 mm (Fig. 3.8c). More generally, the radial errors can be expressed in angular units that are independent of depth. Radial error in milliradians would range from 1.8–75.5 mrad, with mean of 26.2 mrad. For reference, at a target depth of 40 mm (typical in our NHP experiments), a 1 mm radial error is an angular error of 25 mrad.

### **Benefits of this method**

This method provides rapid and accurate alignment, objective determination of the pivot and stem-plane intersection points, accurate and detailed preoperative planning that eases the difficulties associated with mounting a trajectory guide to the curved skull, and increased update rate.

**Tip placement accuracy:** our in-vitro tip placement accuracy compares favorably to our previous image-based work [6], and is similar to that reported for commercial systems in humans [17, 44]. Objective determination of stem-plane intersection and pivot spares the operator from trying to subjectively determine those points visually. Our radial errors of (min, mean, max) = (3.4, 6.1, 14.0) mrad



are comparable to the radial errors of cannula tip placement recently achieved by another lab, (0.7, 6.2, 17.2) mrad, using a mechanically similar trajectory guide across 22 insertions in humans [51]. Ignoring the first-trial outlier, our radial error is evenly distributed along the anterior-posterior axis, but the mean of that group is biased 0.24 mm (4.9 mrad) right of the target. This systematic error is smaller than both our maximum allowable tip placement error (1 mm) and the voxel size of the 3DT<sub>1</sub>W scan used during IMRI. We plan to identify the cause of this systematic error and compensate for it. Experiments by another lab with a mechanically similar trajectory guide have also observed a small bias in their mean cannula tip placement (posterior, slightly right and slightly superior to their targets) across 15 insertions in NHPs [50].

**Physically accurate preoperative planning:** our 3D models of trajectory guide bases enable careful planning that has ensured our ability to reach the intended targets. The utility is fully realized when using a preoperative MRI from the same subject, as in the cell delivery experiments, but it has also worked well when planning on an MRI from a sex-, age-, and weight-matched subject that is comparable to the surgical subject (when preoperative MRI is unavailable, as in most of our gene delivery experiments).

**Increased update rate:** the proposed method reduces the operator fatigue experienced in our previous image-based real-time method, which required waiting for 5 sec between image updates to see the result of aiming movement. This method requires some additional time to compute the pivot once ( $\approx 2$  min), but manipulat-

ing the trajectory guide into different orientations takes only a few seconds of that time, so the operator can rest during the data collection periods between trajectory guide manipulations.

The success of the proposed method is supported by the precise insertion of cannulae into neurosurgical targets in over 71 surgeries in NHPs [35–39], and by the quantification of accuracy in experiments with a rigid phantom.

### **3.6 Conclusions**

We have proposed a method for rapid computational determination of device alignment and demonstrated its successful application in neurosurgeries on NHPs. The approach provides real-time feedback on device orientation at an interactive rate (5 Hz) which, compared to fully-sampled IMRI techniques, is closer to that of the rapid tracking enjoyed by neurosurgeons in stereotactic operating rooms.

The data presented here emphasize the value of real-time MR guidance and intraoperative MRI validation of the spatial distribution of experimental therapies in animal models, as compared to the limitations of stereotactic surgery without MRI.

### **3.7 Acknowledgments**

We thank our coworkers Carissa A. Boettcher, Victoria R. Elam, Eva M. Fekete, Rothem Kovner, and Matthew R. Rabska, as well as the veterinarians, animal care staff, and MRI technologists for their assistance in conducting this research. We

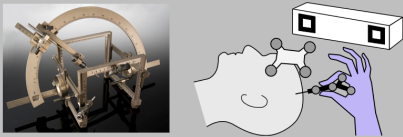

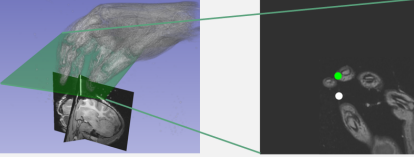
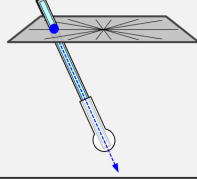
thank the developers of Vurtigo, especially Labonny Biswas, and the developers of RTHawk, especially Juan Santos and William Overall, for their help in understanding and troubleshooting those platforms such that we could build on them to develop our own software and perform this work. We also acknowledge institutional support that GE Healthcare provides to the University of Wisconsin–Madison.

The research was supported by the UW WARF Accelerator program and National Research Service Award (NRSA) T32 EB011434. Specifically, during the development of this computational tracking method, M.E.O. was funded by the University of Wisconsin–Madison’s Clinical Neuroengineering Training Program.

This work was supported by NIH grants R01-MH046729 and R01-MH081884 to N.H.K., Research reported in this publication was also supported in part by the Office of the Director, National Institutes of Health under award number P51OD011106 to the Wisconsin National Primate Research Center, University of Wisconsin–Madison.

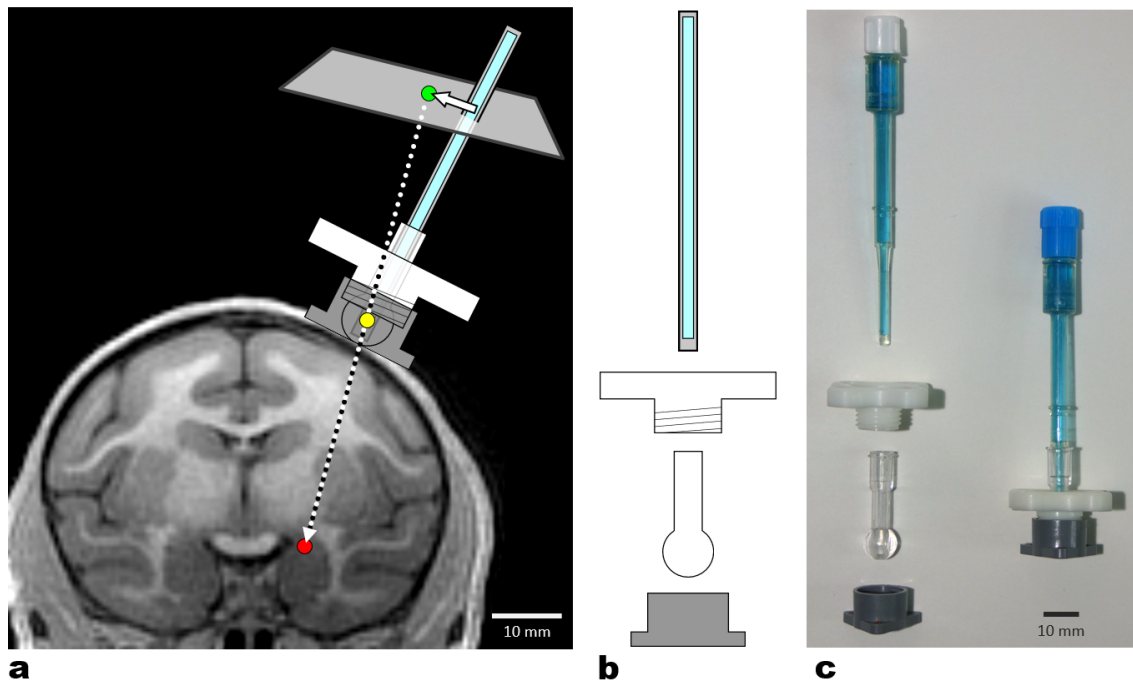
Support was also provided by R01NS076352, U54 HD090256 of the Falk Trust, the University of Wisconsin–Madison Office of Vice Chancellor for Research and Graduate Education, and the Departments of Radiology and Medical Physics at the University of Wisconsin–Madison.

### 3.8 Figures and Tables

Method	Setting	Approximate period for updates [s]
Conventional stereotaxy <b>a</b> 	Operating Room (without intraoperative tomographic imaging)	0.03
3D IMRI prospective stereotaxy <b>b</b> 	Inside bore of conventional diagnostic MRI scanner	60–300
2D IMRI prospective stereotaxy <b>c</b> 		3–5
Proposed MR-based computational tracking prospective stereotaxy <b>d</b> 		0.2

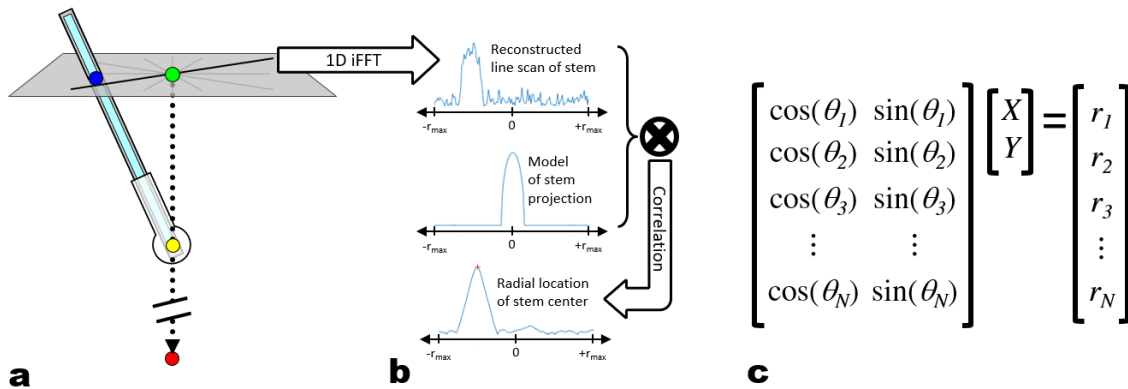
**Figure 3.1: Existing methods for neurosurgical device alignment vs. the proposed MR-based computational tracking.**

(a) Classical techniques that use a stereotactic frame [53], have given way to the modern standard of frameless neuronavigation techniques which use optical cameras or other sensors to rapidly track interventional devices and render the predicted trajectory overlaid on preoperative planning tomographic image volumes. (b) 3D prospective stereotaxy entails acquiring and processing MRIs of an MR-visible trajectory guide to determine a manipulation of the guide that will align it with the target. This process iterates until the alignment is acceptable and manipulation is no longer needed. (c) 2D prospective stereotaxy illustration. High-resolution images in aiming plane (green) show alignment stem cross-section (white dot) as it is moved toward aim point (green dot) by manipulating the guide. High sensitivity to trajectory adjustment requires high-resolution images, leading to slow update rates. Superimposed hand MRI dataset [54] represents operator's hand during aiming. (d) The proposed method updates rapidly by computing the current trajectory from a set of 1D MR measurements, without need for fully sampled imaging.



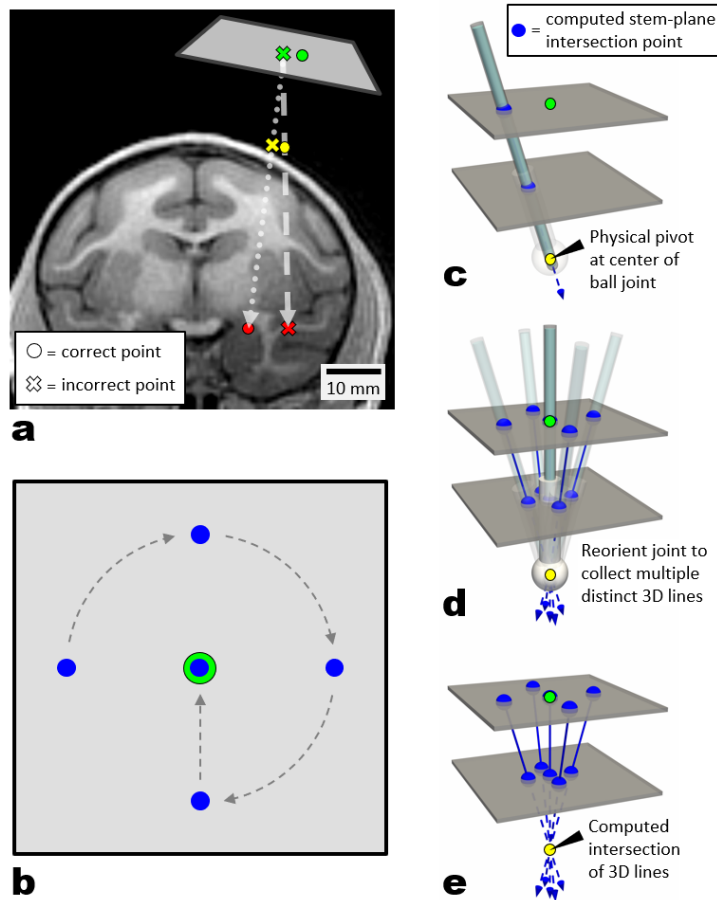
**Figure 3.2: Prospective stereotaxy method and trajectory guide hardware.**

(a) An aim point (green dot) is calculated by extending a line from the chosen target in the dorsal amygdala (red dot) out through the pivot point (yellow dot), which must be identified. The dotted arrow shows the planned trajectory, and the solid arrow indicates the manual adjustment needed to reorient the alignment stem along the planned trajectory. (b) The trajectory guide consists of (from bottom to top) a skull-mounted base, guide tube with pivoting ball joint, lock ring to immobilize ball joint, and an alignment stem filled with MR-visible fluid (light blue), as shown in this simplified exploded schematic and (c) photograph (exploded and assembled).



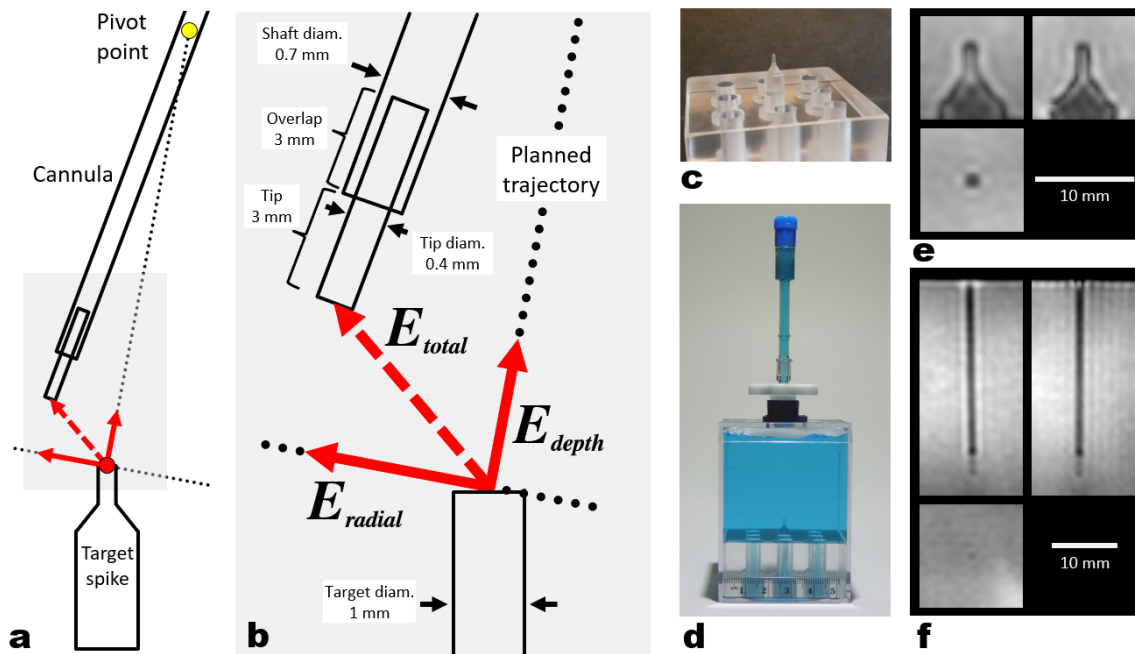
**Figure 3.3: Computation of the stem-plane intersection.**

The alignment stem couples to the ball joint within the trajectory guide and intersects the acquisition plane (gray) at blue dot (a). The acquisition plane is prescribed perpendicular to the planned trajectory (dotted line). (b) Applying a 1D inverse Fourier transform to a radial readout would reconstruct a line scan. Correlating the line scan with a model of the alignment stem projection enables a simple peak finder to detect the center location of the stem along each radial readout. In the proposed method, instead of doing a correlation in image space as depicted, it is accomplished via multiplication in the frequency domain. (c) The in-plane location of the stem center ( $X, Y$ ) is calculated from the overdetermined system of equations arising from the MR readout angles ( $\theta_i$ ) and the detected peak radial locations ( $r_i$ ) at those angles.



**Figure 3.4: Computation of a refined pivot point.**

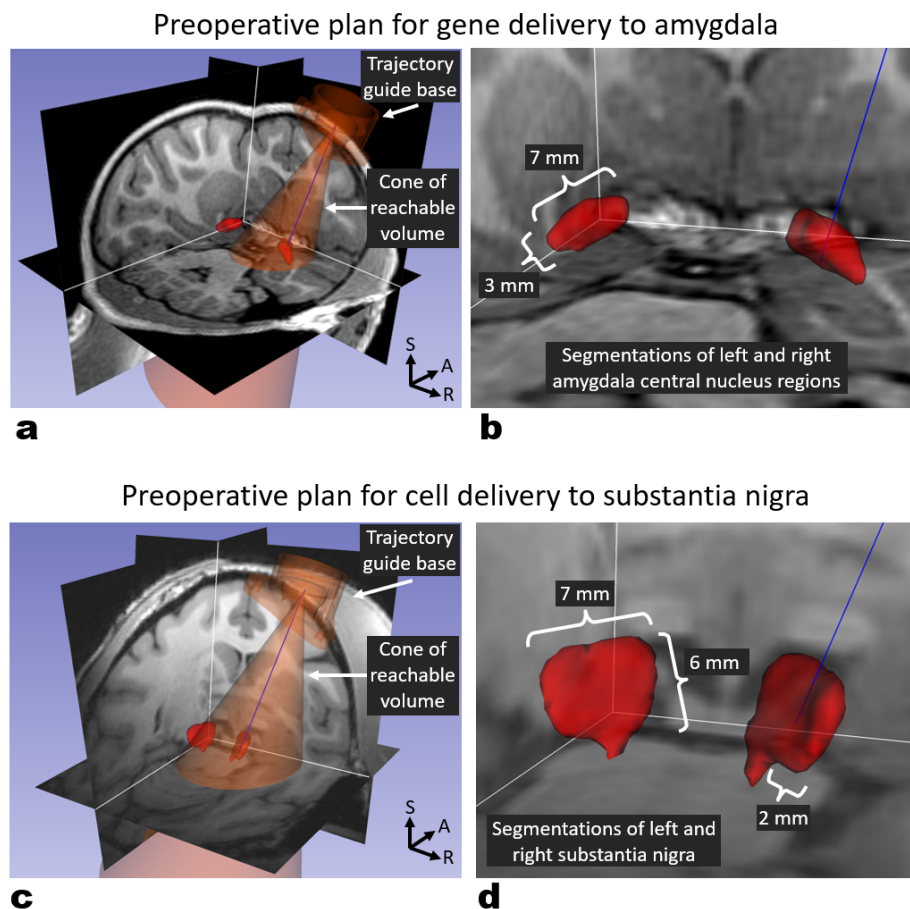
Manually selected pivot points are inherently imprecise, and error in the pivot point results in magnified error at target depth, as illustrated on preoperative MRI (a). For the dorsal amygdala target, (red dot) extrapolating out along dotted line through an incorrectly chosen pivot (yellow X) will result in an incorrect aim point (green X). The interventional device will pass through the true physical pivot point (yellow dot). If aligned with the aim point that is based on an incorrect pivot, it will follow the dashed line trajectory, placing the tip at an incorrect target (red X). (b) Illustration of operator's view of acquisition plane, showing aim point (green) and a progression (dashed arrows) of five stem-plane intersection points (blue dots) as the ball joint is reoriented. (c) Computing stem-plane intersection points (blue dots) at two positions along the stem's length yields a line (blue arrow) representing the current trajectory. (d) The distinct trajectory guide orientations are recorded, and since all trajectories are physically constrained to pass through the pivot point (the center of the trajectory guide's ball joint), computing the intersection of those 3D lines yields that pivot point (e).



**Figure 3.5: Determination of tip placement error.**

A simplified illustration shows a 2D view of the target spike, cannula, and tip placement 3D error vectors (red arrows) used in the phantom study of accuracy (a). The planned trajectory passes through the pivot point, down to the target spike. That trajectory line and its perpendicular plane are indicated with dotted black lines. A close-up view (b) of the gray box in (a) shows the depth and radial error vectors (solid red arrows) obtained by projecting the total 3D error vector (dashed red arrow) onto the trajectory vector, and the perpendicular plane, respectively. A close-up photo (c) of the target spike in the central position of the array block and a photo of the array block inside the precision testing box with a trajectory guide attached to the lid (d) illustrate the size and shape of the target. 3D T1-weighted inversion recovery MRI volumes are used to identify the target point before aiming, as well as the cannula tip after insertion. The target point at the tip of the spike is identified by viewing oblique slices aligned with the target tip (e), and similarly, the cannula tip location is identified by viewing oblique slices aligned with the cannula (f). The cannula tip location is visually determined by the presence of darker negative contrast in the 3 mm overlap section, and fainter negative contrast in the 3 mm tip.



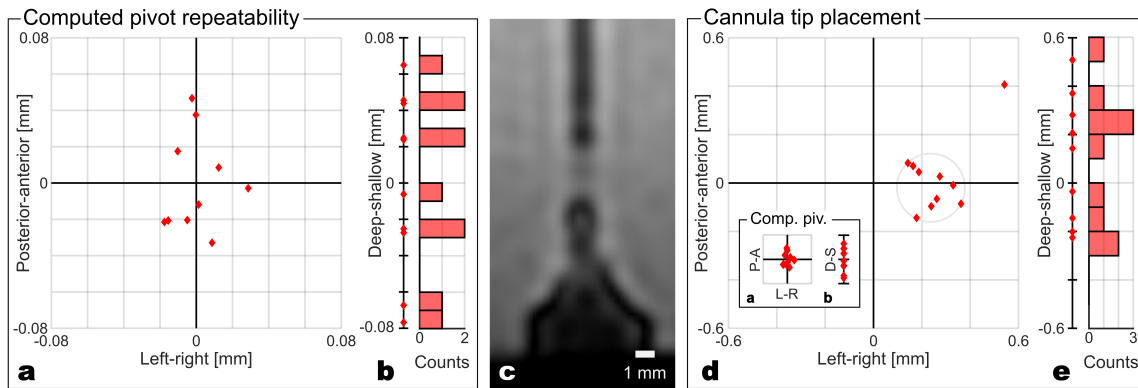


**Figure 3.6: Preoperative plans for gene delivery into amygdala and cell delivery into substantia nigra.**

Three-plane views showing the completed 3D preoperative plans. Segmentations (red) of anatomical structures are used for target identification. Trajectory guide bases, and cones depicting their reachable volume, (orange) are placed to account for skull curvature.

(a) The amygdala central nucleus region is shown in red. The planned trajectory is indicated by a 34 mm blue line starting from the pivot point at the center of the ball joint, within the trajectory guide. Close-up view (b) depicts the prolate spheroid shape of the amygdala central nucleus region, which measures approximately 7 mm long with a 3 mm diameter in this subject. The trajectory line terminates on the ventral edge of the segmented region, at the targeted interface between dorsal and ventral amygdala.

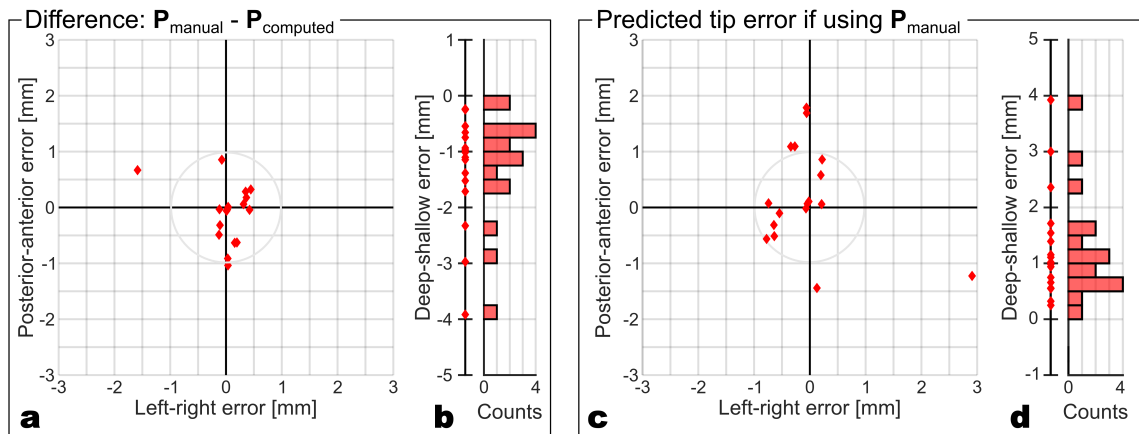
(c) The substantia nigra is shown in red. The planned trajectory is indicated by a 39 mm blue line. Close-up view (d) depicts the dished shape of the SN, which measures approximately 7 mm long, 6 mm tall, and 2 mm thick in this subject. The trajectory line terminates inside the compacta subregion (SNC) on the medial side of the right SN.



**Figure 3.7: In vitro precision and accuracy.**

The repeatability of the computed pivot is shown by plotting the de-meanned point cloud from 10 independent trials of pivot computation (a, b). (a) The 2D scatter shows the radial variation of the computed pivot points and (b) the 1D scatter and histogram show the variation along the depth direction.

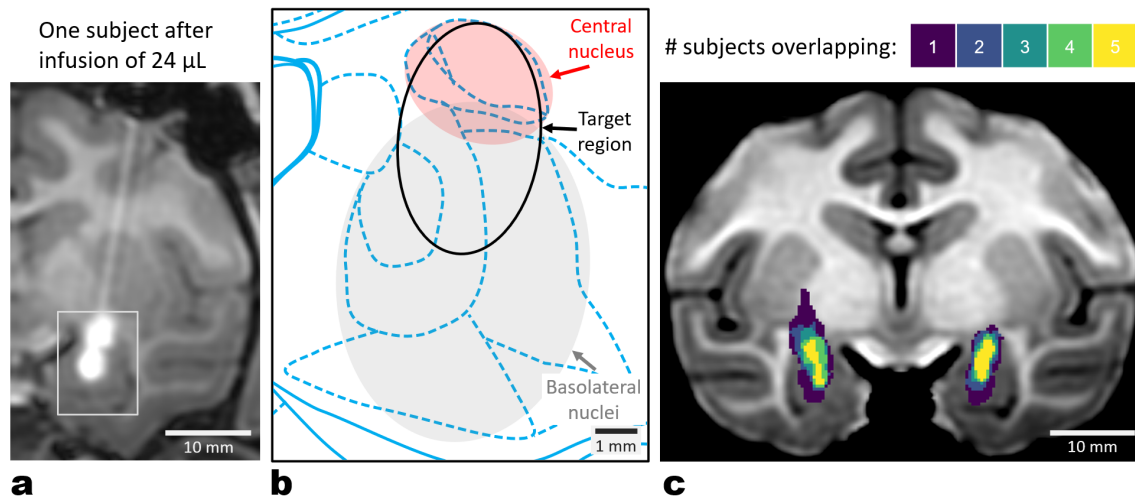
In vitro cannula tip placement is shown in c–e. (c) 3DT<sub>1</sub>W MRI of the cannula after insertion toward the 1 mm diameter spike target. (d) Radial and (e) depth error of the cannula tip after aiming at the spike target and inserting, exhibiting a small bias to the right of the target. The first trial had the greatest radial error and the subsequent nine are more tightly grouped, falling within a circle (gray) of radius 0.14 mm at target depth of 48.3 mm. Expressed as an angular measure that is independent of target depth, those nine trajectories are within 2.9 mrad of the circle center. Inset within (d) shows the data from (a, b), resized to match the scale of (d, e) for comparison, emphasizing that the computed pivots are more tightly clustered than the cannula tip locations.



**Figure 3.8: In vivo pivot computation and predicted inaccuracy.**

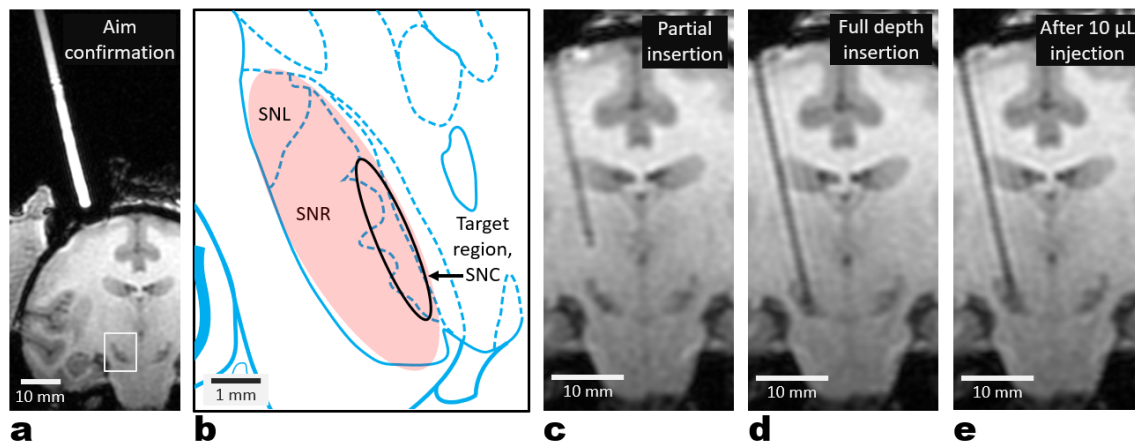
In vivo results over 17 instances of pivot computation show how the manually selected pivot ( $P_{\text{manual}}$ ) differs from the computed pivot ( $P_{\text{computed}}$ , at origin) for each trial in the (a) radial and (b) depth directions. The gray circle ( $r = 1$  mm) shows that two manual pivots had  $> 1$  mm of radial error with respect to the computed pivot. In all cases, the manually selected pivot was deeper than the computed pivot.

To illustrate the importance of correctly determining the pivot, the predicted (c) radial and (d) depth error in tip placement is modeled under the assumptions that 1) the computed pivot is the true physical pivot, but 2) the trajectory guide is aimed based on the manual pivot, then 3) inserted with no deflection. The six trials outside the gray circle were predicted to result in  $> 1$  mm radial error with respect to the target if the pivot refinement procedure had been omitted.



**Figure 3.9: Visualization of gene delivery infusions.**

An intraoperative T1-weighted MRI, with hyperintense signal from the co-infused gadolinium contrast agent, highlights the extent of the infusion cloud around the cannula tip in the left amygdala from one subject in the gene delivery study (a). White rectangle in (a) approximately corresponds to the anatomical atlas illustration of the amygdala sub-nuclei (b). The intended treatment region (black-outlined oval) in the amygdala includes the central nucleus (red, as in fig. 6) and dorsal aspects of the basolateral nuclei (gray oval). Adapted with permission from Paxinos et al. rhesus atlas [55], figure 58. (c) The overlap map shows the concordance of infusions across all five subjects after deformable coregistration of the IMRI volumes using Advanced Normalization Tools [56]. Purple voxels indicate Gd signal from only a single subject, yellow indicates overlap across all five subjects. Backflow in one subject causes greater extent of purple region in right hemisphere. Adapted with permission from Roseboom et al. 2021 [39].

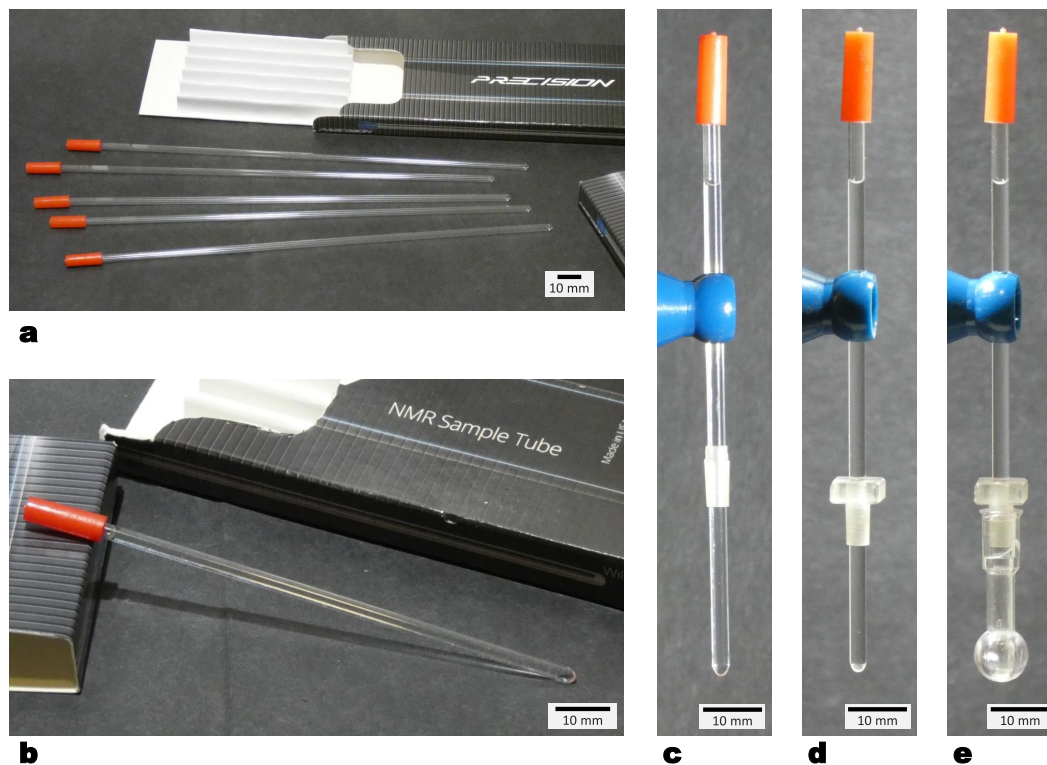


**Figure 3.10: Visualization of cell delivery process.**

An aim confirmation scan (T1-weighted, CSF-nulling IR) is acquired after aiming and locking the trajectory guide. A peri-coronal view from an oblique slice through the middle of the stem (a) allows the operator to verify, before inserting the cannula, that the alignment stem and target location in the substantia nigra (SN) are indeed collinear. An anatomical atlas illustration of the SN subregions (b) approximately corresponds to the white box area in (a). The SN is highlighted in red (as in Fig. 3.6), and the intended treatment region (black oval) corresponds to the SN pars compacta (SNC) subregion, which is medial to the larger pars reticulata (SNR) and lateral (SNL) subregions. Adapted with permission from Paxinos et al. rhesus atlas [55], figure 69.

Another MRI volume is acquired after the cannula is inserted to a partial depth (c). The cannula's negative contrast against the brain parenchyma allows the operator to determine the current position of the tip and measure the remaining distance to the target. After advancing the remaining 8 mm to this target, another 3D volume (d) is acquired to verify that the cannula tip has been successfully placed in the thin, obliquely oriented SNC target. A final MRI volume (e) is acquired after injecting cells suspended in artificial CSF. Two 5  $\mu$ L deposits were injected, with the cannula retracted 1 mm between deposits. The delivered volume is smaller than in the gene therapy experiments (Fig. 3.9), and there is no Gd contrast agent in the injection.

### 3.9 Supporting Figures and Tables

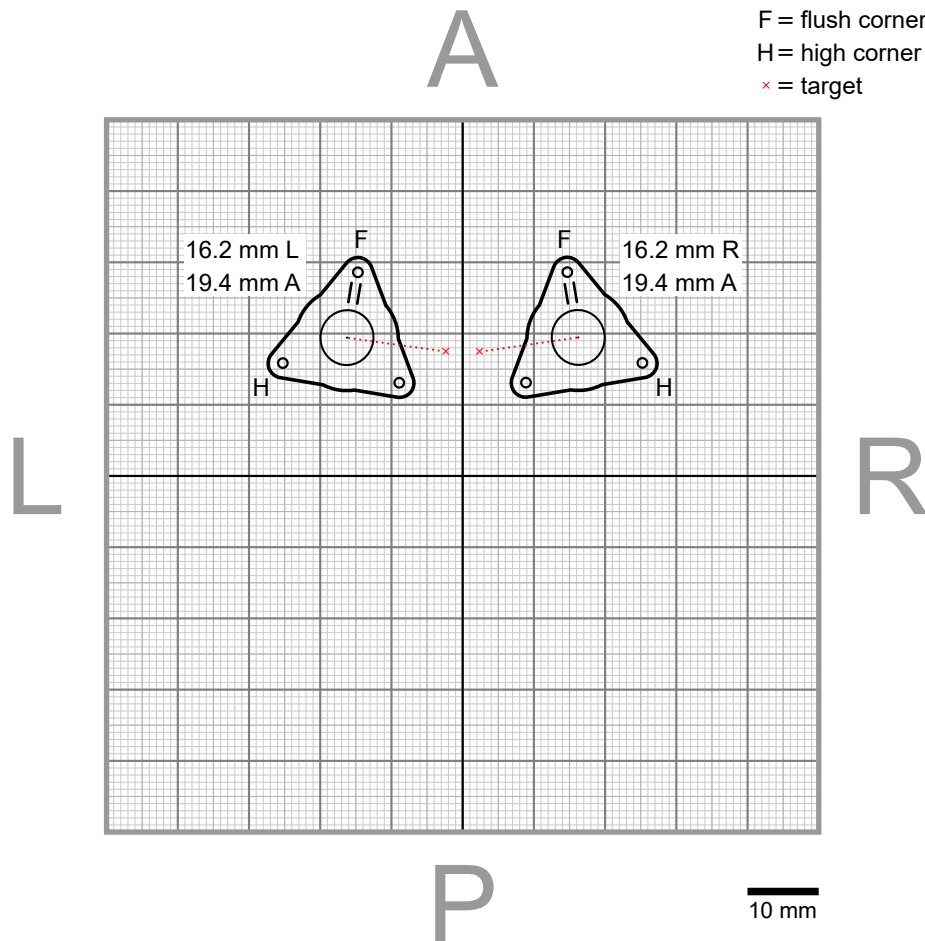


**Figure 3.11: NMR sample tubes and adapter cones used in place of original plastic alignment stems.**

(a) The shortest factory NMR tubes are longer than necessary. (b) After snap cutting to a length of 10 cm and filling with Gd-doped water, the NMR tube is ready for use. The acrylic adapter cones are shown (c–e) after slipping onto an NMR tube (which is held vertically by a small blue support arm for these photos). The inner diameter of the cones is just large enough for a tight sliding fit that can easily support the weight of the adapter, and the outer taper matches the Luer taper inside the guide tube. (c) Our early adapters were simply a truncated cone, with no head to grab. (d) Current adapters have a squared off head (approximately  $7 \times 7 \times 3 \text{ mm}^3$ ) which facilitates pinching and twisting to remove from the guide tube, and prevents the cone from rolling around when set down on a flat surface. (e) The dimensions are such that the cone achieves a snug fit before the square head would impinge on the outer lip of the guide tube, or the narrow end of the cone would contact the end of the guide tube's internal taper.

Subject ID: \_\_\_\_\_

Date: \_\_\_\_\_



**Figure 3.12: Example of a surgical map used for placing bases.**

This surgical map was used in the OR to perform the base placement for one of the gene delivery subjects in this work. With the subject in the sphinx position, the ear bars of the head frame define the anterior–posterior axis zero, and the sagittal crest (at 0 mm anterior) defines the left–right axis zero (black lines). The burr hole center coordinates are given (16.2 mm lateral of the midline, 19.4 mm anterior for both bases) and the outlines of the bases indicate how they should be rotated about the normal to the skull surface. Annotations indicate which corners are expected to be tightened down flush to the skull surface vs. those that will be high. The gaps between the skull surface and bottom face of the base are typically 0–2 mm at the location of the screws. Targets and trajectories are illustrated to help the surgeon determine where to cut and fold the dura out of the way so that the dura flap would not block cannula insertion later at the MRI.

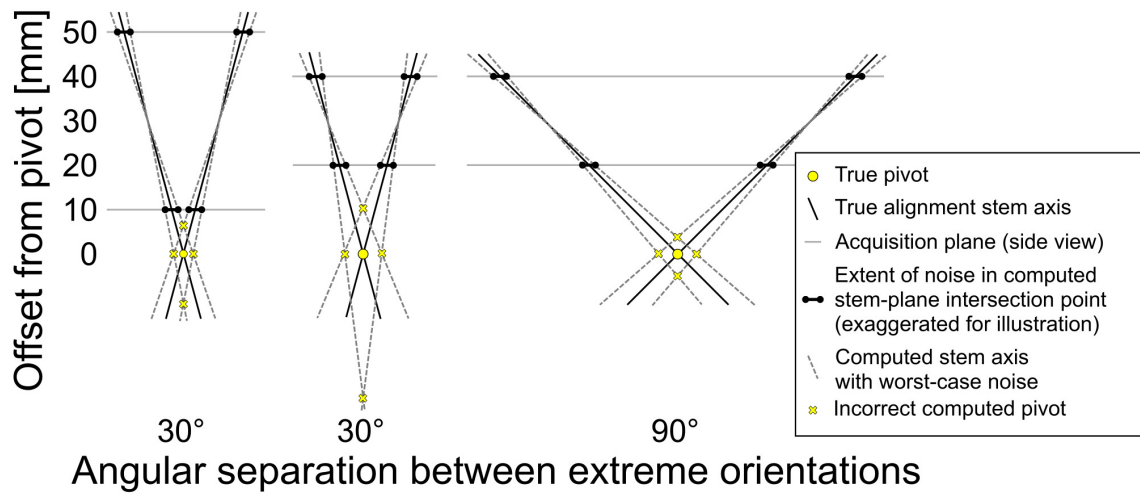


Figure 3.13: **Geometric explanation of error distribution in pivot computation.**

A simplified 2D illustration explaining why the computed pivot repeatability experiment shows more depth variation than radial variation. Comparing (a) and (b): for a given angular separation (e.g.,  $30^\circ$ ) between the trajectories, using (a) offsets of 10 and 50 mm will more tightly bound the worst-case computed pivot than (b) offsets of 20 and 40 mm. Comparing (b) and (c): for given offsets, if the trajectories are (c) perpendicular, the worst-case computed pivot is more tightly bound than if the trajectories are (b) closer to parallel. Hence, we use near and far offsets (usually 10 and 50 mm), and orient the trajectory guide at its extreme range of motion limits when computing the current trajectory during the pivot computation step.



## 4 INTRACEREBRAL HEMORRHAGE EVACUATION

---

In the previous chapters I described our novel developments for preoperative planning and intraoperative tracking and monitoring. Now I describe the development of an in vitro model of intracerebral hemorrhage (ICH) and the use of this model to develop and explore new MRI-based approaches to preoperative planning and clot characterization, as well as intraoperative monitoring during delivery of a clot-dissolving agent.

Portions of this chapter have previously been presented at the 2018 Interventional MRI Symposium:

- **Miles Olsen**, Jennifer Meudt, Robert Weyker, Morgan McCue, Robert Moskwa, Terrence Oakes, Ethan Brodsky, Dhanansayan Shanmuganayagam, Azam Ahmed, and Walter Block. "Feasibility Study of MR Image-Guided Intracerebral Clot Evacuation". In: *the 12th Interventional MRI Symposium*. Page #23 of proceedings. 2018

### 4.1 Abstract

**Purpose:** Intracerebral hemorrhage (ICH) is the stroke subtype with the highest mortality rate, and current clinical treatment is often limited to imaging and stabilizing patients, rather than performing an intervention to directly reduce the hemorrhage volume. An emerging therapy is minimally invasive surgery to periodically administer a clot lysing agent, tissue plasminogen activator (TPA), and drain off dissolved clot. While the MISTIE

**Methods:** We investigated solutions to various problems that arose in this early-stage ICH project:

Sources of fresh blood: swine sacrificed at WIMR after use in research and training for X-ray guided heart catheterization procedures, non-sacrificial blood draws from large swine at the UW's breeding facility off campus, and routine swine exsanguination at the on-campus slaughterhouse operated by the Meat Science Department.

Means of physically holding the clotted blood during scanning and mock surgery: syringes/vials, agarose gels, salt dough modeling compound, and large clots in tight-fitting plastic boxes, with negligible surrounding blood serum.

Methods for TPA delivery: manual injection through a 3 mm-wide catheter, and convection-enhanced delivery (CED) through a 0.7 mm-wide cannula at flow rates of 12, 20, and 50  $\mu\text{L}/\text{min}$ .

And tools needed to carry out an in vivo study in swine: a suitable model of the large-bore (3 mm) catheters used clinically for ICH evacuation, replacements for the out-of-production remote introducer linear stage, poseable arms to hold MR-visible fiducials for burr hole site selection, a way to clearly mark the skull surface for accurate burr hole drilling.

**Results:** The slaughterhouse is capable of providing large quantities of blood, but presents a logistical problem in synchronizing with MRI scanner availability.

As a sample of fresh swine blood ages, approximately half of the initial volume will convert into a fibrous clot which is then floating in the other, serous half. This makes it challenging to perform mock surgery in vitro, as hitting the clot with

an interventional device is like bobbing for apples. The agarose gels tested were unsuitable as an in vitro model, because their smooth-and-firm-walled voids do not grip the clot and cannot prevent it from moving. Salt dough is more compliant but still does not quite mimic the environment of the brain. Large clots secured snugly in plastic boxes are even less like the brain but, crucially, they immobilize the clot which enables mock surgeries to be performed.

**Conclusion:** Blood from slaughtered pigs, or large blood draws from donors, should be immediately treated with anti-coagulants and refrigerated until scanner availability permits the start of an experiment, at which time clotting can be initiated chemically. Enclosing large clots in boxes allowed us to test manual injection as well as convection-enhanced delivery (CED) of TPA into a clot

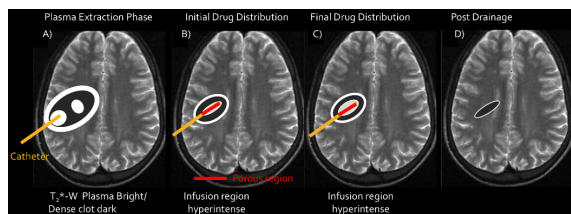
## 4.2 Feasibility Study of MRI-Guided ICH Evacuation

### **Purpose:**

Typically, the current clinical treatment of intracerebral hemorrhage (ICH) merely stabilizes the patient's condition, resigning them to a lifetime of considerable cognitive deficits, motor deficits, loss of independence, and extended care costs. However, a recent large-scale NIH trial, termed MISTIE (Minimally Invasive Surgery Plus rt-PA for Intracerebral Hemorrhage Evacuation)[57], shows promise in minimizing the brain damage by lysing the interior of the clot with a minimally invasive catheter, inserted through a small burr hole not much wider than the catheter, which slowly

delivers clot-busting drugs and drains the lysed blood. CT surveillance is used daily to plan dosages and catheter movements that will avoid dangerously lysing the exterior of the clot and creating a new bleed. The inability of CT to visualize the clot components or the spatial distribution of the clot buster drug leads to very conservative dosing, slowly administered over 3–5 days, with highly variable patient outcomes.

We investigate here whether the soft tissue contrast of MR would advance the MISTIE approach by spatially visualizing blood clot components and the location of administered drugs, as illustrated in Figure 4.1:



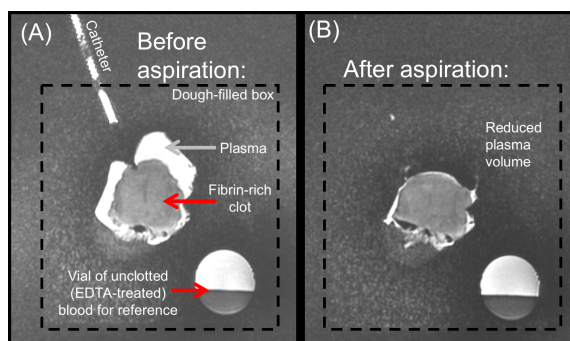
**Figure 4.1: Vision for MR-Guided ICH Evacuation.**

**A)** MR depicts bright plasma in T2-w image which can be extracted prior to clot lysing through aspiration. **B-D)** MR improves safety and cuts procedure time by displaying location of clot busting drugs relative to clot boundaries.

We hypothesize that T2-W imaging will clearly show plasma components which could be immediately aspirated under MR guidance to reduce intracranial pressure. We also hypothesize that co-infused Gd, or simply T2-W imaging, would differentiate the administered clot buster and lysed blood from rigid blood clots, as the lysing agent is distributed (illustrated in Fig. 4.1B), acts upon the clot (Fig. 4.1C), and is drained (Fig. 4.1D).

## Methods:

We mimicked ICH clots in vitro by drawing 50 mL of fresh blood from a swine donor, transferring the blood to a thin plastic bag, and burying it in soft dough to approximate the mechanics of surrounding brain tissue. By several hours after collection, the blood had separated into distinct volumes of free plasma and rigid clot, as shown in Fig. 4.2A.

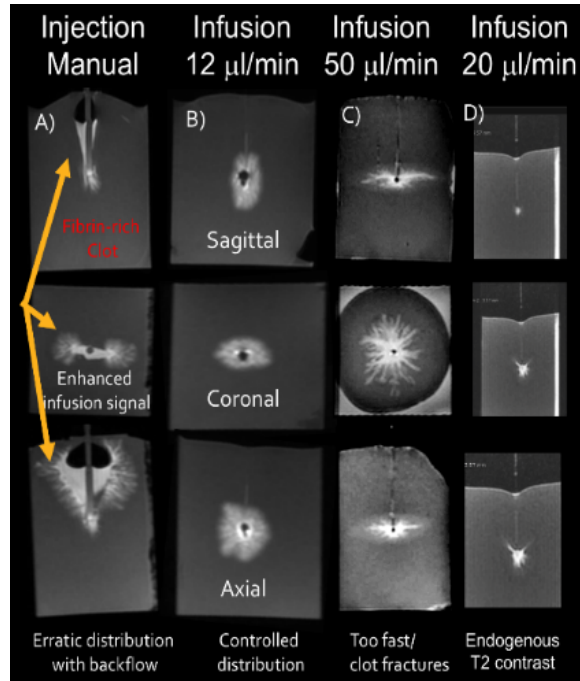


**Figure 4.2: In vitro feasibility study of plasma extraction.**

**A)** Bright plasma in T2-w image surrounds fibrin-rich dark clot. **B)** After plasma aspiration, volume of clot is significantly reduced.

We simulated plasma extraction by inserting a catheter into the plasma under MR guidance. We also operated on large solid clots that filled the  $55 \times 55 \times 75 \text{ mm}^3$  experimental boxes (Fig. 4.3) and were taken from multi-liter blood samples collected at a slaughterhouse during routine swine exsanguination. We simulated (1) manual surgical injection of rtPA clot buster into the clot with dose volumes (1–2 mL) and catheter diameter (3 mm) similar to techniques used clinically for MISTIE today, and (2) similar dose volumes delivered via pressurized infusions through a 0.7 mm fused silica catheter at flow rates of 12, 20, or  $50 \mu\text{L}/\text{min}$ , in accordance

with methods used for intraparenchymal brain cancer treatments. This infusion technique is known as convection-enhanced delivery (CED).



**Figure 4.3: Assorted TPA delivery methods.**

Simulation of surgical practice of manual injection (Col. A) shows highly asymmetric and dangerous clot buster distribution. MR guided infusion (Col. B-D) shows ability to monitor and control distribution. Note: no Gd contrast agent was used in the experiment of column D.

## Results:

The ability to aspirate plasma, thus decreasing clot volume and its deleterious mass effect on the brain, is shown in Fig. 4.2B. Manually injecting the clot buster, the actual surgical practice, creates escape routes along paths of least resistance, producing a highly asymmetric distribution with unwanted and potentially dangerous backflow along the catheter (Fig. 4.3A). Our initial experience using CED to infuse clots

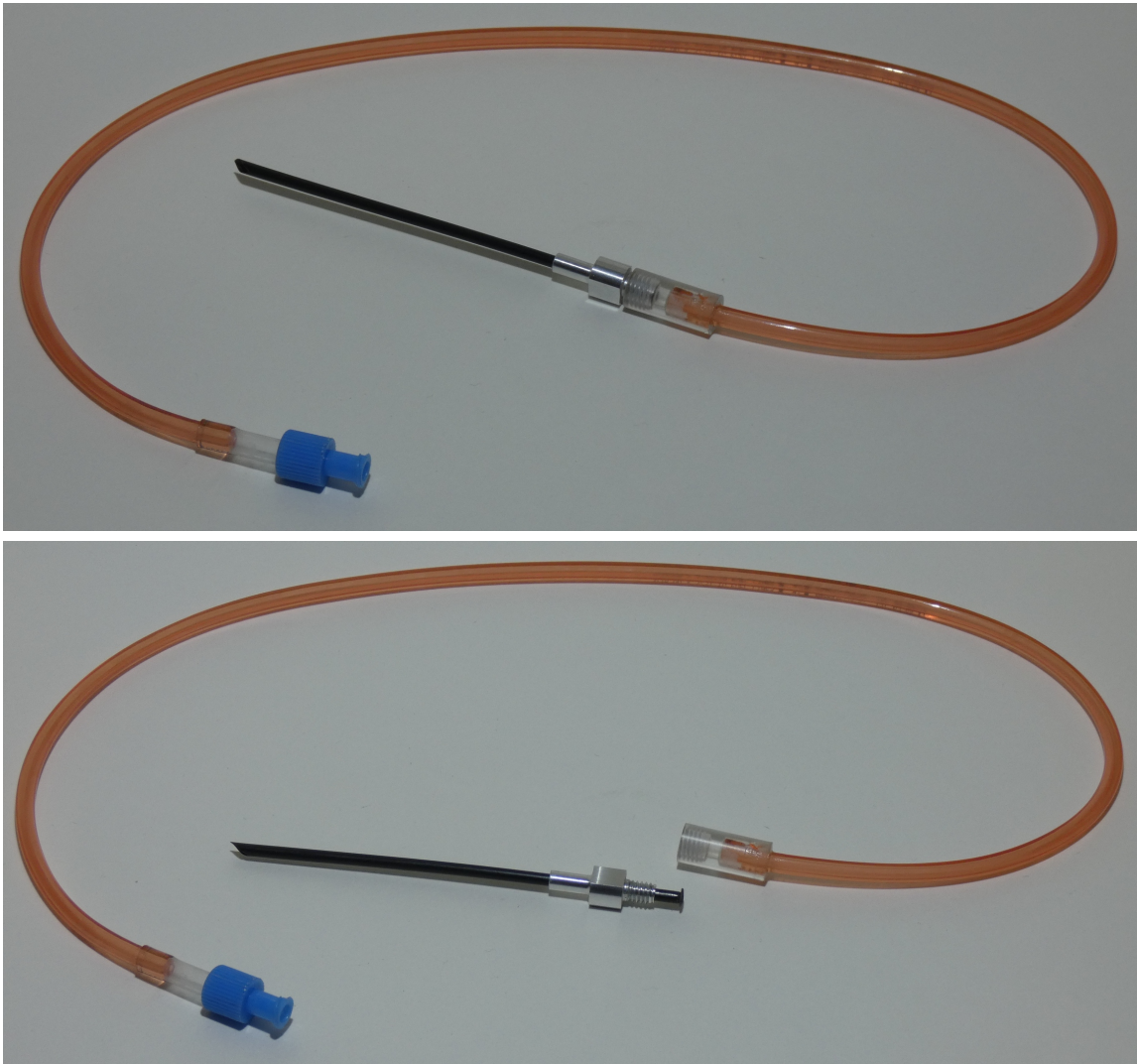
reveals a much more controlled and symmetric distribution of infusate (Fig. 4.3B) at 12  $\mu\text{L}/\text{min}$ . At the higher flow rate of 50  $\mu\text{L}/\text{min}$ , real-time monitoring shows the infusion fracturing the clot (Fig. 4.3C), which risks lysing at unsafe locations such as the exterior surface of the clot, where the failed vessel that was initially responsible for the hemorrhage is likely located. While Fig. 4.3A–C used co-infused Gd with T1 sequences, Fig. 4.3D demonstrates that T2 sequences without Gd show hyperintense infusion as well.

### **Conclusion:**

The ability of MR to visualize blood clot components and the spatial distribution of clot busting drugs within the clot holds significant promise for speeding the extraction of clots while visualizing whether the treatment is risking rebleeds by nearing the exterior of the clot.

## **4.3 Hardware fabricated for in vitro and swine in vivo experiments**

We developed an MR-compatible, configurable cannula platform for approximating the larger-diameter (3 mm) catheters used in ICH evacuation surgeries (Figures 4.4 and 4.5). The most delicate component, the cannula shaft, is easy to replace and very inexpensive.



**Figure 4.4: MR-compatible cannula with interchangeable tips.**

This MR-compatible cannula system has an aluminum body with small cylinder sized to fit into existing remote introducer hardware. It can be disassembled (**bottom**) to replace the black plastic cannula.



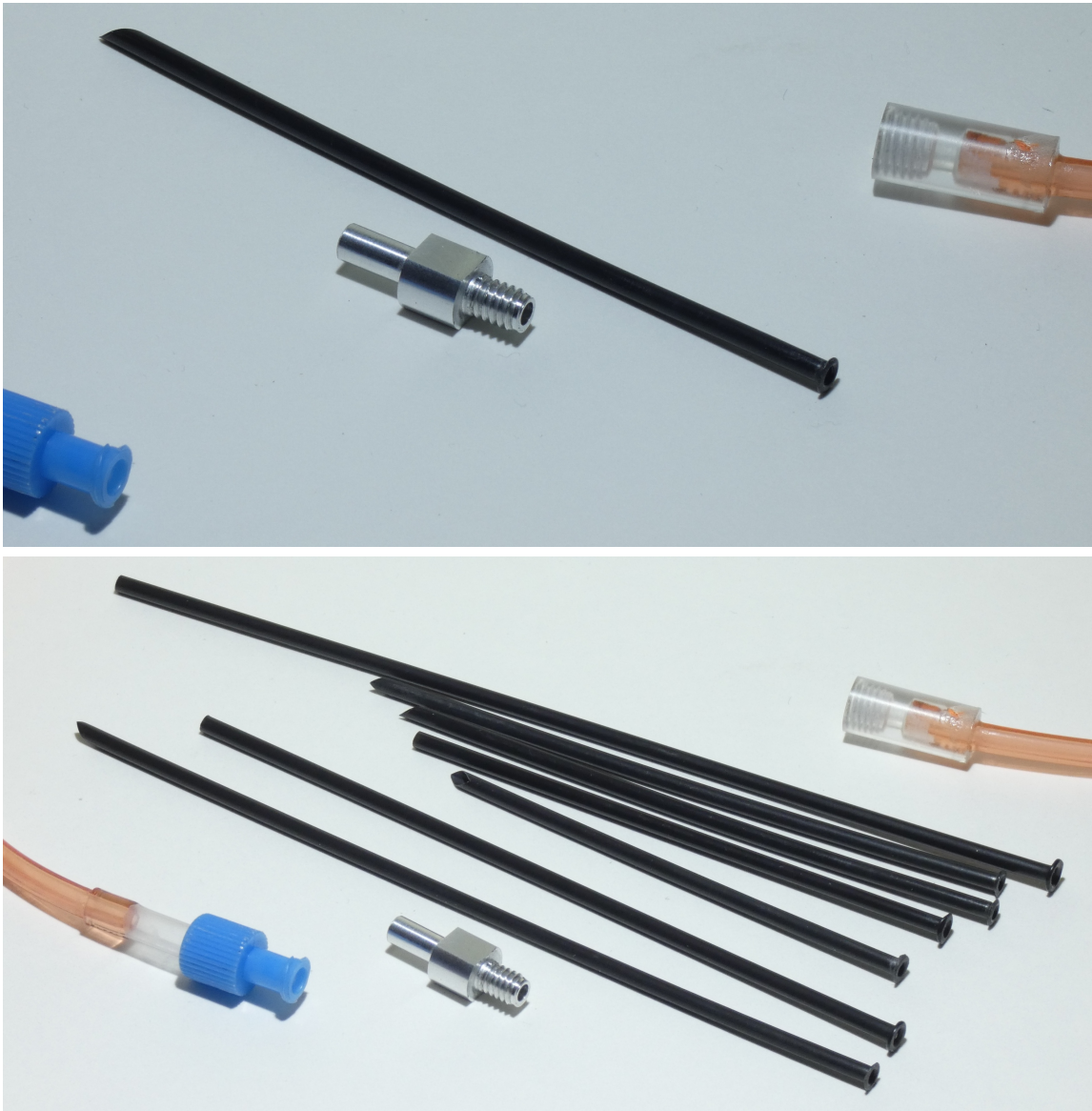
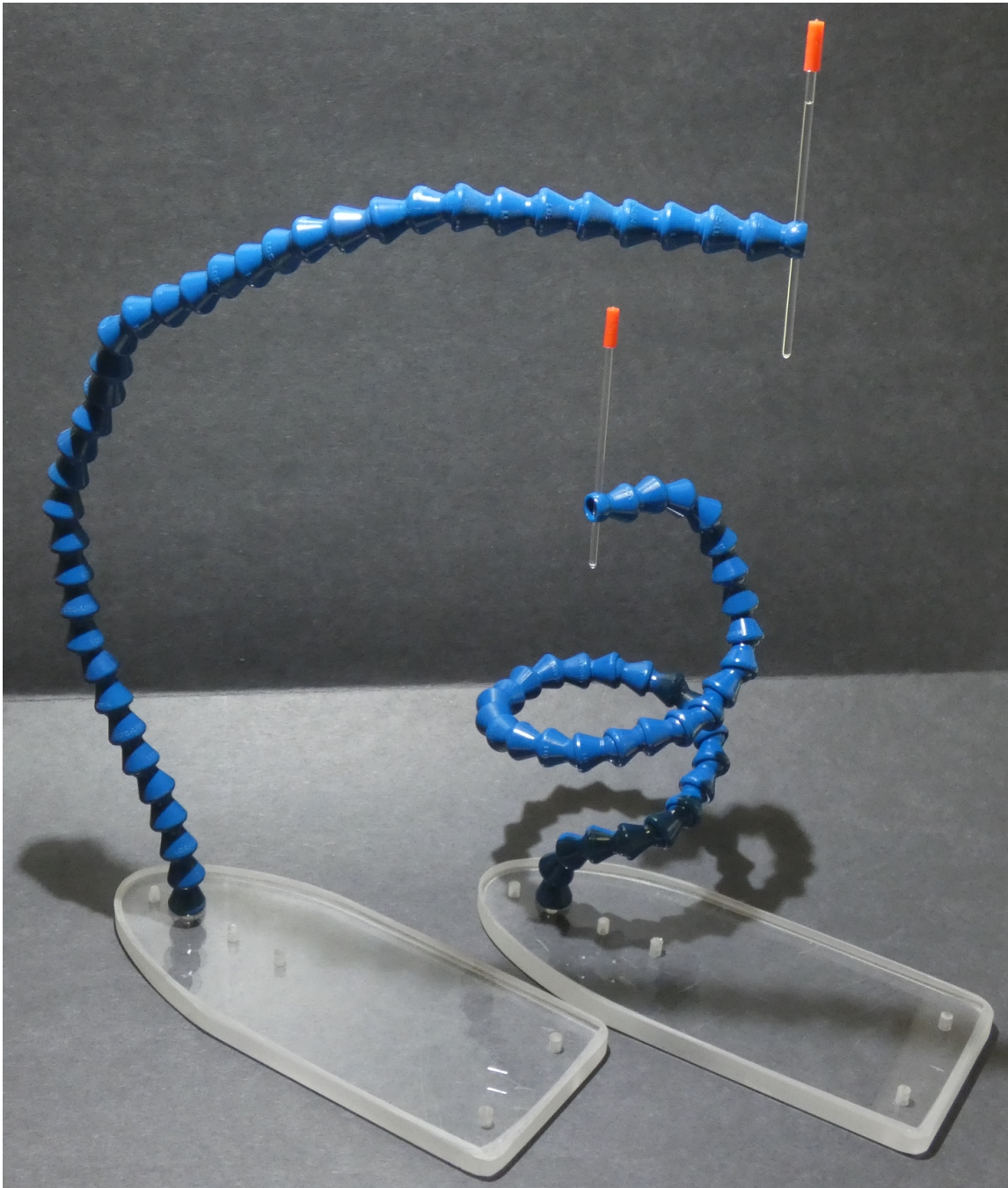


Figure 4.5: Closeup of MR-compatible cannula and tips.

The threads enable the aluminum piece to securely clamp the black plastic cannula and form a tight seal. (**bottom**) The device can be reconfigured with a continuum of different cannula lengths.

Previously, we had been determining burr hole locations at which to install

trajectory guides by taping vitamin E capsules onto the exposed surface of the swine skull, then acquiring an MRI volume and referencing off those fiducials. This proved difficult for multiple reasons: tape performs poorly in the wet surgical field, and the large size of vitamin E capsules introduces some uncertainty about where to measure from when using the capsule as a reference. We developed a pair of poseable arms that can be bent into arbitrary shapes and will maintain their configuration (Figure 4.6). The clear base is secured underneath the forelimb of the swine subject (in sphinx position), and the blue poseable arm can then reach up to hold an NMR tube with its tip on the exposed top of the skull.



**Figure 4.6: Poseable arms to hold fiducials during swine IMRI.**

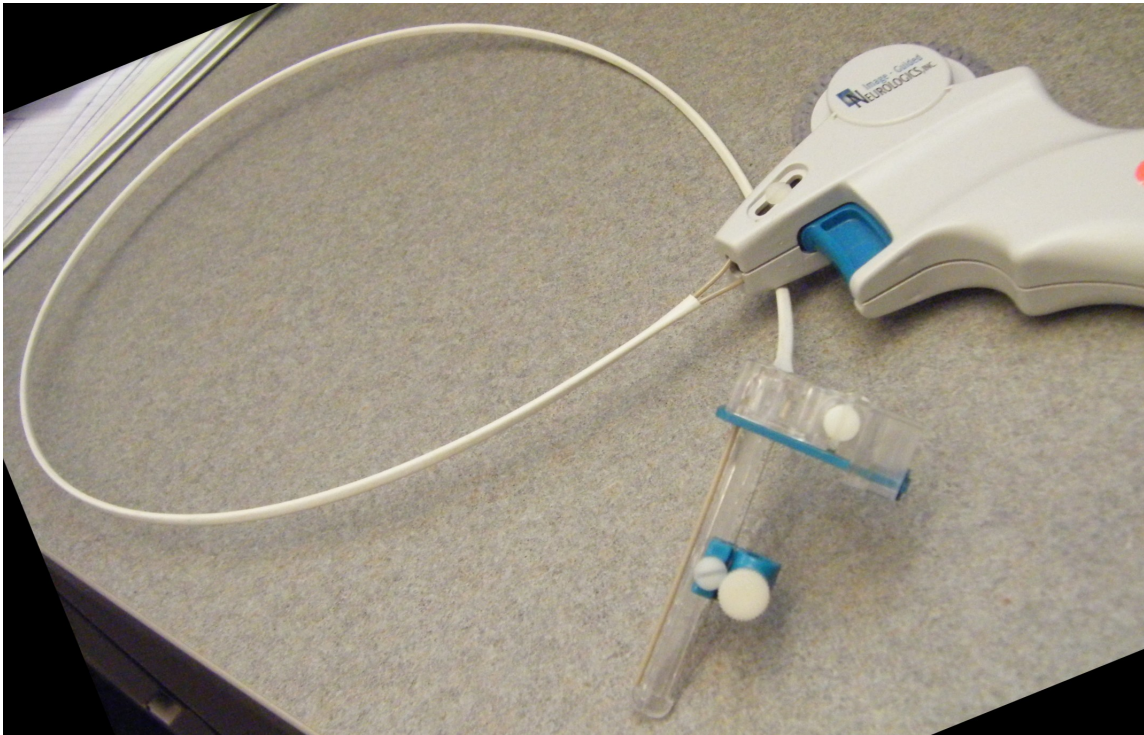
These poseable arms enable placement of NMR tubes containing MR-visible fluid on the exposed skull of swine during IMRI. This is far superior to our previous approach of attempting to tape vitamin E capsules onto the slippery tissue surface. Scale: NMR tubes are approximately 10 cm long.

Prior to the installation of trajectory guide bases, burr holes must be drilled in the skull. Our felt tipped surgical pens proved inadequate for making durable, high visibility marks in the surgical field to indicate the border of the planned burr hole. We developed a marking tool (Figure. 4.7) which can produce circular marks (shallow rings in the bone) that are precisely centered on a given point and which remain as a visible guide until the burr hole drilling is well underway. At that point, the burr hole itself is a suitable guide and a surface mark is no longer needed. The entire device is non-ferrous (all aluminum except for one small brass screw), to eliminate the risk of the tool being pulled into the magnet. The outer diameter of the sleeve is 10 mm, matching the size of burr holes for the orthogonal Navigus trajectory guides used in our swine IMRI studies.



**Figure 4.7: Tool for marking burr hole perimeter on swine skull.**  
This marking tool consists of a pointed shaft with a captive sleeve that can slide along and turn about the shaft, all attached to a handle for easy manipulation.

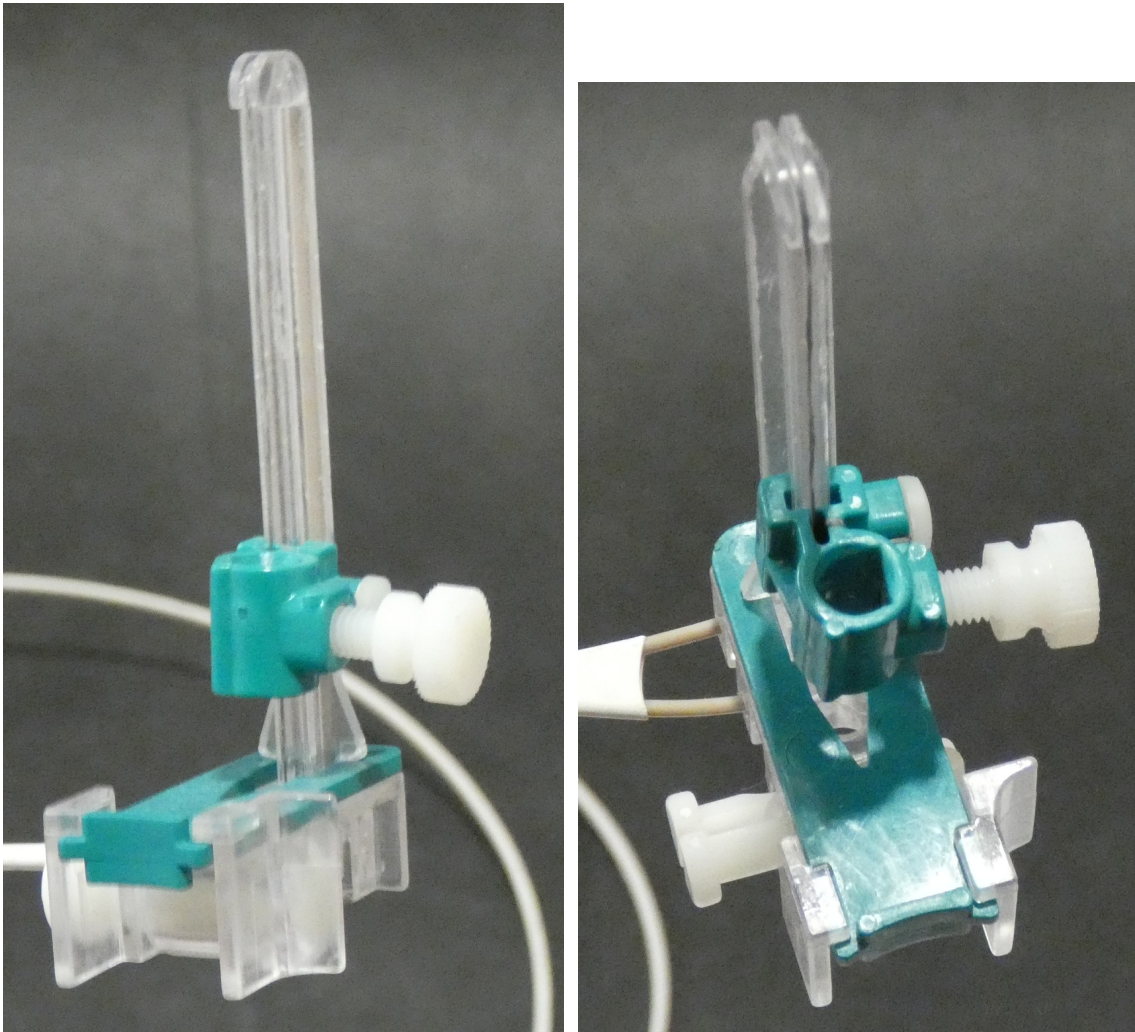
After a Navigus trajectory guide is aimed, the alignment stem is removed and a small linear stage called the “remote introducer” (RI) is attached in its place. The moving portion of the RI is pulled down or up (to advance or retract a cannula) via cables which go to a hand held remote (Figure 4.8).



**Figure 4.8: Remote introducer.**

Linear stage, control cables, and hand held remote. Blue trigger on hand grip locks stage from moving.

Our CED cannulas are made to slide partway through the piece that moves up and down. They are then secured by a set screw (Fig. 4.9).



**Figure 4.9: Linear stage.** Oblique views from the side and top of the linear stage. White set screw attaches cannula to teal piece which moves up and down.

Because the RI hardware is long out of production, quantities are limited. In order to perform simultaneous infusions in swine while only possessing one RI, we designed and fabricated introducer hardware that would allow us to place two cannulas in the brain simultaneously (Figs. 4.10 and 4.11).

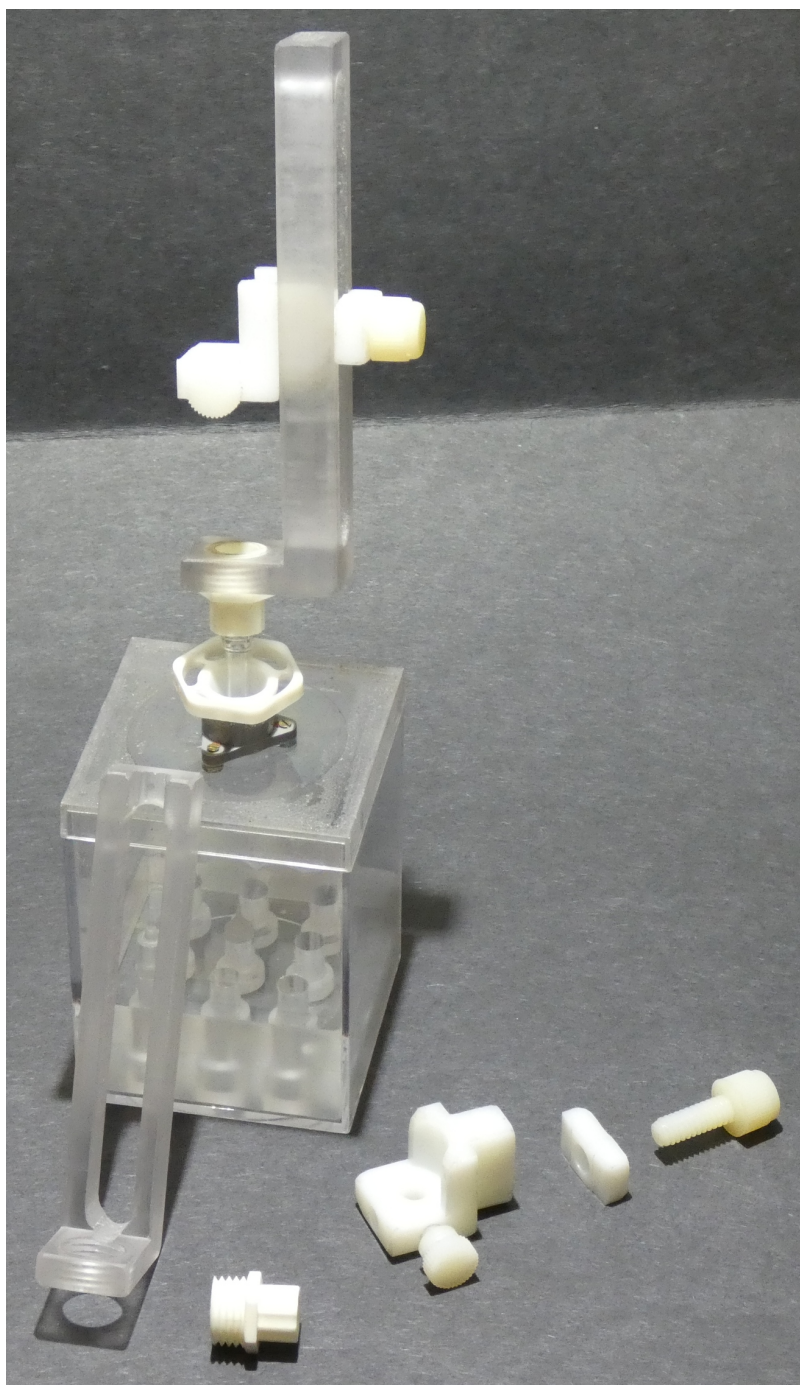


Figure 4.10: **New introducer hardware.** (**Top**) assembled and mounted to the guide tube of a Navigus trajectory guide. (**Bottom**) disassembled to show components.





**Figure 4.11: New introducer hardware (close up).**

The larger set screw is used to lock the stage from traveling up and down. The smaller set screw holds a cannula in place, as in the original RI hardware. The threaded Luer adapter (white, lower left) enables these introducers to thread onto the guide tube of the Navigus.

## 5 CONCLUSIONS AND RECOMMENDATIONS FOR FUTURE WORK

---

*We can only see a short distance ahead,  
but we can see plenty there that needs to be done.*

— ALAN TURING

I have now described my developments in preoperative planning for DBS, my methods for preoperative planning and intraoperative tracking used in preclinical gene and cell delivery studies, and my work to develop an in vitro model of ICH suitable for mock surgery and further exploration of possible MRI monitoring during clot evacuation. In this final chapter, I will present the conclusions and recommendations for future work.

### 5.1 Aim 1: preoperative angiography for planning

We observe that bSSFP is better than TOF at depicting small vessels in the basal ganglia.

We found a modest prevalence (12%) of EPVS in or immediately adjacent to the putamen among subjects around the age of Parkinson's disease onset. For future studies, we feel that a more-automated approach using computer vision would be preferable to the approach used here, which relied on human readers. The WRAP project already possesses versions of the MRI volumes that have been coregistered to an anatomical template space. This would allow an ROI to be segmented once in the template space, then easily inverse transformed back to each individual's

MRI scan space to set the EPVS search volume more consistently from subject to subject. WRAP scans also include small vials of water within the FOV when subjects are scanned, so an intensity threshold for vessel segmentation could be based on the reference signal from free water, making the process a little more quantitative despite variation in scanner performance (across, and even within, scan sessions).

We observed a modest rate (18%) of trajectory adjustment when the surgeon planning a DBS trajectory into GPi was unblinded to a bSSFP image volume containing the putamen. As a next step, we suggest a small study in the actual population of patients seeking DBS electrode implantation. The bSSFP sequence could be added to the standard preoperative protocol used in the clinic, and the same procedure of blinded planning followed by unblinding and optional trajectory adjustment would be used to determine whether the bSSFP imagery has a similar influence on planned trajectories in the patient population as well.

## **5.2 Aim 2: intraoperative trajectory guide tracking**

Preoperative planning in 3D Slicer is feasible, but laborious. We're harnessing default functionality of the software to perform this planning task. It could be easier with a Slicer plugin that is purpose-built to assist with:

- Keeping the base bottom surface tangent to outer table of skull
- Adjusting start and end locations of ruler lines so they always go from pivot to target
- Exhaustively searching for base locations/orientations to optimize placement

In the case of the latter, the surgeon's precision when placing the bases in the OR is approximately 1~2mm, and for setting the angle it may be as much as 5°. An exhaustive search could try coordinates within a 50 mm by 50 mm square in the axial plane, centered on the skull, for a total of

$$(50 \text{ mm}/(1 \sim 2\text{mm})) * (50 \text{ mm}/(1 \sim 2\text{mm})) * (360^\circ/(1 \sim 5^\circ))$$

$$= 900\,000 \sim 45\,000 \text{ possible ways to place base}$$

Real-time MR computational device tracking is useful and has performed well in 80+ experiments to date (71 survival NHPs, 7 swine, 2 NHP pilots for causal fMRI). Further simulation, using measurements of observed noise, is warranted to optimize the number of projections per stem-plane computation, and the number of distinct trajectory guide orientations sampled per pivot computation.

Perhaps it is incorrect to describe this technique as "computation instead of imaging". A one-dimensional image is reconstructed from each MR readout for the peak finder to consume. From this perspective, one could view the progression of the field in this way:

- ClearPoint SmartFrame - 3D imaging
- GantryMate - 2D imaging, 2 planes
- Our method - 1D imaging, ~20 lines \* 2 planes

to continue the trend to lower dimensionality and less data sampling would seem to require "zero-dimensional imaging". Thus, it looks like 1D imaging, with 2~4

readout lines \* 2 planes is about the minimum amount of data one could sample and still produce a useful result.

This method, preoperative planning and intraoperative guidance, has enabled our collaborators to perform surgeries that they would otherwise have been unable to do. Classic animal neurosurgery approaches, using only stereotaxic coordinates and no intraoperative imaging, would frequently miss the small targets due to individual variation of subjects, which causes disagreement between the anatomical targets and the atlas-derived stereotaxic coordinates. Many subjects would have to be rejected from the study after post mortem histology revealed that the surgery missed its mark. To achieve the same number of successful surgeries with those methods would necessitate an enormous number of unsuccessful surgeries, which would be ethically unacceptable and extremely costly. By doing our best to ensure that each surgery will work as planned, we are minimizing the number of animal subjects used in these projects.

Maintaining the IMRI software stack across multiple upgrades of the GE scanner software, Real-time computer host OS, and RTHawk is time-consuming. It would be worthwhile to simplify the software, which may be reducible to just a few RTHawk plugins (compared to the current incarnation of the software: Vurtigo + geometry server + RTHawk plugins).

With this new computational aiming method, it feels like much of our IMRI time is now taken up by the 6-minute IR FSPGR  $T_1$ -weighted BRAVO scans that we acquire several times per needle insertion. Further speedup of the procedure will likely require the development of a rapid 2D sequence with near fully-sampled

acquisition that is able to produce a 2D image with resolution and contrast similar to the BRAVO scan. Such a sequence could then be used to quickly check: aim confirmation, partial depth insertion, full depth insertion, and possibly infusion monitoring (though the 3D coverage of the BRAVO scan is nice to have, and infusions are typically longer than 6 minutes, so the BRAVO usually fits into the infusion timeline without issue).

### **5.3 Aim 3: model of intracerebral hemorrhage**

The first major difficulty was finding a source of blood. In the absence of a high-availability source, it was difficult to explore some of the secondary research questions:

- use of magnetization transfer imaging
- use of MR elastography
- development of an in-vitro model of ICH
- use of conventional ultrasound imaging on in vitro model

The blood source problem was mostly solved by a collaboration with the Meat Science department, and I am very grateful to Jen Meudt and Robby Weyker for their assistance. There are still difficulties with synchronizing blood and scanner availability. Repeated scanning for 48+ hours is best done over the weekend starting Friday evening, and swine exsanguination is only performed on weekdays, not always on Fridays. For future work, it may be worthwhile to immediately treat the

collected blood with anticoagulant (e.g., EDTA), then later introduce a coagulant (e.g.  $\text{Ca}^+$  ions) when the MRI scanner is available. Further testing is warranted to determine the differences, if any, between untreated freshly clotted blood and blood which has had its clotting delayed in this way. If the delayed clotting does not significantly change the properties of the blood, this would be a welcome modification of the model.

A workable in-vitro model was eventually developed, but with some compromises. It proved difficult to develop a phantom that would mimic the brain as needed. The model of a large clot snugly contained in a small box is compatible with our approach to IMRI accuracy testing in phantoms, allowing reuse of trajectory guides and IMRI aiming technique.

The failure of the MISTIE stage III clinical trial is unfortunate: “For moderate to large intracerebral haemorrhage, MISTIE did not improve the proportion of patients who achieved a good response 365 days after intracerebral haemorrhage” [58]. But perhaps this opens a window to argue in favor of trying again with MRI guidance/monitoring, and a more aggressive dosing strategy instead of MISTIE’s CT guidance/monitoring, and conservative dosing strategy.

In this aim we did not perform several trials of any one experiment, but we did trials of several different experiments to explore the space and look for interesting avenues to pursue. With the logistical problems now partly solved, further research is warranted on topics like:

- Infusion rather than injection
- Different catheter designs

- Different flow rates
- Various sequences for assessing clot structure:
  - Mag. transfer - seems promising
  - $T_2w$  - seems promising
  - DWI - questionable due to image warp from susceptibility variation
  - MR elastography - may be okay in vitro, questionable in vivo due to acoustic driver jostling brain and risking a rebleed



## A APPENDICES

## A.1 Surgical map and symbols

Subject ID: [r/cy] \_\_\_\_\_  
 Date: YYYY-MM-DD

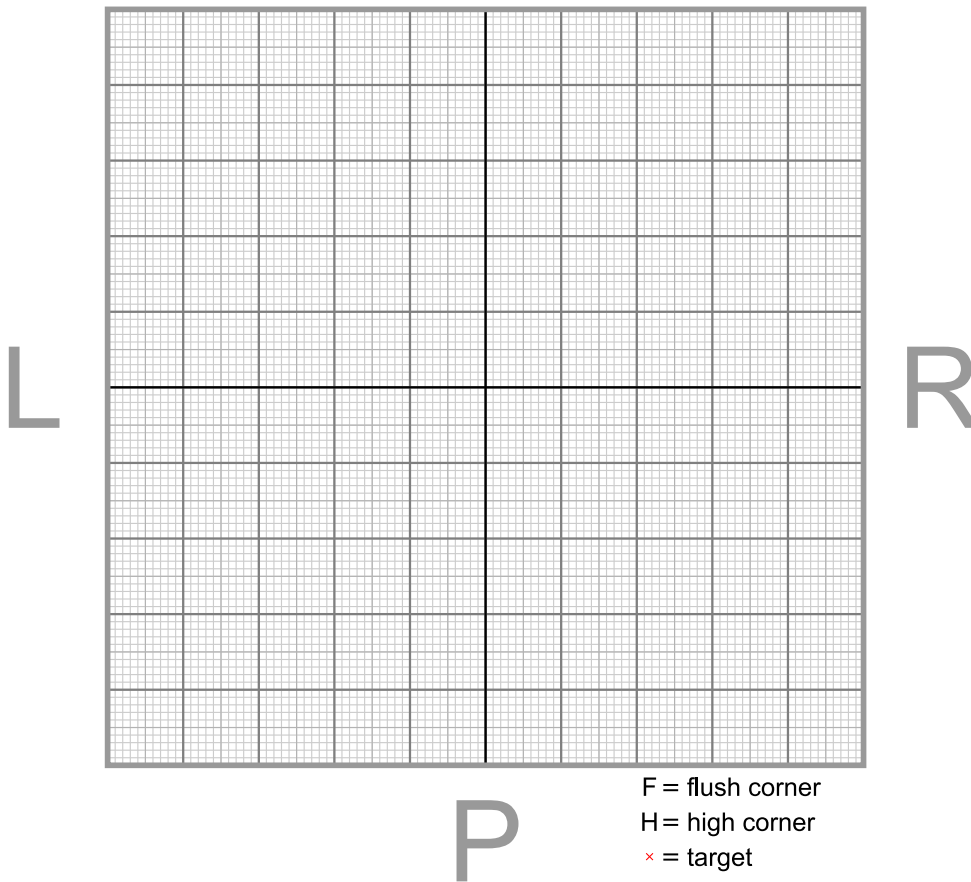
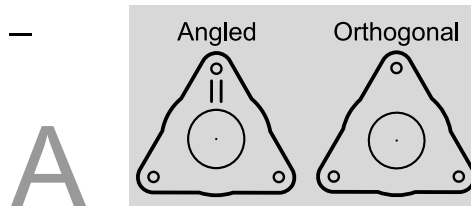
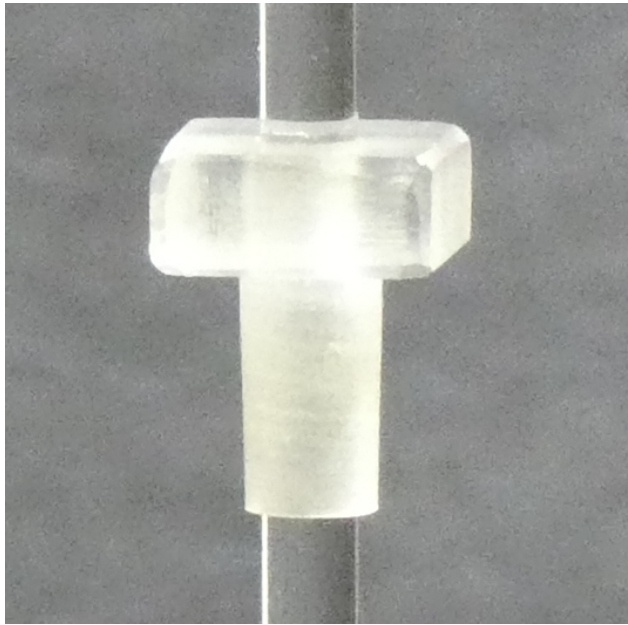


Figure A.1: **Blank surgical map template.**  
 The smallest divisions on the grid are 1 mm.

## A.2 Machining conical adapters

Described below is the approach to making NMR tube adapter cones with material and tools from the Medical Physics machine shop.

### Finished adapter



**Figure A.2: A finished conical adapter on an NMR tube.**

Bare (left) and inside Navigus guide tube (right). The bore of the adapter is nominally 3 mm, finished to achieve a sliding fit around the NMR tubes, which have a nominal outer diameter of 3 mm. The taper of the conical section matches the corresponding Luer taper on the ball joint tube of the Navigus trajectory guide. The head has been squared off so the adapter is easy to grab and remove from the Navigus, and to prevent it from rolling when set down on a flat surface.

## Materials

The Clausing lathe has a quick-release tool holder on the top slide and a taper inside the tailstock which permit rapid tool changes. Be aware that the scales on the handwheels are in thousandths of inches. Time can be saved by gathering the necessary tools and preparing multiple chucks with the appropriate bits, rather than placing and removing bits several times with a single chuck.

For stock, use a dowel of cast—not extruded—acrylic (PMMA). Start with a diameter that is thick enough ( $5/8$  in is a common size that works well) to give the part some rigidity during the drilling operations, before it is turned down to a small diameter and tapered. Delrin (POM) may be a good alternative to avoid downsides of PMMA, such as crazing from alcohol exposure.

Cut about 8 cm off the dowel stock to obtain a workable length. Multiple adapters can be made from a piece this long. Hold the work piece with a collet, rather than the 3-jaw chuck, for greater precision.



Figure A.3: Suggested materials for machining adapters.

## Procedure

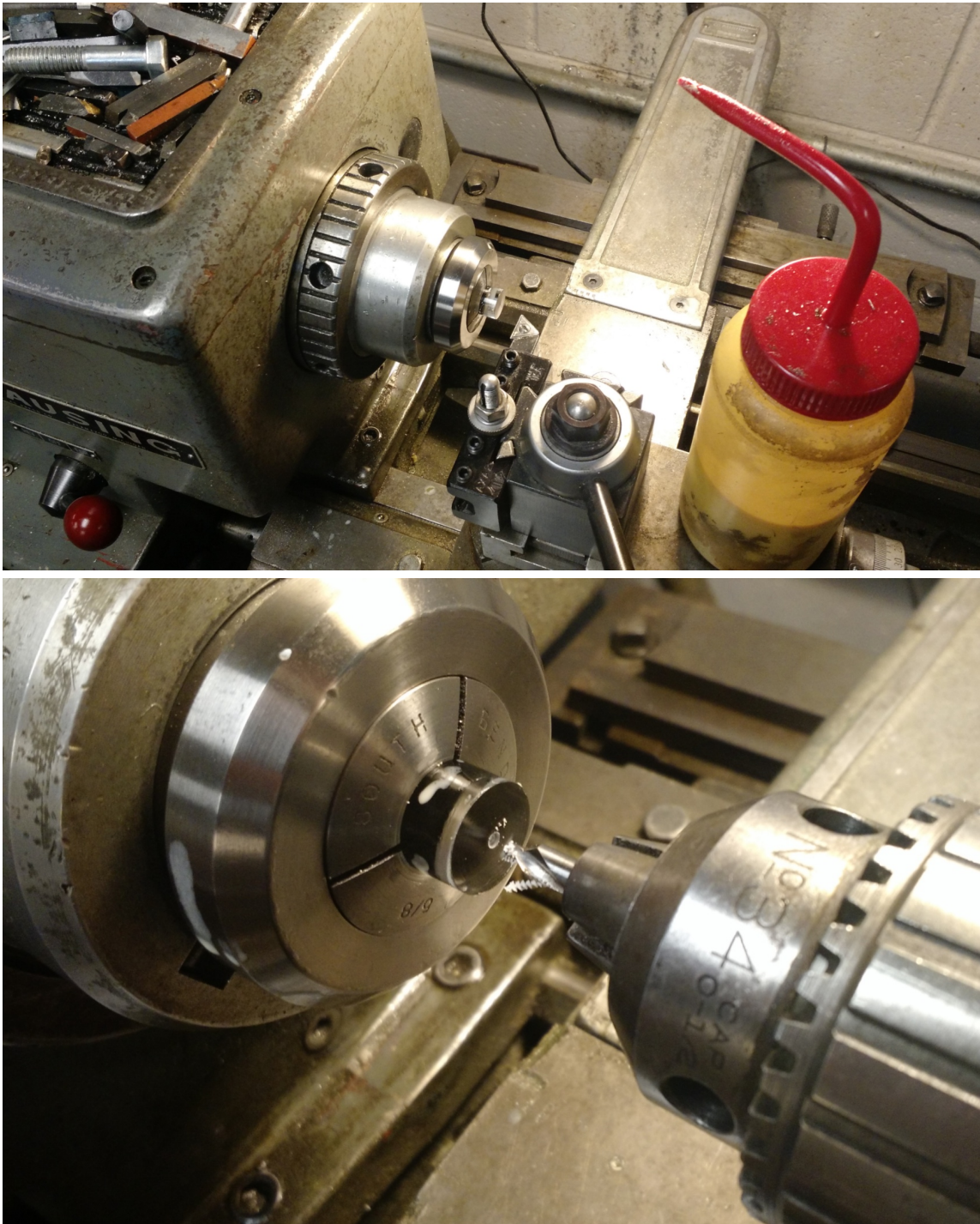
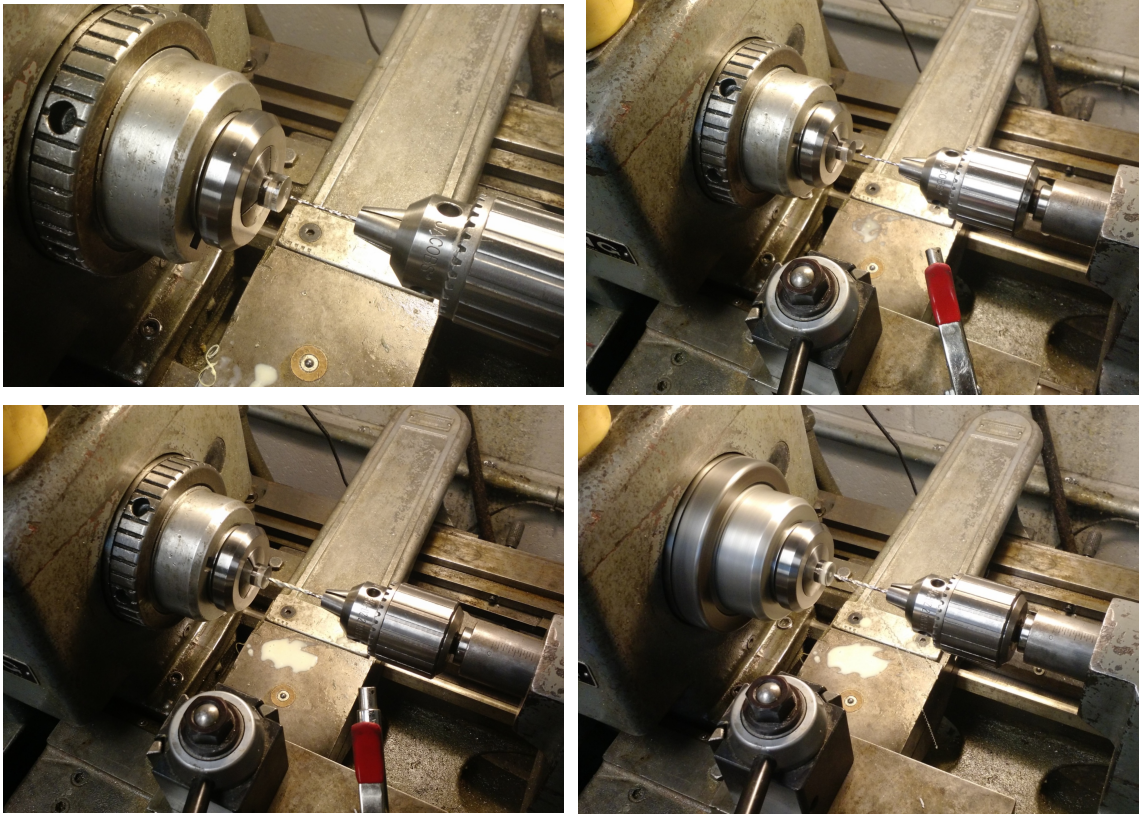
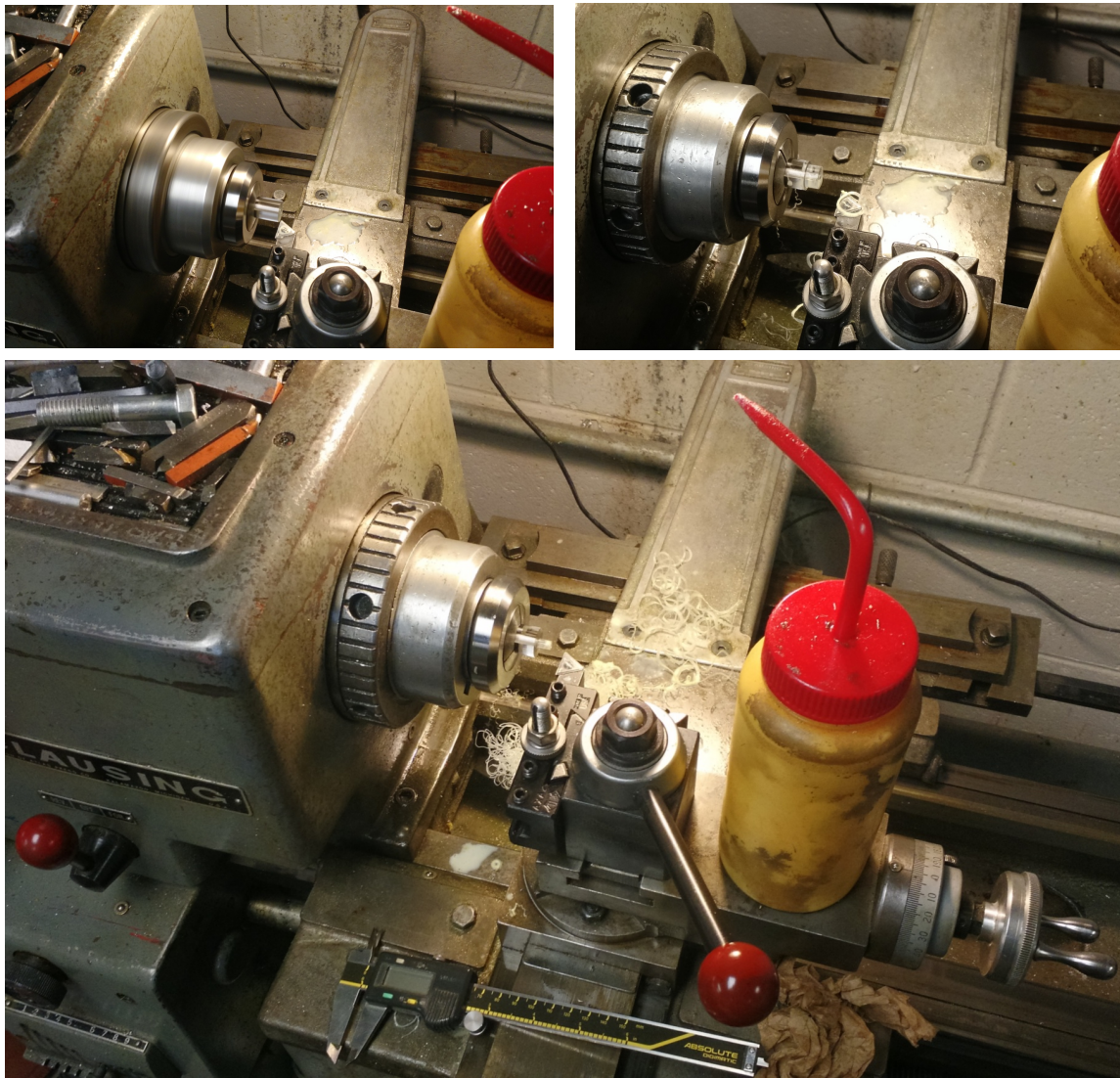


Figure A.4: Face off end of stock, then center drill.

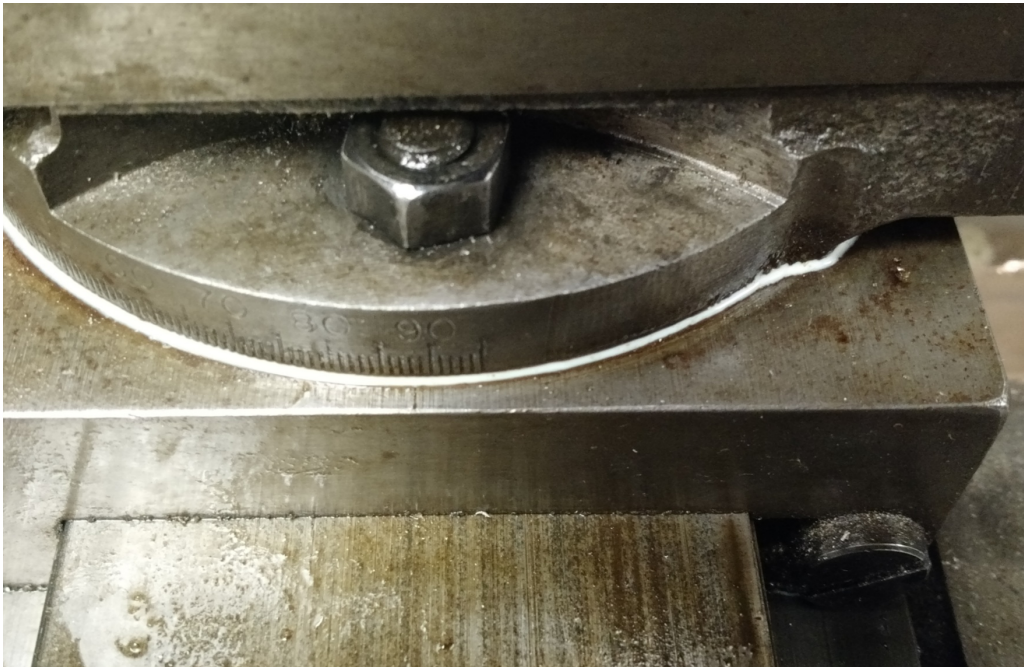


**Figure A.5: Drill with #45 bit, then #32.**

Apply cutting fluid and peck hole gradually using handwheel on tailstock to advance and retract bit. Use compressed air to clear chips and cool the drill bit and workpiece to prevent melting.



**Figure A.6: Reduce outer diameter.**  
Over a length of approximately 0.5 in, turn down cylinder until outer diameter is approximately 0.2 in.



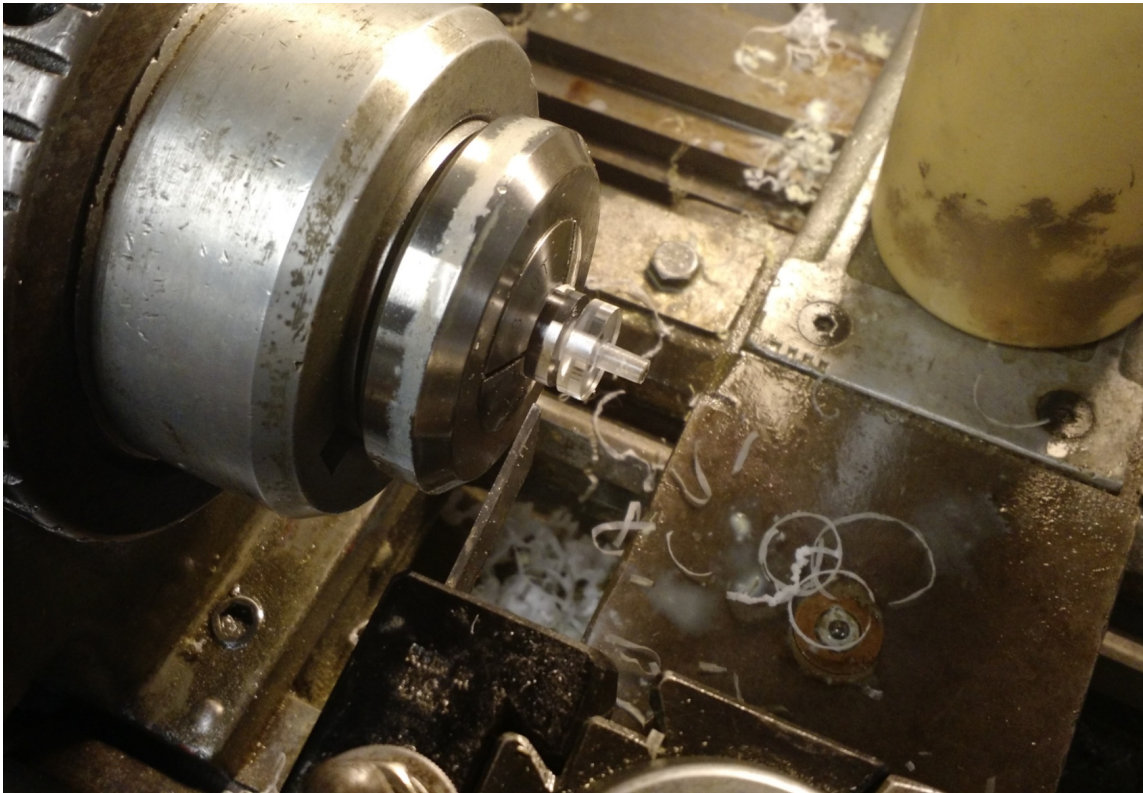
**Figure A.7: Set angle of top slide to achieve desired taper.**

Loosen nuts that hold top slide, rotate to just a little over  $1.5^\circ$  off  $90^\circ$ , retighten nuts.

Continue turning down reduced section until outer diameter at the tip measures approximately 0.150 in, performing test fits as described next.

With lathe spindle stopped, press the guide tube of one of the Navigus trajectory guides onto the cone to test the fit. If the cone reaches the bottom of the Luer tapered cavity on the Navigus guide tube before engaging with the sides, it is too narrow and some length should be faced off the tip to expose a wider tip. If the tip of the cone is wide enough to touch the sides before bottoming out, but the wider cone surface toward the collet is not touching the inside taper of the Navigus, the taper must be made less pointy (top slide angle must be adjusted farther from  $90^\circ$ ). If the tip of the cone fits into the Navigus but the cone surface higher up jams on the mouth of the Navigus and cannot be inserted further, the taper must be made more pointy (top slide angle must be adjusted closer to  $90^\circ$ ).

After the desired conical taper is achieved (see right side of Fig. A.2), face the exposed side of the cylinder from the outer edge of the stock to the base of the cone with a light depth of cut ( $\sim 0.010$  in) to clean up that surface.



**Figure A.8: Cut off with parting tool.**

Reset the top slide angle to  $90^\circ$ , swap insert cutter for parting tool, and advance cross slide to cut off part, leaving a disk about 0.15 in tall above cone.



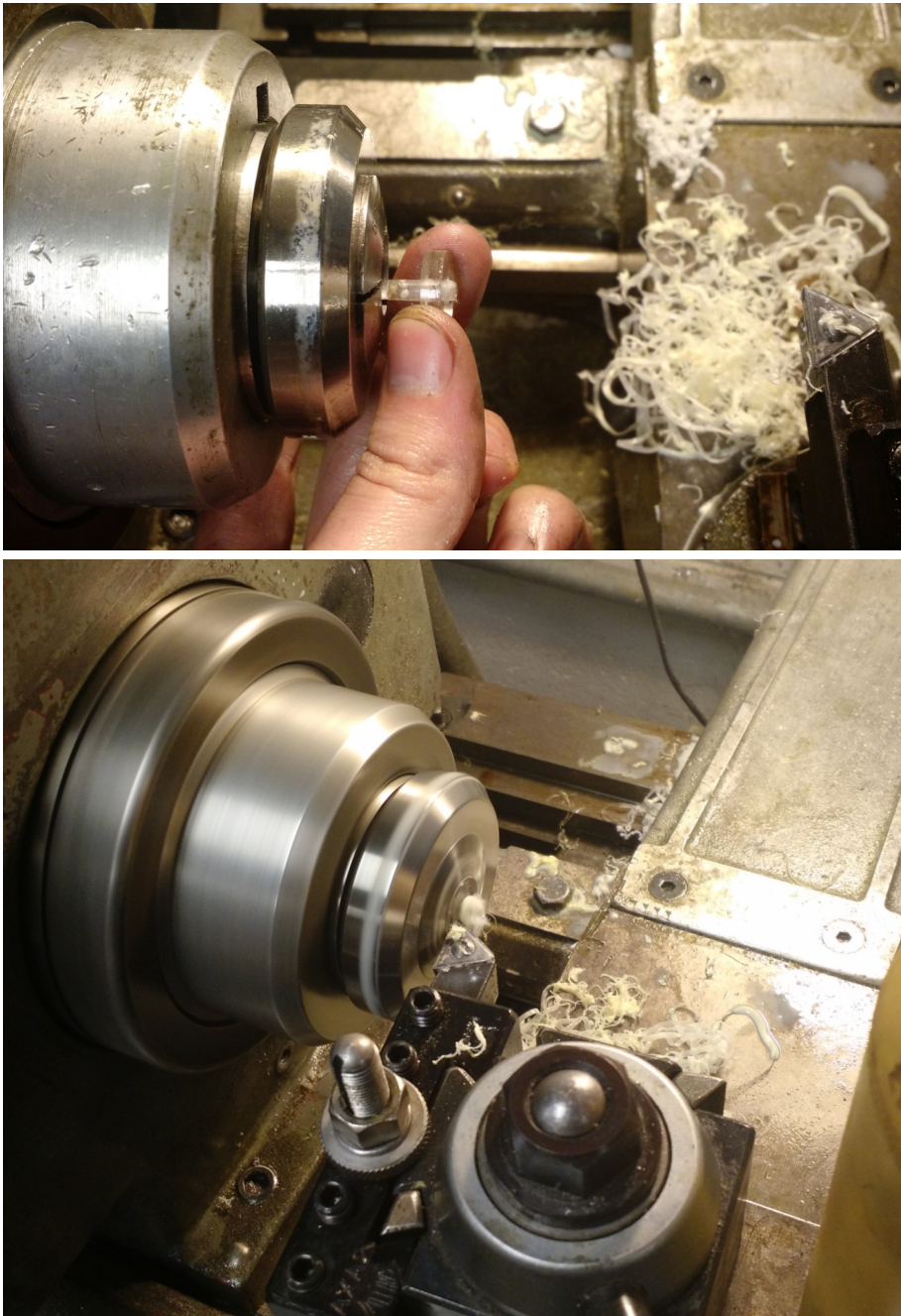
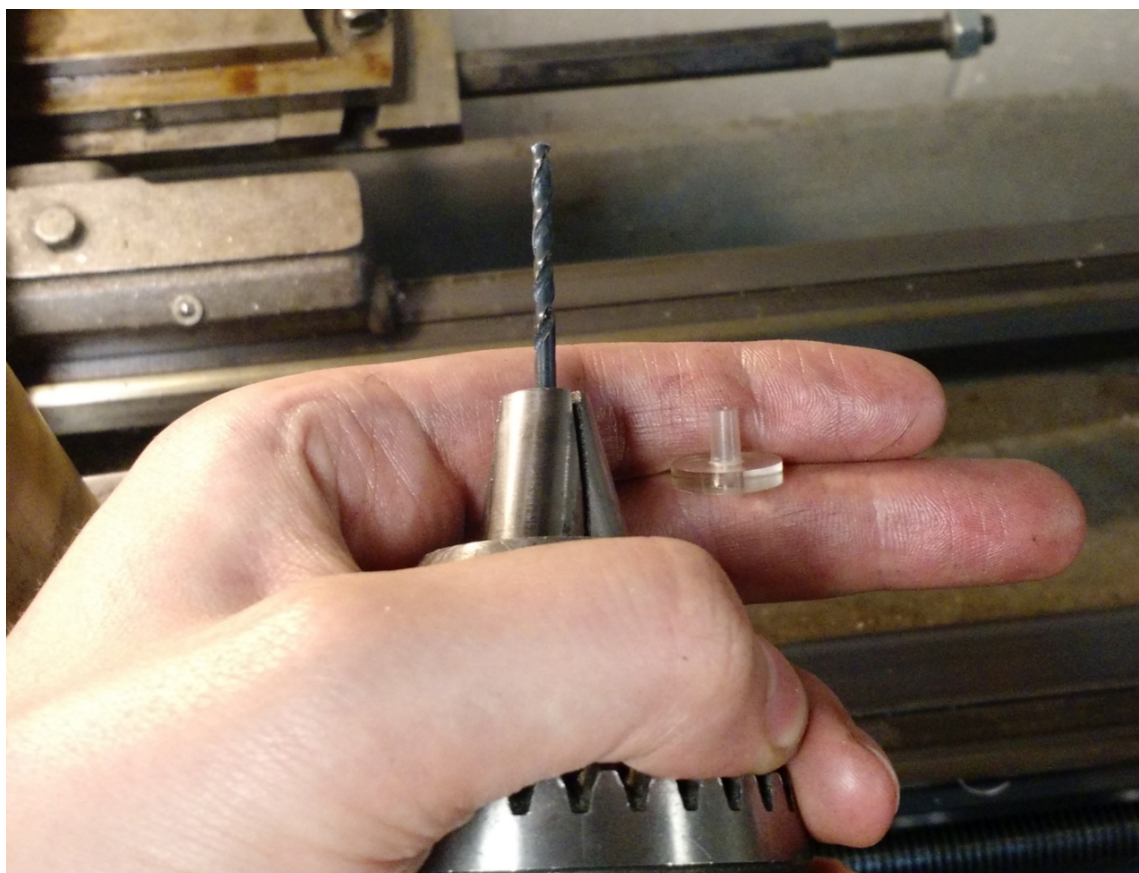


Figure A.9: **Reverse part in collet, face off.**  
Swap back to cutting tool before facing off excess material from parting operation.



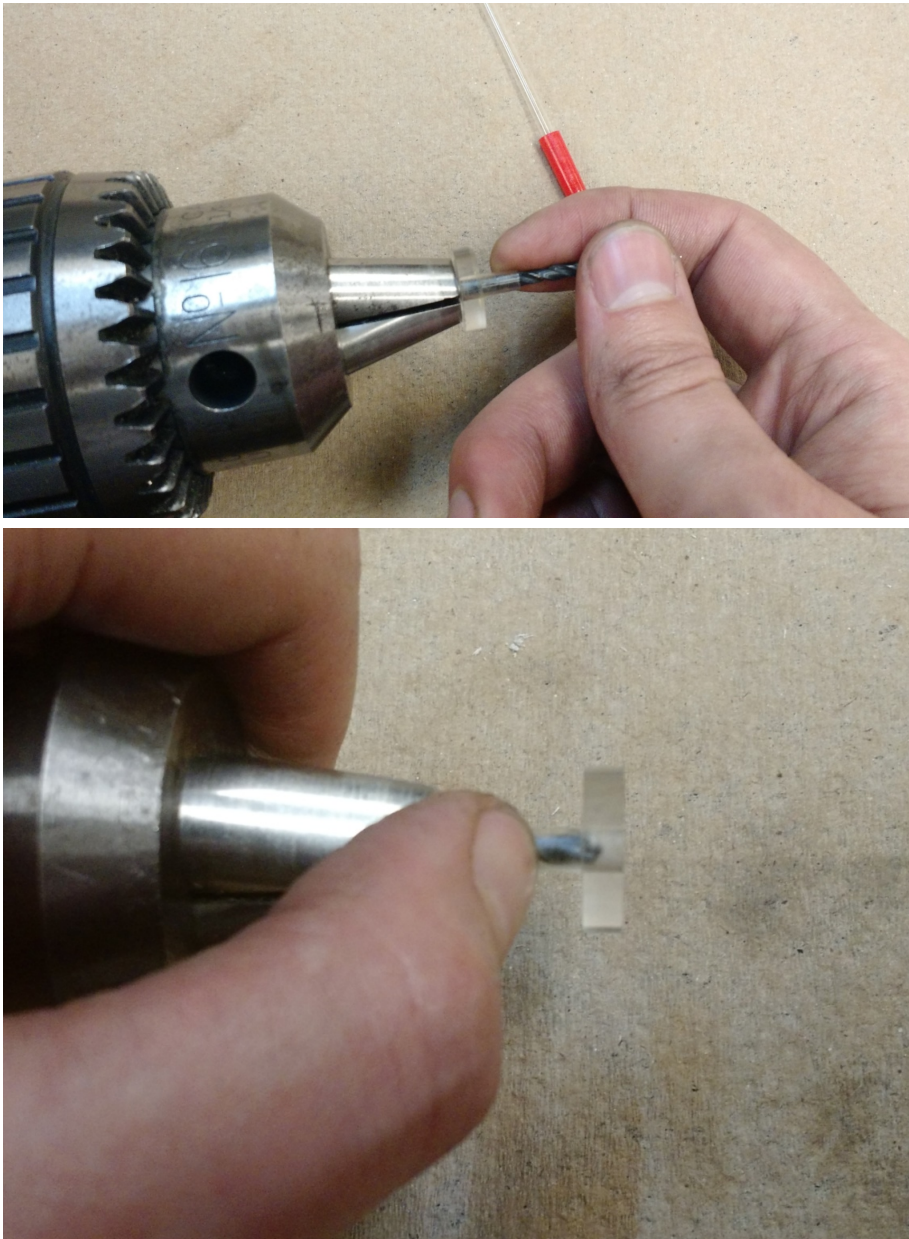
**Figure A.10: Remove from collet, finish drilling by hand.**

Using the 3 mm drill bit in the lathe will produce a hole that is slightly too loose to get the desired fit on the NMR tubes. Carefully spin the part around on the bit by hand to bring the hole up to size.



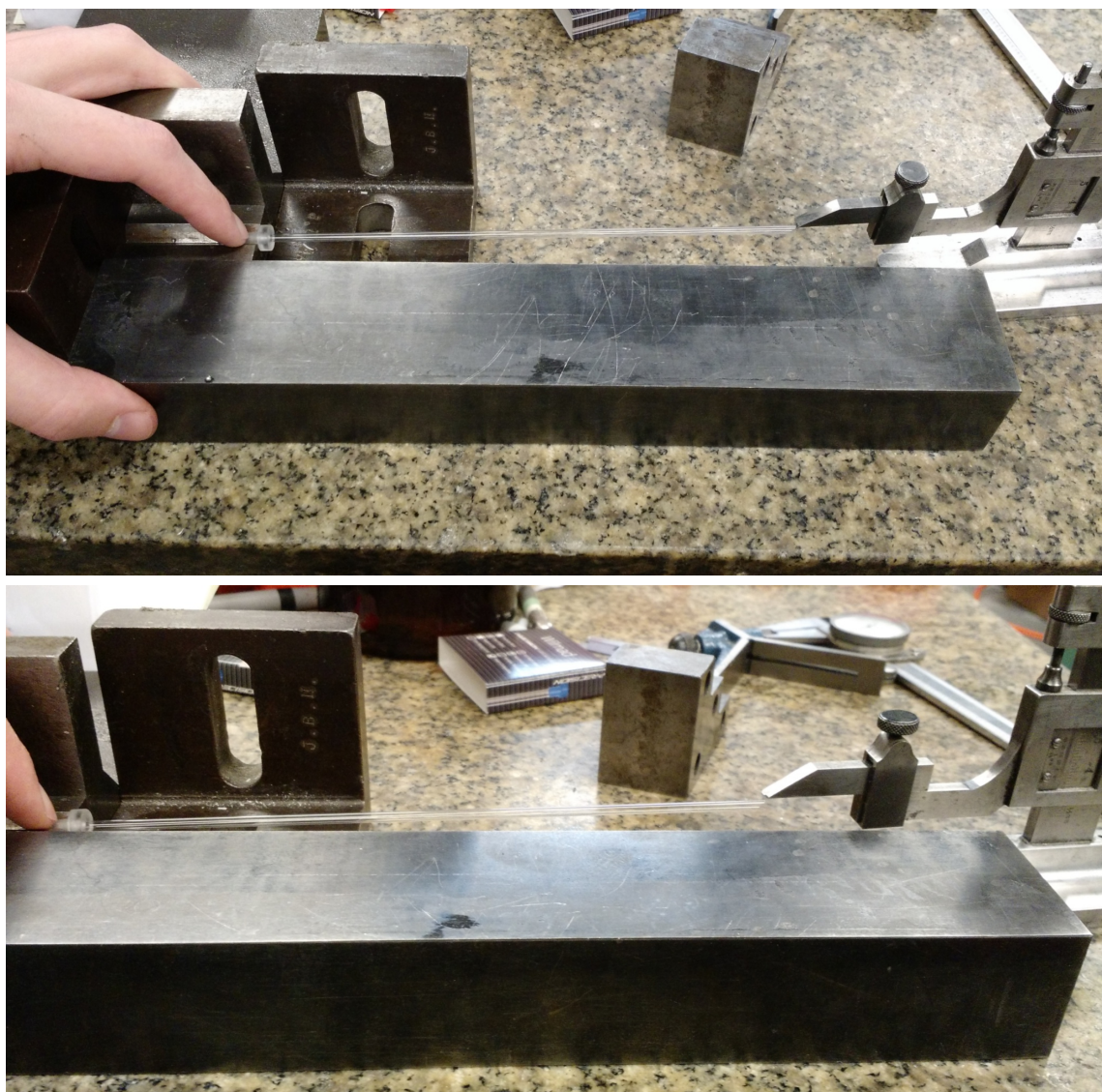
Figure A.11: **Test fit with NMR tube.**

Try inserting NMR tube to find any tight spots along the length of the bore where tube binds and cannot be pushed further. In the case shown here, the tight spot is near the tip of the cone.



**Figure A.12: Apply radial pressure at level of binding spots.**

The flutes of the drill bit are not sharp like the tip, but they can gradually remove plastic in this way. Depending on where the tight spot is, applying pressure may be easier if the part is flipped around (lower image). Press down with a fingernail and spin the part with the other hand.



**Figure A.13: Test concentricity error.**

A measure of concentricity error can be made by placing a long uncut NMR tube in the adapter so the bottom of the tube is not far past the tip of the cone. Hold down the cone with a fingernail so the entire length of its taper is resting in the V of a V-block (ensuring that NMR tube is not poking out far enough past cone tip to touch the V-block). Rotate the adapter and use a height gauge to measure the magnitude of displacement at the far end of the NMR tube over a full rotation of the adapter.

### Squaring off round head

The procedure for using a milling machine to square off the round head of the adapter was not photographed, but it is described below:

1. Install a collet and flat bottomed end mill in the spindle. Mill bit diameter should be somewhat greater than the thickness of the plastic cylinder on the part (which should be about 3–4 mm), so the whole thickness can be cut in one pass.
2. Clamp part in vise so the flat ends of the cylinder are held by the inside of the vise jaws and the tapered cone is completely above the jaws.
3. Turn small handwheel to move saddle along Y axis (toward-away) until end mill is centered over cylinder. No need to adjust Y axis again after this, so turn small handle to lock Y axis.
4. Turn small handwheel to move table along X axis (left-right) until end mill is centered over the highest point on the cylinder.
5. Unlock and lower quill until bottom of end mill just touches highest point on cylinder.
6. Lock quill travel.
7. **Note Z axis position** (height of the mill's knee, which travels up-down).
8. Turn large crank to lower knee slightly.
9. Turn small handwheel to move table along X axis until cylinder is to the left of end mill. The goal is to reduce the head to a square shape of approximately  $7 \times 7 \times 3 \text{ mm}^3$ . Assuming initial plastic stock is  $5/8 \text{ in}$ , the amount to remove from each side of the cylinder is:

$$\left( \frac{5}{8} \text{ in} - \left( \frac{7 \text{ mm}}{25.4 \text{ mm in}^{-1}} \right) \right) / 2 \text{ sides} = 0.1747 \text{ in/side} \approx 0.175 \text{ in/side}$$

10. Turn large crank to raise knee until it is 0.165 in above the noted position, to make a cut of that depth.
11. Turn on spindle.
12. With travel speed set conservatively low, activate power feed to move table rightward.

13. Apply cutting fluid to cutting site with spray bottle as part feeds under cutter.
14. Raise knee by an additional 0.010 in to make a finishing pass with that much smaller depth of cut.
15. Reapply fluid and send part under cutter with power feed again.  
The side of the cylinder that was up has now been cut flat to the desired depth.
16. Loosen the vise and turn the part over (a 180° rotation about the cylinder axis). To get that angle correct:
  - Insert blade of a machinist square between vise jaws and press body of square up against outside edge of jaws.
  - Slide square up until blade contacts the flat, which is now facing downward inside the jaws, aligning the part for the next cut.
17. Clamp part in vise and repeat steps 4–15 above to mill the second flat.
18. Release part, rotate 90° using body of square (or any flat tool) as a reference pressed up against end of jaws, and re-clamp.
19. Repeat steps 4–15 above to mill the third flat.
20. Release part, rotate 180° and re-clamp.
21. Repeat steps 4–15 above to mill the final flat.
22. Release part from vise.
23. Round off all sharp edges using new fine-grit sandpaper (or a file that is free of metallic dust).

## A.3 Navigus models in OpenSCAD

### Models

#### Orthogonal base

These bases have  $120^\circ$  rotational symmetry. The axis of the cylinder which contains the ball joint is perpendicular to the bottom face of the triangle that attaches to the skull.

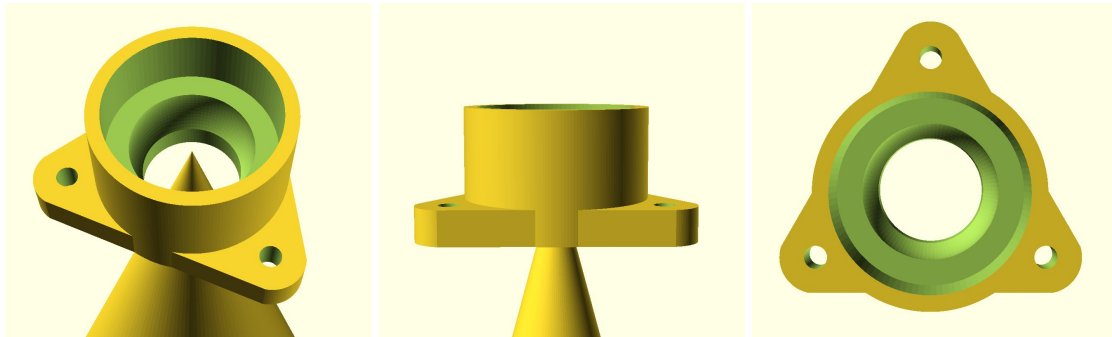


Figure A.14: **Rendering of orthogonal Navigus base in OpenSCAD.** (L–R) oblique, side and top views. A  $30^\circ$  cone has been added (except top view), emanating downward from the center of the ball joint, as a conservative estimate of the reachable volume.

#### Angled base

On angled bases, the cylinder is canted  $15^\circ$  off of orthogonal to the bottom face. The cylinder points up and away from one corner of the base and toward the opposite edge. There are two small ridges that run along the outer surface of the cylinder, on the same side of the cylinder as the corner it is angled away from.

For a given burr hole location, angled bases can point toward different targets depending on how the base is rotated about the skull surface normal vector. This is usually advantageous, but it adds an additional degree of freedom that must be considered during planning. We almost always use angled instead of orthogonal bases during our NHP surgeries. For thick-skulled subjects such as swine, the difficulty of creating an angled burr hole forces us to use orthogonal bases instead.



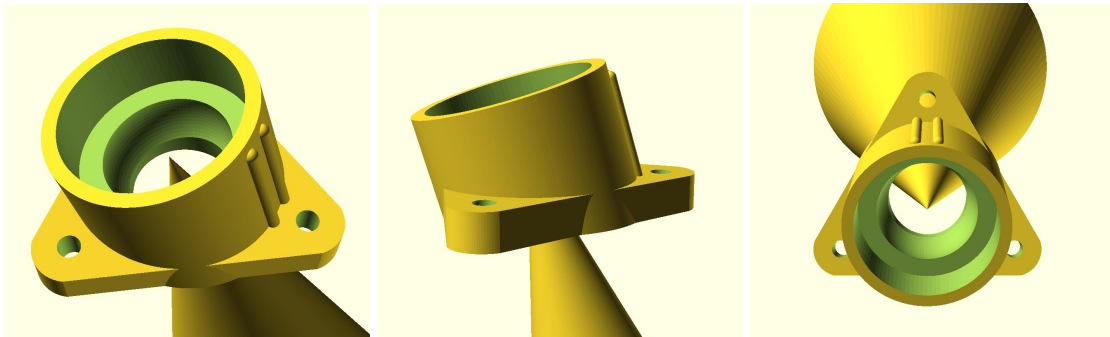


Figure A.15: **Rendering of angled Navigus base in OpenSCAD.**  
 (L–R) oblique, side and top views. A 30° cone has been added, emanating from the center of the ball joint along the axis of the cylinder, as a conservative estimate of the reachable volume.

## Using models

OpenSCAD produces STL files which are not directly readable by 3D Slicer, but can be converted to a format that is. STL files can be loaded into Kitware’s ParaView and exported in the legacy VTK format: File > Save Data... > Files of type: Legacy VTK Files (\*.vtk) > File Type: Binary > OK. Once converted to the legacy VTK format, these 3D models can be loaded in Slicer, which will recognize them as models and import them appropriately.

## Source code listing

```
// Taking the arbitrary units to be millimeters:
inch = 25.4;

// These bases appear to be designed as equilateral triangles with 1 inch sides
// (before the tips are rounded off):
side_len = 1*inch;

EL = 0.1; // An excess length factor to prevent z-fighting.

base_res = 100; // The baseline level of detail ($fn, number of fragments).
// Some parts need to be smoother, some can be coarser, so $fn is scaled up or down

module base_triangle(side_len, h) {
  translate([-side_len/2, -c_to_b, 0]) {
    linear_extrude(height = h, center = true) {
      polygon(points=[[0, 0, ],
                    [side_len, 0, ],
                    [side_len*sin(30), side_len*cos(30)]]);
    }
  }
}
```

```

}

module through_holes(diam, ctc_dist, h) {
    // Distance from triangle center to screw center
    tc_to_sc = ctc_dist / (2*cos(30));

    for(i = [90, 90+120, 90-120]) {
        rotate(a = i) {
            translate([tc_to_sc, 0, 0]) {
                cylinder(h = h,
                    d = diam,
                    $fn = base_res,
                    center = true);
            }
        }
    }
}

////////////////////////////////////
// Create bottom part of base
////////////////////////////////////
h_tri = 2.75; // Height of triangular piece
d_hole = 1.66; // Diameter of screw through holes
ctc_screw = 16.6; // Center to center sep between screws

module tri_with_holes() {
    difference() {
        base_triangle(side_len = side_len, h = h_tri);
        through_holes(diam = d_hole, ctc_dist = ctc_screw, h = h_tri + EL);
    }
}
//tri_with_holes();

// Create convex shape for rounding off triangle corners
//-----
module roundoff_block(width, h) {
    translate([0, width/2, 0]) {
        difference() {
            cube([width,width,h], center=true);

            translate([0, -width/2, 0]) {
                cylinder(h = h+EL,
                    d = width,
                    $fn = base_res,
                    center=true);
            }
        }
    }
}

module limiter_shape(diam, h) {
    // Convex polygon for limiting roundoff effect to a 120 degree range
    scale([diam, diam, 1]) {
        linear_extrude(height = h, center=true){
            polygon(points = [[0,0],
                [sqrt(3), 1],

```

```

        [sqrt(3), -1],
        [-sqrt(3), -1],
        [-sqrt(3), 1]];
    }
}

module angular_limiter(angle, r, h) {
    // Convex shape for setting angular range of corner roundoff

    // Convert from the total interior angle to the angular
    // value that will be used in trig functions
    theta = 90 - (angle/2);

    linear_extrude(height = h, center=true){
        polygon(points = [[0,0],
            [ r*cos(theta),  r*sin(theta)],
            [ r*cos(theta), -r*sin(theta)],
            [-r*cos(theta), -r*sin(theta)],
            [-r*cos(theta),  r*sin(theta)]]);
    }
}

module corner_cap(width, angle, h) {
    difference() {
        roundoff_block(width = width, h = h);
        // Set radius to 2x block width, so it's long enough even when angle is
        // small
        angular_limiter(angle = angle, r = 2*width, h = h+EL);
    }
}

// This is how far to translate the corner caps, assuming their center
// of curvature should be at the screw hole center
tr = ctc_screw/(2*cos(30));

d_cor = 5.2; // Diameter of the cylindrical roundoff on corners

module three_corner_caps() {
    for(i = [0, 120, -120]) {
        rotate(a = i) {
            translate([0, tr, 0]) {
                corner_cap(width = d_cor, angle = 120, h = h_tri + EL);
            }
        }
    }
}

module bottom_piece() {
    difference() {
        tri_with_holes();
        three_corner_caps();
    }
}

////////////////////////////////////

```

```

// Create ball joint cylinder
////////////////////////////////////
h_cyl = 10.1; // Measured height of orthogonal base
d_cyl = 15.0; // Outer diameter of cylinder on ortho and angled bases
d_in_sm = 7.65; // Inner diameter of hole at bottom of orthogonal base

d_in_lg = 12.9; // Inner diameter of large threaded hole at top
h_in_lg = 4.7; // Height of large interior tube (down from top)

d_in_sph = 9.5; // Diameter of ball joint sphere

module ortho_base_solid() {
    union() {
        translate([0, 0, h_tri/2]) {
            bottom_piece();
        }

        cylinder(h = h_cyl,
                d = d_cyl,
                $fn = 2*base_res);
    }
}
//ortho_base_solid();

// Create the hollows within the ball joint cylinder
module tube_in_small() {
    cylinder(h = 3*h_cyl,
            d = d_in_sm,
            $fn = base_res,
            center = true);
}
//tube_in_small();

module tube_in_large() {
    translate([0, 0, (h_cyl - h_in_lg)]) {
        cylinder(h = h_cyl,
                d = d_in_lg,
                $fn = base_res);
    }
}
//tube_in_large();

module sphere_in() {
    translate([0, 0, d_in_sph/2]) {
        sphere(d = d_in_sph,
              $fn = base_res);
    }
}

module cone_of_possibility(h, ang) {
    radius = h * tan(ang/2);

    translate([0, 0, -h]) {
        cylinder(h = h,
                r1 = radius,
                r2 = 0,

```

```

        $fn = base_res);
    }
}
//cone_of_possibility(60, 30);

module complete_ortho_base(alpha_cone) {
    union() {
        difference() {
            ortho_base_solid();
            tube_in_small();
            tube_in_large();
            sphere_in();
        }

        if (alpha_cone > 0) {
            translate([0, 0, d_in_sph/2]) {
                cone_of_possibility(h = h_cone,
                                    ang = alpha_cone);
            }
        }
    }
}
//complete_ortho_base();

// Make angled base
h_cone = 80; // Cone height (should be greater than target depth)

theta_cyl = 15; // I calculated 16 deg angle from my caliper measurements, but
                // literature that references the Navigus suggests that the angle is actually 15
                // deg.
//theta_cyl = 30; // This would be great for reaching some difficult targets.

c_to_b = side_len*tan(30)/2; // Distance from triangle center to back edge

h_cyl_ang_s = 8.8; // Height of cyl on short side, from rear of bottom face
h_cyl_ang_t = 13.4; // Height of cyl on tall side (before chopping everything below
                    // bottom face)

h_bottom_rear = c_to_b*tan(theta_cyl/2);
// Height of bottom center after rotation
h_bottom_center = h_tri/(2*cos(theta_cyl));

// Ridge details
h_ridges = 8.5; // Approximate length of ridges
d_ridges = 1; // Diameter of ridges
a_ridges = 7.6; // Angular separation between ridges, from cylinder axis

module ang_base_solid() {
    union() {
        // Translate so bottom center of base is at z = 0
        translate([0, 0, h_bottom_center]) {
            rotate([-theta_cyl, 0, 0]) {
                bottom_piece();
            }
        }
    }
}

```

```

difference() {
  union () {
    // Translate cylinder down by h so top face is at z=0,
    // then up by h_bottom_rear + h_cyl_ang, so top face is
    // the correct distance from bottom rear
    translate([0, 0, (-h_cyl_ang_t)+h_bottom_rear+h_cyl_ang_s]) {
      cylinder(h = h_cyl_ang_t,
              d = d_cyl,
              $fn = 2*base_res);
    }

    // Ridges
    for (a = [-a_ridges, a_ridges]) {
      rotate([0, 0, a]) {
        translate([0, d_cyl/2, 0]) {
          union() {
            cylinder(h = h_ridges,
                    d = d_ridges,
                    $fn = base_res/2);

            translate([0, 0, h_ridges]) {
              sphere(d = d_ridges,
                   $fn = base_res/2);
            }
          }
        }
      }
    }

    // Large cube to trim off excess cylinder below base
    rotate([-theta_cyl, 0, 0]) {
      translate([0, 0, -side_len/2]) {
        cube(side_len,
            center = true);
      }
    }
  }
}
//ang_base_solid();

module complete_ang_base(alpha_cone) {
  union() {
    difference() {
      ang_base_solid();

      tube_in_small();
      tube_in_large();
      sphere_in();
    }

    if (alpha_cone > 0) {
      translate([0, 0, d_in_sph/2]) {
        cone_of_possibility(h = h_cone,
                          ang = alpha_cone);
      }
    }
  }
}

```

```
    }  
  }  
}  
  
// Uncomment either of the following to get the desired base as output:  
  
// Orthogonal:  
//complete_ortho_base(alpha_cone = 30);  
  
// Angled:  
rotate([theta_cyl, 0, 0]) {  
  complete_ang_base(alpha_cone = 30);  
}
```

## A.4 Additional IMRI experiments

This appendix contains verbatim abstracts from other experiments that used our preoperative planning and IMRI device tracking method which have previously been published as journal articles (in *Molecular Therapy*, *Nature Medicine*, *EJNMMI Research*, *Biological Psychiatry*, and *Cell transplantation*) and presented as talks at the 2017, 2018, and 2019 ISMRM annual meetings. References and figures, if any, appear below the text of each abstract.

### Roseboom and Mueller et al. 2021

Abstract reproduced from:

Patrick H. Roseboom, Sascha A.L. Mueller, Jonathan A. Oler, Andrew S. Fox, Marissa K. Riedel, Victoria R. Elam, **Miles E. Olsen**, Juan L. Gomez, Matthew A. Boehm, Alexandra H. DiFilippo, Bradley T. Christian, Michael Michaelides, and Ned H. Kalin. "Evidence in primates supporting the use of chemogenetics for the treatment of human refractory neuropsychiatric disorders". In: *Molecular Therapy* (Apr. 2021)

Non-human primate (NHP) models are essential for developing and translating new treatments that target neural circuit dysfunction underlying human psychopathology. As a proof-of-concept for treating neuropsychiatric disorders, we used a NHP model of pathological anxiety to investigate the feasibility of decreasing anxiety by chemogenetically (DREADDs [designer receptors exclusively activated by designer drugs]) reducing amygdala neuronal activity. Intraoperative MRI surgery was used to infect dorsal amygdala neurons with AAV5-hSyn-HA-hM4Di in young rhesus monkeys. In vivo microPET studies with [ $^{11}\text{C}$ ]-deschloroclozapine and postmortem autoradiography with [ $^3\text{H}$ ]-clozapine demonstrated selective hM4Di binding in the amygdala, and neuronal expression of hM4Di was confirmed with immunohistochemistry. Additionally, because of its high affinity for DREADDs, and its approved use in humans, we developed an individualized, low-dose clozapine administration strategy to induce DREADD-mediated amygdala inhibition. Compared to controls, clozapine selectively decreased anxiety-related freezing behavior in the human intruder paradigm in hM4Di-expressing monkeys, while coo vocalizations and locomotion were unaffected. These results are an important step in establishing chemogenetic strategies for patients with refractory neuropsychiatric disorders in which amygdala alterations are central to disease pathophysiology.



**Tao et al. 2021**

Abstract reproduced from:

Yunlong Tao, Scott C. Vermilyea, Matthew Zammit, Jianfeng Lu, **Miles Olsen**, Jeanette M. Metzger, Lin Yao, Yuejun Chen, Sean Phillips, James E. Holden, Viktoriya Bondarenko, Walter F. Block, Todd E. Barnhart, Nancy Schultz-Darken, Kevin Brunner, Heather Simmons, Bradley T. Christian, Marina E. Emborg, and Su-Chun Zhang. “Autologous transplant therapy alleviates motor and depressive behaviors in parkinsonian monkeys”. In: *Nature Medicine* (Mar. 2021)

Degeneration of dopamine (DA) neurons in the midbrain underlies the pathogenesis of Parkinson’s disease (PD). Supplement of DA via L-DOPA alleviates motor symptoms but does not prevent the progressive loss of DA neurons. A large body of experimental studies, including those in nonhuman primates, demonstrates that transplantation of fetal mesencephalic tissues improves motor symptoms in animals, which culminated in open-label and double-blinded clinical trials of fetal tissue transplantation for PD<sup>1</sup>. Unfortunately, the outcomes are mixed, primarily due to the undefined and unstandardized donor tissues<sup>1,2</sup>. Generation of induced pluripotent stem cells enables standardized and autologous transplantation therapy for PD. However, its efficacy, especially in primates, remains unclear. Here we show that over a 2-year period without immunosuppression, PD monkeys receiving autologous, but not allogenic, transplantation exhibited recovery from motor and depressive signs. These behavioral improvements were accompanied by robust grafts with extensive DA neuron axon growth as well as strong DA activity in positron emission tomography (PET). Mathematical modeling reveals correlations between the number of surviving DA neurons with PET signal intensity and behavior recovery regardless autologous or allogeneic transplant, suggesting a predictive power of PET and motor behaviors for surviving DA neuron number.

**References**

1. Bjorklund, A. & Lindvall, O. Replacing dopamine neurons in Parkinson’s disease: how did it happen? *J. Parkinsons Dis.* 7, S21–S31 (2017).
2. Barker, R. A., Barrett, J., Mason, S. L. & Bjorklund, A. Fetal dopaminergic transplantation trials and the future of neural grafting in Parkinson’s disease. *Lancet Neurol.* 12, 84–91 (2013).

## Zammit et al. 2020

Abstract reproduced from:

Matthew Zammit, Yunlong Tao, **Miles E. Olsen**, Jeanette Metzger, Scott C. Vermilyea, Kathryn Bjornson, Maxim Slesarev, Walter F. Block, Kerri Fuchs, Sean Phillips, Viktorya Bondarenko, Su-Chun Zhang, Marina E. Emborg, and Bradley T. Christian. “[<sup>18</sup>F]FEPPA PET imaging for monitoring CD68-positive microglia/macrophage neuroinflammation in nonhuman primates”. In: *EJNMMI Research* 10 (Dec. 2020), p. 93

**Purpose:** The aim of this study was to examine whether the translocator protein 18-kDa (TSPO) PET ligand [<sup>18</sup>F]FEPPA has the sensitivity for detecting changes in CD68-positive microglial/macrophage activation in hemiparkinsonian rhesus macaques treated with allogeneic grafts of induced pluripotent stem cell-derived midbrain dopaminergic neurons (iPSC-mDA).

**Methods:** In vivo positron emission tomography (PET) imaging with [<sup>18</sup>F]FEPPA was used in conjunction with postmortem CD68 immunostaining to evaluate neuroinflammation in the brains of hemiparkinsonian rhesus macaques (n = 6) that received allogeneic iPSC-mDA grafts in the putamen ipsilateral to MPTP administration.

**Results:** Based on assessment of radiotracer uptake and confirmed by visual inspection of the imaging data, nonhuman primates with allogeneic grafts showed increased [<sup>18</sup>F]FEPPA binding at the graft sites relative to the contralateral putamen. From PET asymmetry analysis of the images, the mean asymmetry index of the monkeys was  $AI = -0.085 \pm 0.018$ . Evaluation and scoring of CD68 immunoreactivity by an investigator blind to the treatment identified significantly more neuroinflammation in the grafted areas of the putamen compared to the contralateral putamen (p = 0.0004). [<sup>18</sup>F]FEPPA PET AI showed a positive correlation with CD68 immunoreactivity AI ratings in the monkeys (Spearman’s  $\rho = 0.94$ ; p = 0.005).

**Conclusion:** These findings reveal that [<sup>18</sup>F]FEPPA PET is an effective marker for detecting increased CD68-positive microglial/macrophage activation and demonstrates sufficient sensitivity to detect changes in neuroinflammation in vivo following allogeneic cell engraftment.

## Fox et al. 2019

Abstract reproduced from:

Andrew S. Fox, Tade Souaiaia, Jonathan A. Oler, Rothem Kovner, Jae Mun (Hugo)

Kim, Joseph Nguyen, Delores A. French, Marissa K. Riedel, Eva M. Fekete, Matthew R. Rabska, **Miles E. Olsen**, Ethan K. Brodsky, Andrew L. Alexander, Walter F. Block, Patrick H. Roseboom, James A. Knowles, and Ned H. Kalin. "Dorsal Amygdala Neurotrophin-3 Decreases Anxious Temperament in Primates". In: *Biological Psychiatry* 86.12 (Dec. 2019), pp. 881–889

**BACKGROUND:** An early-life anxious temperament (AT) is a risk factor for the development of anxiety, depression, and comorbid substance abuse. We validated a nonhuman primate model of early-life AT and identified the dorsal amygdala as a core component of AT's neural circuit. Here, we combine RNA sequencing, viral-vector gene manipulation, functional brain imaging, and behavioral phenotyping to uncover AT's molecular substrates.

**METHODS:** In response to potential threat, AT and brain metabolism were assessed in 46 young rhesus monkeys. We identified AT-related transcripts using RNA-sequencing data from dorsal amygdala tissue (including central nucleus of the amygdala [Ce] and dorsal regions of the basal nucleus). Based on the results, we overexpressed the neurotrophin-3 gene, NTF3, in the dorsal amygdala using intraoperative magnetic resonance imaging-guided surgery (n = 5 per group).

**RESULTS:** This discovery-based approach identified AT-related alterations in the expression of well-established and novel genes, including an inverse association between NTRK3 expression and AT. NTRK3 is an interesting target because it is a relatively unexplored neurotrophic factor that modulates intracellular neuroplasticity pathways. Overexpression of the transcript for NTRK3's endogenous ligand, NTF3, in the dorsal amygdala resulted in reduced AT and altered function in AT's neural circuit.

**CONCLUSIONS:** Together, these data implicate neurotrophin-3/NTRK3 signaling in the dorsal amygdala in mediating primate anxiety. More generally, this approach provides an important step toward understanding the molecular underpinnings of early-life AT and will be useful in guiding the development of treatments to prevent the development of stress-related psychopathology.

## **Block et al. 2019**

Abstract reproduced from:

Walter F Block, Rasmus Birn, **Miles Olsen**, Samuel Hurley, Ethan K Brodsky, Abigail Rajala, Caitlynn Filla, Allen McMillan, Andrew L Alexander, Rick Jenison, and Luis Populin. "MR-Guided Pharmacological Intervention: Creating Causal Capabilities for fMRI". in: *the 28th Annual Meeting of the International Society for*

*Magnetic Resonance in Medicine*. Talk #1054. 2019

## **Synopsis**

Neuroscience is in need of precise interventional tools that alter local neural dynamics while monitoring whole brain network activity. We demonstrate methods to guide catheters to deliver and monitor pharmacologic alteration of a local brain region in anaesthetized Rhesus monkeys while monitoring changes in resting state functional connectivity MRI (rs-fcMRI) throughout all brain networks. Expected and unexpected alterations in rs-fcMRI after unilateral and bilateral infusions of inhibitory agents in the limbic system are provided. The approach shows promise for using the alterations to compute effective connectivity through fMRI.

## **Introduction:**

Cognitive and behavioral functions are mediated by distributed networks of neurons involving multiple cortical and subcortical brain regions. Neuroscientists rely heavily on repeated insertions of electrophysiological probes in pre-clinical models to perform causal studies of these regions at the circuit level. At the larger network level, functional magnetic resonance imaging (fMRI) has served as the cornerstone of brain mapping tools for the past twenty years. However, the spatial and temporal resolution limits of fMRI provide primarily correlative information on brain connectivity. Determining how one region causally modulates and mediates activity in other regions remains difficult with fMRI. MR-guided, localized intraparenchymal brain delivery of viral vectors (1, 2) and chemotherapeutic agents (3, 4) uses catheters with sub-mm diameters that are smaller than most electrophysiological probes. We demonstrate here methods to guide and monitor pharmacologic alteration of a local brain region in anaesthetized Rhesus monkeys while monitoring changes in resting state functional connectivity MRI (rs-fcMRI) throughout all brain networks. Proving the feasibility of these methods is essential to our future efforts to perform repeated studies in awake Rhesus subjects performing cognitive tasks before and after localized drug interventions.

## **Methods:**

Two untrained monkeys slated for euthanasia were used for initial testing. As shown in Fig. 1A, pre-surgical MRI was used to determine skull locations for craniotomies for installation of Navigus™ brain ports. After installation (Fig. 1B), real-time control of the scanner was usurped with the RtHawk portal (HeartVista,

CA)(5). The ports were aligned in real-time (Fig. 1D) to provide trajectories aimed at the central nucleus of the amygdala (CeA) using projection-based methods that determine the 3D orientation of the brain port central axis at 5 frames/sec(6, 7). Fused silica 0.7 mm catheters were then inserted into the CeA where 24 mg of muscimol (an inhibitory agent) was infused in 24 ml of buffered solution under pressure over 12 minutes, first on the right side of the brain in Fig. 1F and then later on the left side. Resting-state functional-connectivity MRI imaging (rs-fcMRI) was performed for 45 minutes prior to the unilateral infusion, 45 minutes after the unilateral infusion, and 45 minutes after the bilateral infusion.

### **Results:**

Bilateral catheters were successfully aligned and inserted into the CeA targets with sub-mm accuracy, as shown in Fig. 2. Accuracy was measured by comparing the location of tip of the catheter to the desired MR coordinates selected prior to insertion. A co-infused Gd tracer was not used to identify the infusion volume, as Gd could alter the fMRI measurements. Instead, T2-weighted imaging detected the enhanced T2 from the infusion's saline buffer, as shown in Fig. 2. Pre-infusion rs-fcMRI provides results consistent with prior studies, which have shown that the CeA is most strongly connected to the contralateral CeA [2], as shown in Fig. 3 (left). This connectivity was significantly reduced following both unilateral (Fig. 3 center) and bilateral injections of muscimol (Fig. 3 right) into the CeA, demonstrating the effectiveness of the muscimol infusions. To depict changes over a broader region, R2 adjacency matrices in Fig. 4 show statistically significant alterations in connectivity from the pre-infusion to the post-infusion resting-state connectivity maps. After unilateral or bilateral infusions, connectivity between the left and right amygdala is decreased. After a bilateral infusion, connectivity within the ipsilateral and contralateral amygdala is further reduced. Significant controversies arise when deriving effective connectivity models (directionality) from BOLD fMRI time series using Conditional Grainger Causality (CGC). However, the ability to compare signals before and after inhibiting a node(s) allows us to provide estimates of directional influence, as shown in Fig. 5. Besides simply attenuating connectivity with the contralateral side, CGC analysis shows unexpected new connectivity after the unilateral infusion. Upon the bilateral infusion, global effective connectivity in the region is reduced.

### **Discussion:**

Though demonstrated in anesthetized NHP models for feasibility, we believe permanent brain ports can be affixed to skulls in a surgical setting which can provide long-term access for repeated catheter insertions for studies in awake models performing cognitive tasks. We have already trained other NHP models to remain still and perform cognitive tasks in the magnet.

### **Conclusion:**

The first feasibility studies for performing casual experiments to alter the functional organization and dynamics of brain networks have been completed. Expected and unexpected changes in resting state functional connectivity resulted from unilateral and bilateral infusions of inhibitory agents. Further development will allow us to test hypotheses about network topology and information flow, as well as to further the understanding of the mechanisms underlying the signals provided by fMRI.

### **Acknowledgements**

We graciously acknowledge support of research funding from the UW-Madison 2020 program and the UW-Madison Radiology Research and Development Fund.

### **References**

1. Richardson RM, Kells AP, Rosenbluth KH, Salegio EA, Fiandaca MS, Larson PS, Starr PA, Martin AJ, Lonser RR, Federoff HJ, Forsayeth JR, Bankiewicz KS. Interventional MRI-guided putaminal delivery of AAV2-GDNF for a planned clinical trial in Parkinson's disease. *Molecular therapy : the journal of the American Society of Gene Therapy*. 2011;19(6):1048-57. doi: 10.1038/mt.2011.11. PubMed PMID: 21343917; PMCID: 3129792.
2. Kalin NH, Fox AS, Kovner R, Riedel MK, Fekete EM, Roseboom PH, Tromp do PM, Grabow BP, Olsen ME, Brodsky EK, McFarlin DR, Alexander AL, Emborg ME, Block WF, Fudge JL, Oler JA. Overexpressing Corticotropin-Releasing Factor in the Primate Amygdala Increases Anxious Temperament and Alters Its Neural Circuit. *Biol Psychiatry*. 2016;80(5):345-55. doi: 10.1016/j.biopsych.2016.01.010. PubMed PMID: 27016385; PMCID: 4967405.
3. Lonser RR, Warren KE, Butman JA, Quezado Z, Robison RA, Walbridge S, Schiffman R, Merrill M, Walker ML, Park DM, Croteau D, Brady RO, Oldfield EH. Real-time

image-guided direct convective perfusion of intrinsic brainstem lesions. Technical note. *Journal of neurosurgery*. 2007;107(1):190-7. doi: 10.3171/JNS-07/07/0190. PubMed PMID: 17639894.

4. Sampson JH, Raghavan R, Provenzale JM, Croteau D, Reardon DA, Coleman RE, Rodriguez Ponce I, Pastan I, Puri RK, Pedain C. Induction of hyperintense signal on T2-weighted MR images correlates with infusion distribution from intracerebral convection-enhanced delivery of a tumor-targeted cytotoxin. *AJR Am J Roentgenol*. 2007;188(3):703-9. doi: 10.2214/AJR.06.0428. PubMed PMID: 17312057.
5. Santos JM, Wright GA, Pauly JM. Flexible real-time magnetic resonance imaging framework. *Conf Proc IEEE Eng Med Biol Soc*. 2004;2:1048-51. PubMed PMID: 17271862.
6. Olsen ME, Brodsky EK, Oler JA, Fekete EM, Riedel MK, N.H. K, Block WF, , editors. Rapid Localization for prospective stereotaxy: Using computation instead of imaging. *Proc of ISMRM 24th Annual Meeting 2016; Singapore*.
7. Brodsky EK, Olsen ME, Oler JA, Fox AS, Kovner RL, Riedel MK, Fekete EM, Roseboom PH, Tromp DPM, Grabow BP, Fudge JL, Alexander AL, Emborg ME, N.H. K, Block WF, editors. MRI-Guided Delivery of Viral Vectors for Targeted Alteration of Neurochemistry. *National Center for Targeted Alteration of Neurochemistry. National Center for Image Guided Therapy Workshop; 2016; Bethesda, MD*.

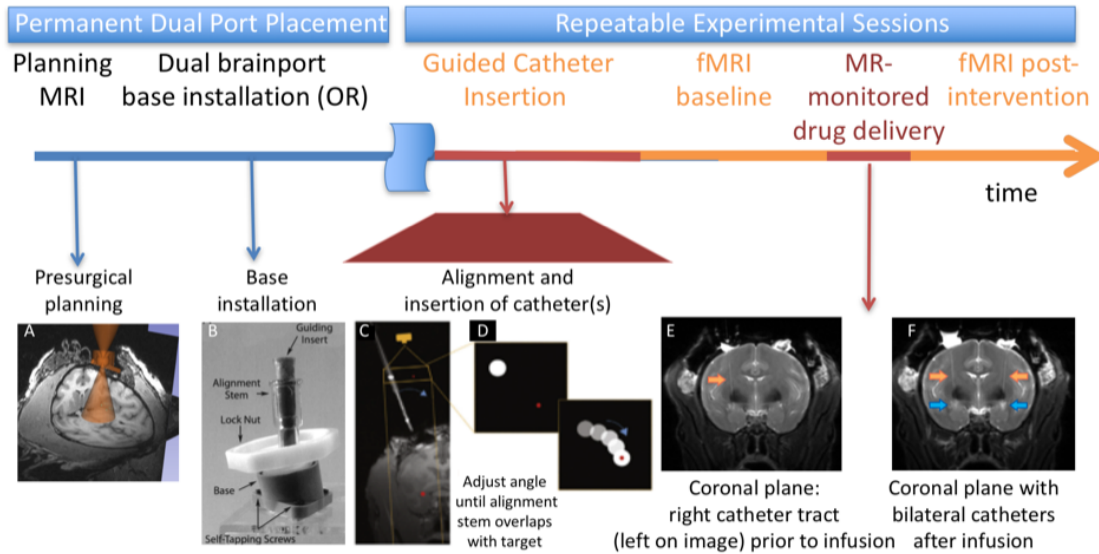


Figure A.16: **Block2019 Fig. 1**

Figure 1: Experimental timeline (Top). A) MRI is obtained to plan ideal brain guideport placements to reach desired brain regions. B) Brain guideport base is installed in OR C) MR-guided insertion of catheter(s) to targets. D) Rapid brain guideport alignment (5 frames/sec). E) One of 2 catheter tracts is visible in slice in (orange arrow) prior to drug delivery. fMRI baseline is acquired followed by MR-monitoring drug delivery. F) Spatial extent of drug delivery shown by T2-enhanced regions (blue arrows) during post-intervention fMRI.



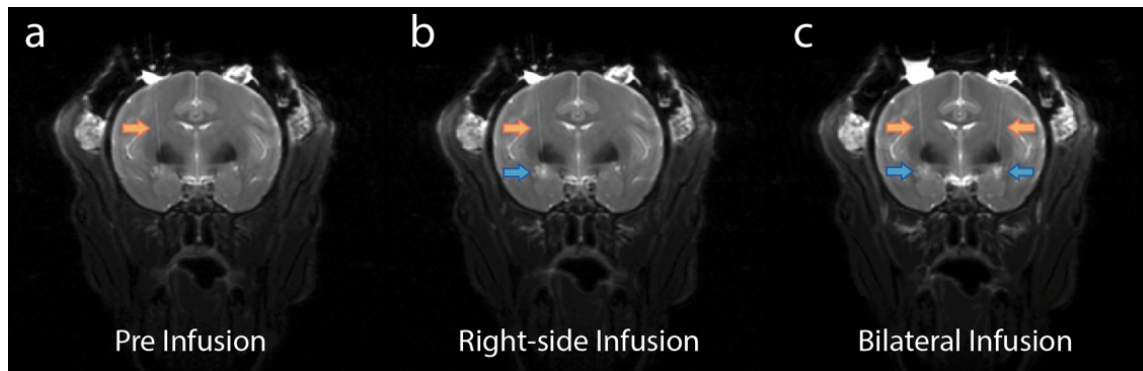


Figure A.17: **Block2019 Fig. 2**

Figure 2: Functional connectivity of the right central amygdala nucleus (CeA, blue arrow) before unilateral (right) and bilateral injection of muscimol in the CeA. Significant functional connectivity to contralateral Ce (green arrow) is seen pre-injection and is absent after both uni- and bi-lateral infusions.

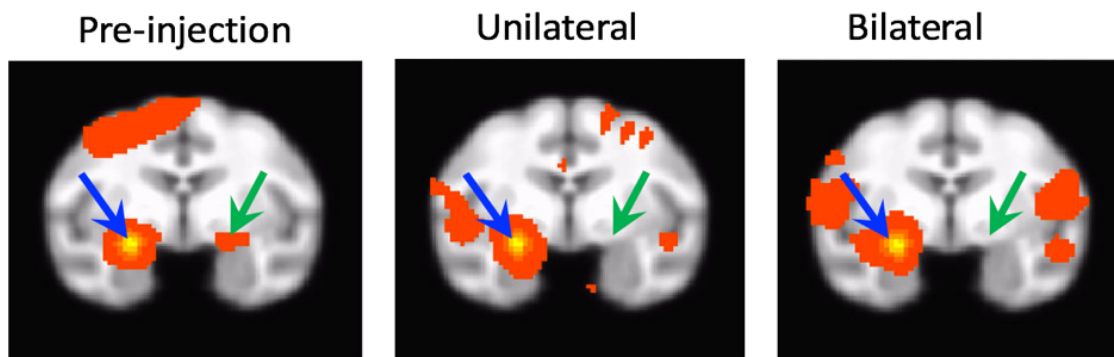


Figure A.18: **Block2019 Fig. 3**

Figure 3: Functional connectivity of the right central amygdala nucleus (CeA, blue arrow) before unilateral (right) and bilateral injection of muscimol in the CeA. Significant functional connectivity to contralateral Ce (green arrow) is seen pre-injection and is absent after both uni- and bi-lateral infusions.

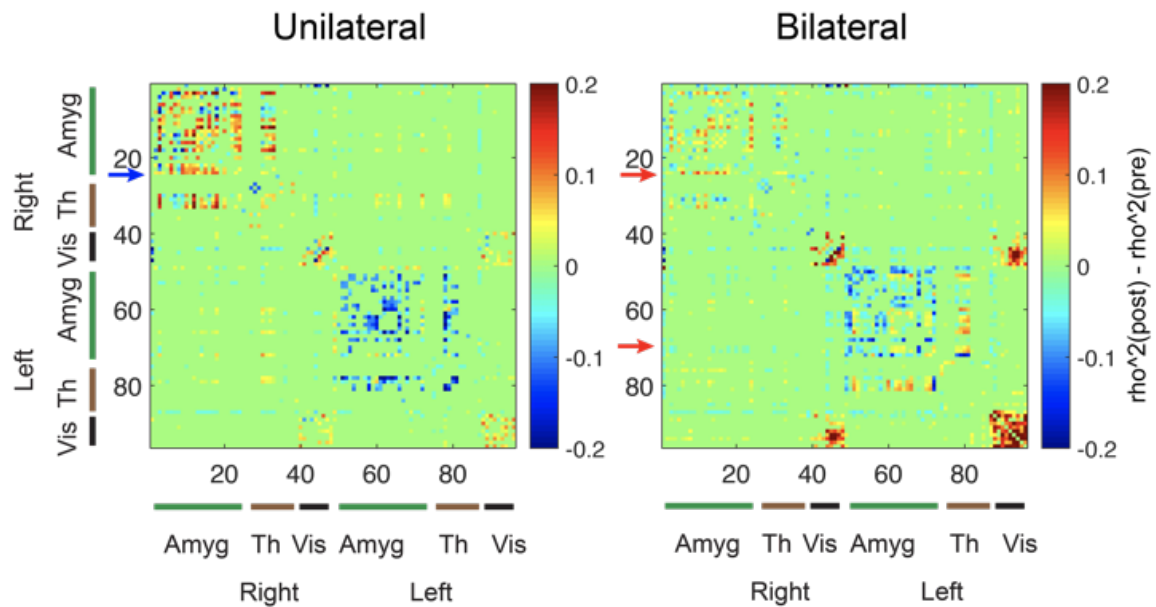


Figure A.19: Block2019 Fig. 4

Figure 4: Difference (post – pre infusion) R2 adjacency matrices following unilateral and bilateral injection. Warm colors reflect statistically significant increases in connectivity following injection and cool colors reflect significant decreases in connectivity. Subcortical regions of the amygdala and thalamus, and visual cortex regions are shown as an example. Unilateral infusion matrix: The cool colors in the lower right corner demonstrate decreased connectivity with the contralateral amygdala after infusion. Bilateral matrix: Bilateral infusions reduce connectivity between each amygdala, with some increased connectivity to the visual cortex.

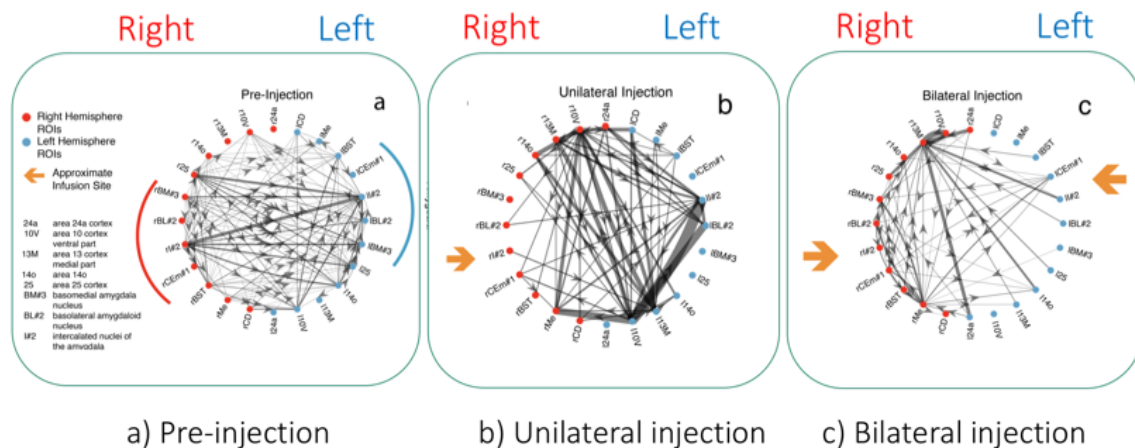


Figure A.20: **Block2019 Fig. 5**

Figure 5: State-Space Causal Grainger Connectivity models fit to 45 min of rsfMRI under no infusion (a), unilateral infusion on right side (orange arrow) (b), and bilateral infusion (c), targeted at the central nucleus of the amygdala. Directional edges reflect statistically significant influence based on non-parametric permutation tests corrected for FDR ( $p < .05$ ). Rather than simply eliminating existing connections, inhibition of the central amygdala creates new connections as well.

## Brady et al. 2018

Abstract reproduced from:

Martin Brady, Raghu Raghavan, Peng Wang, **Miles Olsen**, Ethan K. Brodsky, Terrence Oakes, Andrew L. Alexander, and Walter F. Block. "Real-time MR Brain Infusion Monitoring Enables Accurate Prediction of End Drug Distribution". In: *the 27th Annual Meeting of the International Society for Magnetic Resonance in Medicine*. Talk #0604. 2018

## Synopsis

The heterogeneity of the brain makes designing a desired end drug distribution through pressurized catheters difficult. We present a method to utilize real-time MR monitoring of a co-infused Gd tracer during initial stages of the infusion to derive a real-time 3D estimate of the velocity front. We demonstrate considerable improvement in predicting the actual drug distribution using the MR real-time data in four cases using a large animal surgical model.

## Introduction

As brain cancer and rare genetic brain diseases require treatments capable of bypassing the blood-brain barrier over wide regions, a procedure known as convection-enhanced delivery (CED) uses catheters inserted into brain tissue to infuse new therapeutics. CED is being used in multiple clinical trials, often treating an entire hemisphere over 2-3 days. However, the brain presents a very complex as well as dynamic topography for fluid flow [1] so that it is impossible for a surgeon to form a mental map for the likely final distribution of the drug based only on pre-surgical clinical imaging. In fact, the interpretation of past failed trials has often been clouded by questions on where the therapeutic was actually delivered[2].

Building upon a retrospective trial[3], we demonstrate the value of real-time MRI to (i) capture the relatively slow fluid expansion during the first 20-40 minutes of the infusion; (ii) calculate a velocity front at each point along a 3D surface on the advancing infusion, and (iii) utilize the velocity front in a brain drug predictive algorithms to predict the final spatial distribution. We present prospective predictions in four image-guided swine surgeries, compare them to the actual end distribution, and compare them with our best prediction based upon pre-surgical planning alone.

## Methods

Real-time MR qualitative infusion monitoring has previously recognized issues such as backflow [4]. However, the real-time data is not leveraged to predict the actual final distribution and thus detecting and controlling errant distributions is difficult.

As MRI can segment parenchymal components and map the geometry of fluid pathways, it is promising for planning, predicting, and monitoring CED infusions. Our prediction estimation model, illustrated in Figure 1, computes changes in drug concentration as the sum of a diffusion term, bulk flow due to CED, and losses due to movement out of the parenchyma[5].

Initializing the algorithm, however, requires assumptions on flow mechanics at the catheter tip. We replace these assumptions by generating a 3D velocity front along the expanding infusion surface, co-infused with a Gd tracer. By waiting a moderate duration after infusion initiation (tens of minutes), the infusion front travels a moderate distance from the catheter tip, as shown in Figure 2. A 3D velocity boundary vector at the infusion front is derived from a difference image between sequential volumetric images.

We guided 0.7 mm diameter CED catheters bilaterally into four swine models using a customized guidance platform[6] on a GE PET/MR scanner. Infusions of 5 mL/min extended for 140 minutes, resulting in a total infused volume of 700 mL. IR-prepped 3D GRE scans monitored the infusion.

## Results

High resolution is needed to measure the slow moving velocity front. We initially used 3D GRE dual flip angles scans (6 and 34 degrees) to measure the velocity front[3]. Though this approach could quantify the spatial tracer concentration, we have transitioned to simply thresholding an inversion-recovery prepped 3D GRE sequences (BRAVO, MP-RAGE to increase resolution. Typical parameters include a 512 x 512 x 80 image matrix at 0.35 x 0.35 x 0.8 mm resolution acquired over 4 minutes. A typical velocity front estimation is shown in Figure 2.

In general, the value of real-time MRI to enhance final drug distribution prediction is greater on edges of the infusion than in the center. In the case in Figure 3, the color overlay of the pre-surgical prediction (middle row) significantly extends beyond the grayscale enhancement that indicates the final distribution, particularly lower in the images. The infusion shape predicted from the proposed method (bottom row) matches much more closely with the actual infusion. In the surgical case in Figure 4, there is higher concordance between both predictions and the actual infusion, though the value of the proposed method is evident on the edge of the infusion (row f). The value of real-time monitoring is quite clear in the case of Figure 5, where unexpected backflow is captured by the proposed method and correctly estimates the infusion distribution (bottom row).

## Discussion

Every catheter design offers different backflow characteristics [4, 7, 8]. While the commercial pre-operative planning system available today (Figure 1) accommodates only one catheter design [9], trials have been supplanted with more advanced designs [7, 10-12]. Our approach liberates the predictive algorithm from detailed accounting of the backflow characteristics and thus offers significantly greater utility.

## Conclusion

We have presented an advance in guided intraparenchymal drug delivery using real-time MRI monitoring to more accurately predict final drug distribution. Given

the difficulty and variability of intraparenchymal drug distributions, MRI provides high added value to assist neurosurgeons in delivering the intended treatment.

### **Acknowledgements**

We gratefully acknowledge NIH funding 5R44CA177205-03. We also acknowledge Dan Consigny for his assistance in designing and executing the pre-clinical experiment.

### **References**

1. R. Raghavan, Brady, Martin L., and Sampson, John H. , "Delivering therapy to target: improving the odds for successful drug development," *Therapy Delivery*, vol. 7, pp. 457 - 481, 2016.
2. J. H. Sampson, G. Archer, C. Pedain, E. Wembacher-Schroder, M. Westphal, S. Kunwar, et al., "Poor drug distribution as a possible explanation for the results of the PRECISE trial," *J Neurosurg*, vol. 113, pp. 301-9, Aug 2010.
3. M. Brady, R. Raghavan, A. L. Alexander, and W. F. Block, "Controlling Brain Infusion Distributions: Moving from Surgical Planning to Real-Time MR Guidance," in *International Society of Magnetic Resonance in Medicine*, Honolulu, Hawaii, 2017, p. 5419.
4. M. Brady, Raghavan, R, Alexander, A, Kubota, K, Sillay, K and Emborg, ME, "Pathways of infusate loss during convection-enhanced delivery into the putamen nucleus," *Stereotact Funct Neurosurg*, vol. 91, pp. 69-78, 2013.
5. R. Raghavan and M. Brady, "Predictive models for pressure-driven fluid infusions into brain parenchyma," *Phys Med Biol*, vol. 56, pp. 6179-204, Oct 7 2011.
6. N. H. Kalin, A. S. Fox, R. Kovner, M. K. Riedel, E. M. Fekete, P. H. Roseboom, et al., "Overexpressing Corticotropin-Releasing Factor in the Primate Amygdala Increases Anxious Temperament and Alters Its Neural Circuit," *Biol Psychiatry*, vol. 80, pp. 345-55, Sep 01 2016.
7. M. Brady, Raghavan, R, Singh, D., Anand, PJ, Fleisher, AS, Mata, J, Broaddus, WC, and Olbricht, WL, "In vivo performance of a microfabricated catheter for intraparenchymal delivery," *J Neurosci Methods*, vol. 229, pp. 76-83, May 30 2014.

8. M. L. Brady, Raghavan, R., Block, W., Grabow, B., Ross, C., Kubota, K., Alexander, A., and Emborg, M. E., "The Relation between Catheter Occlusion and Backflow during Intraparenchymal Cerebral Infusions," *Stereotactic and Functional Neurosurgery*, vol. 93, pp. 102 - 109, 2015.

## Figures

### Neurosurgical Planning of Drug Delivery Today is Limited Today to Pre-operative Planning

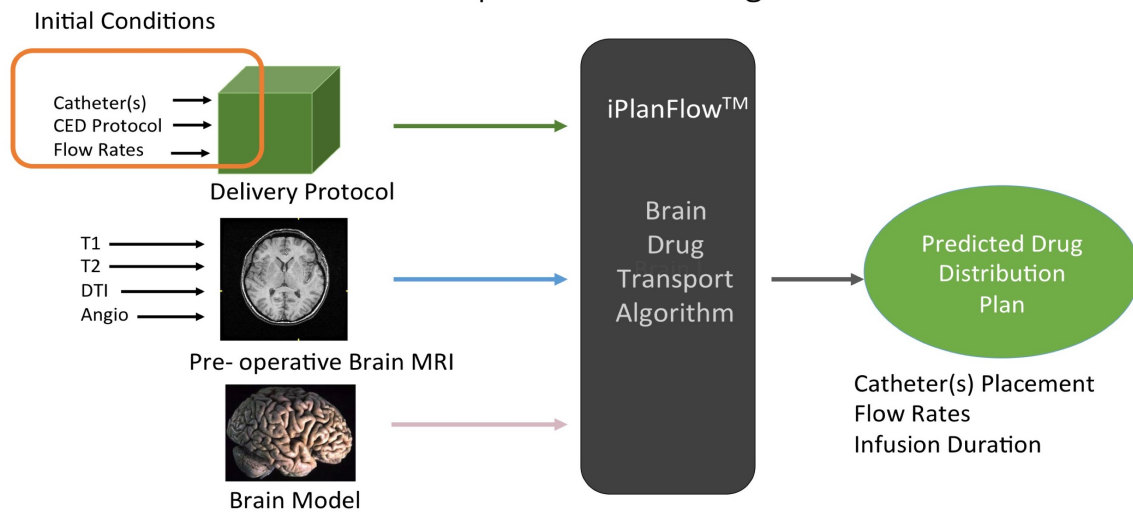
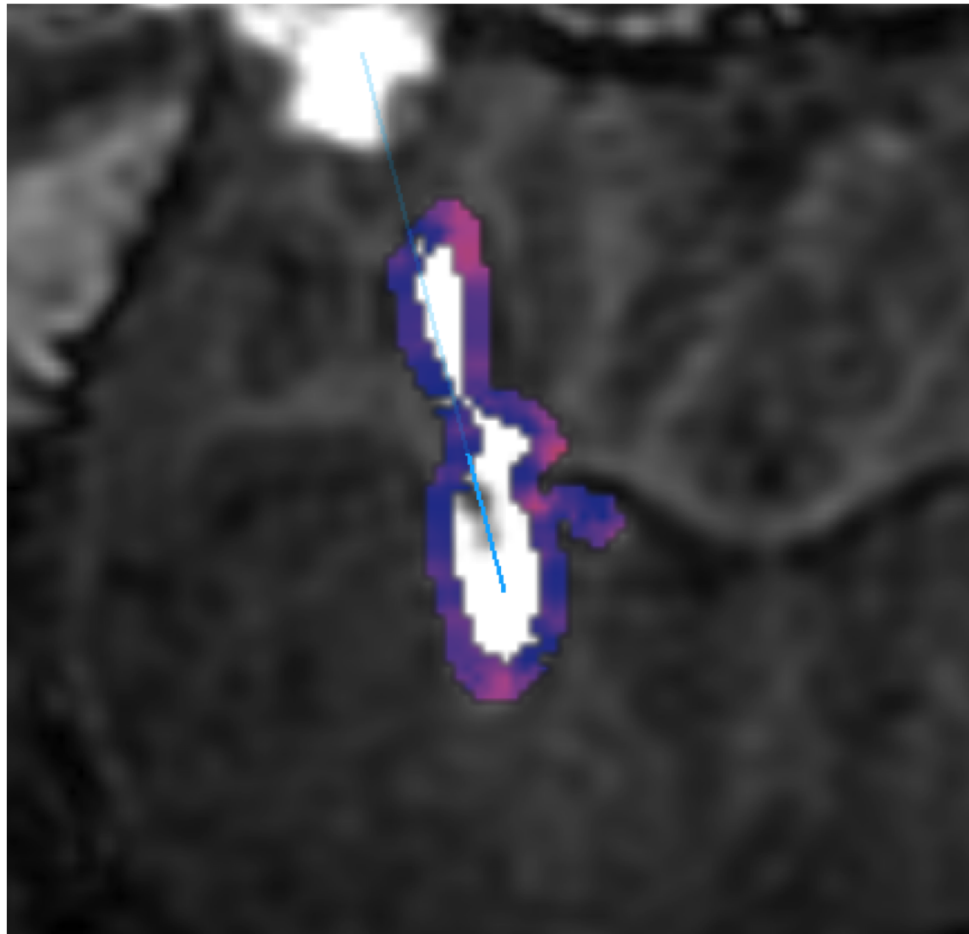


Figure A.21: **Brady2018 Fig. 1**

Pre-operative MRI is used to segment the brain as an input to a commercial, brain drug transport algorithm (iPlanFlow™, Brainlab) that provides predicted drug distribution for given catheter(s) placement, flow rate, and flow duration.



Velocity color map

Figure A.22: **Brady2018 Fig. 2**

Estimation of infusion front velocities are three dimensional vectors, shown here as speeds with the corresponding color map. Slow infusion expansion leads (0.5 mm/s in places, shown in blue in Figure) causes the sequential 3D IR GRE scans to differ often by less than a voxel. We utilize a sub-voxel method to successfully resolve these low velocities.



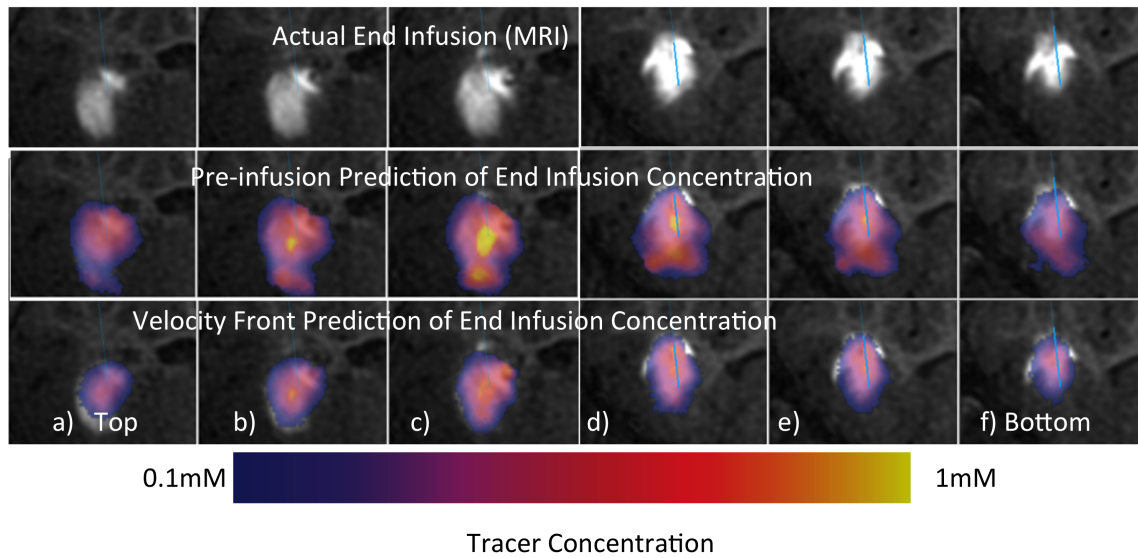


Figure A.23: **Brady2018 Fig. 3**

End drug distribution prediction generated using velocity front calculation from real-time MRI monitoring (color overlays in bottom row) matches actual end drug distribution as indicated in tracer enhancement pattern (top row). The conventional end drug prediction using only pre-surgical planning (middle row), which mimics current operating room guidance, considerably over-estimates the size of the infusion. Top three slices (a-c) and bottom three slices (d-f)

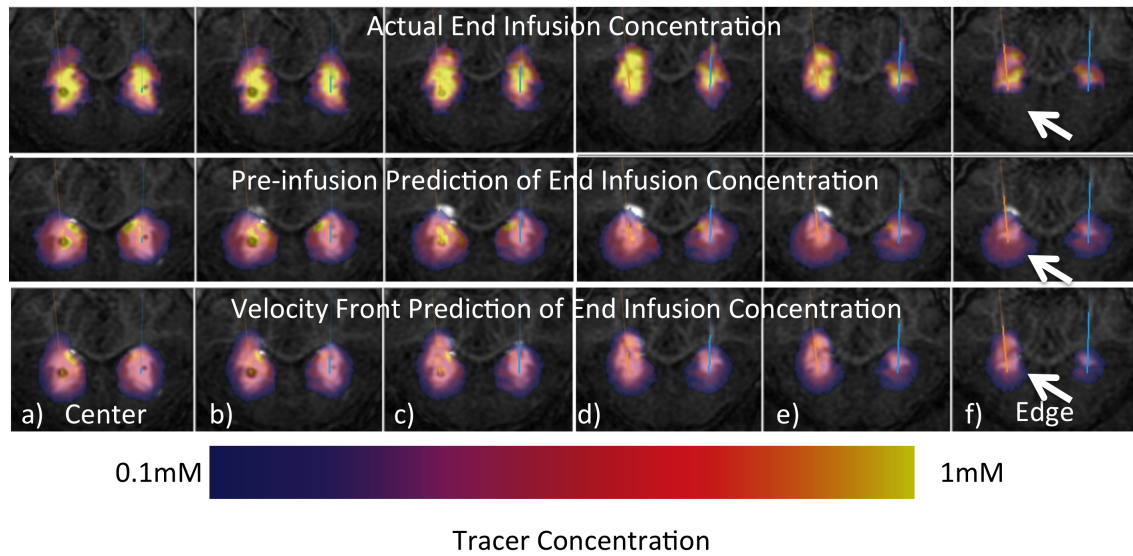
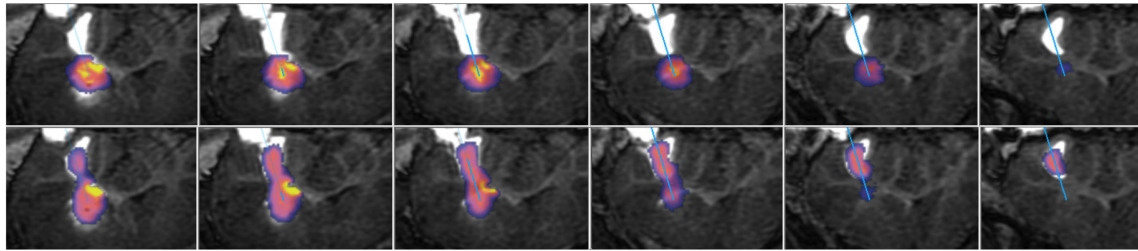


Figure A.24: **Brady2018 Fig. 4**

Value of real-time prediction of end drug distribution grown as one moves away from the infusion center (column a) towards the infusion edge (column f). Top row: Actual end distribution concentration. Middle row: Conventional end drug prediction using only pre-surgical planning mimics current operating room guidance. Bottom row: End drug distribution using velocity front calculation from real-time MRI monitoring. All three rows coincide well at the center (column a) but the velocity front prediction coincides with the actual infusion much better than the pre-surgical prediction on the edge of the infusion (see white arrows).

Pre-surgical Planning Prediction(Color Overlay) vs. Actual End Infusion (Grayscale)



Velocity Front Planning Prediction(Color Overlay) vs. Actual End Infusion (Grayscale)

Figure A.25: Brady2018 Fig. 5

Top Row: Backflow along catheter tract causes significant changes in actual drug distribution (grayscale) relative to the color overlay generated from the pre-surgical planning simulation.. Bottom row: Using the velocity front to update the prediction algorithm creates much better concordance between the predicted distribution ( color overlay) and the actual distribution (grayscale)

## Olsen et al. 2017

Abstract reproduced from:

**Miles Olsen**, Scott Vermilyea, Jianfeng Lu, Ethan Brodsky, Scott Guthrie, Yunlong Tao, Eva Fekete, Marissa Riedel, Kevin Brunner, Carissa Boettcher, Viktorya Bondarenko, Andrew Alexander, Su-Chun Zhang, Marina Emborg, and Walter Block. "Targeted Delivery of Stem Cells to the Brain using Real Time Interventional MRI". in: *the 26th Annual Meeting of the International Society for Magnetic Resonance in Medicine*. Talk #0738. 2017

### Synopsis

We present an intraoperative MRI protocol for stereotaxic surgery to precisely deliver induced pluripotent stem cells to targeted locations within the brain of a non-human primate model.

Previously, these surgeries were performed in stereotaxic operating rooms with no intraoperative imaging, or in a conventional MRI system without real-time guidance. Those environments complicate the goals of ensuring precise cannula tip placement before injection, and being able to perform the desired number of injections during the anesthesia window. Our platform enables surgeons to quickly achieve precise tip placement, and confirm via imaging that cells were deposited at the intended target.

**PURPOSE:**

The vast majority of in-vivo stem cell delivery procedures in complex pre-clinical and human studies are performed under stereotaxic guidance. MRI guidance and monitoring of stem cell delivery offers several advantages in monitoring the precise location of delivery and characterizing distribution, however the overall duration of the MR procedure imperils stem cell survival rates. We present an ensemble of rapid guidance and monitoring capabilities that promote the value of MR guidance while minimizing the interval cells reside in the dangerous period between bioreactor and injection. We demonstrate the value of the real-time intraoperative MRI (RT-IMRI) in the successful delivery of neuroprogenitor-induced pluripotent stem cells (iPSCs) to the putamen of 9 non-human primate (NHP) models of Parkinson's disease in survival experiments spanning several months[1].

**METHODS:**

The real-time interventional MRI (RT-MRI) system consists of rapid cannula trajectory planning, device alignment, device insertion, and validation imaging after stem cell transplantation. Our system allows the operator to visualize the possible brain parenchyma trajectories, as shown in Figure 1, that are possible for any fixation point of a simple trajectory guide[2] (Navigus, Medtronic, Minneapolis, MN). The caudate and commissural putamen are both considered as potential iPSC targets, and the Navigus trajectory guide has a limited range of motion – a cone with apex angle of  $36^\circ$ . Thus, careful preoperative planning is required to determine a suitable mounting configuration for the guide, such that all targets will be reachable once the subject is in the MR bore. The trajectory guide is mounted ovetop a burr hole roughly 10 mm in diameter and affixed to the skull with 3 small screws.

Once the desired trajectory has been selected, a computational approach is utilized to rapidly compute the centerline of the MR visible portion of the trajectory guide and align it with the desired trajectory. The computational approach, rather than imaging the entire alignment stem at high resolution[3], provides aiming feedback at 5 updates per second to the operator, enabling smooth intuitive motions and approximating the feel of stereotaxic OR tracking. All scanning was completed in a GE 3T 750 scanner (Waukesha, WI). A single channel 3-inch surface coil placed upon the skull around the trajectory guide provided signal reception.

The large size of stem cells relative to other commonly infused agents limits prevents them from convecting, which limits the utility of an added Gd tracer for visualizing the cell distribution. Furthermore, the iPSC team wants to avoid introducing any Gd, as a precaution against metal toxicity in the vulnerable stem

cells and surrounding tissue. Instead, we use an IR-prep spoiled gradient echo sequence which shows hypointense signal from the artificial cerebrospinal fluid (aCSF) buffering the cells. The difference between these contrast mechanisms is shown in Figure 2.

Minimizing the interval between transferring the iPSCs-derived neurons from the bioreactor, loading them into the cannula, and inserting the cannula from the surface of the brain to the desired target is crucial to maximize stem cell survival. Our RT-MRI system automatically determines and initiates scan planes collinear with the cannula trajectory to minimize this time.

## **RESULTS AND DISCUSSION:**

Our protocol is able to achieve a speed closer to that of the stereotaxic OR, while maintaining the key benefit of IMRI: the ability to acquire intraoperative images that enable good targeting precision. By moving faster than classic IMRI techniques, we are able to perform all the desired injections within the window of time that the subject may be under general anesthesia.

In each preoperative plan, we identified a location and orientation for the base that would allow all four potential targets to be reached from a single Navigus base. Each insertion and set of deposits was carried out within the window of time cells are capable of surviving within the cannula as determined by *in vitro* testing of the cannula/pump system [1] The negative contrast of the artificial CSF provides a good visual indicator of the injection location and extent (Figures 2, 3 and 4)

Quite often, the hypointense signal around a deposit will contain a small hyperintense center. The appearance varies from one deposit to the next (Figure 4) and we hypothesize that this may be due to variation in the clumping of the neurospheres.

## **CONCLUSIONS AND FUTURE WORK:**

Additional *in-vitro* experiments may be warranted to investigate the observed variation in macroscale organization of the neurospheres after injection

It could be worthwhile to employ a bSSFP sequence that will yield high signal from CSF and could improve conspicuity of the cell deposit in early images, before the artificial CSF has diffused out into the brain tissue.

## Acknowledgements

We acknowledge institutional support from GE Healthcare given to the Medical Physics and Radiology departments here. We thank HeartVista (Menlo Park, CA) for their technical support with the RTHawk software, and Graham Wright's lab at the Sunnybrook Research Institute (Toronto, ON) for their work on the Vurtigo RT-IMRI visualization software.

## References

1. Vermilyea, S. C., Lu, J., Olsen, M., Guthrie, S., Tao, Y., Fekete, E. M., ... & Brodsky, E. (2016). Real-Time Intraoperative MRI Intracerebral Delivery of Induced Pluripotent Stem Cell-Derived Neurons. *Cell Transplantation*.
2. Hall, W. A., Liu, H., & Truwit, C. L. (2000). Navigus trajectory guide. *Neurosurgery*, 46(2), 502.
3. Truwit C and Liu H. Prospective stereotaxy: a novel method of trajectory alignment using real-time image guidance. *JMRI*. 2001;13(3):452–457.
4. Kalin, N. H., Fox, A. S., Kovner, R., Riedel, M. K., Fekete, E. M., Roseboom, P. H., ... & McFarlin, D. R. (2016). Overexpressing Corticotropin-Releasing Hormone in the Primate Amygdala Increases Anxious Temperament and Alters Its Neural Circuit. *Biological psychiatry*.

## Figures

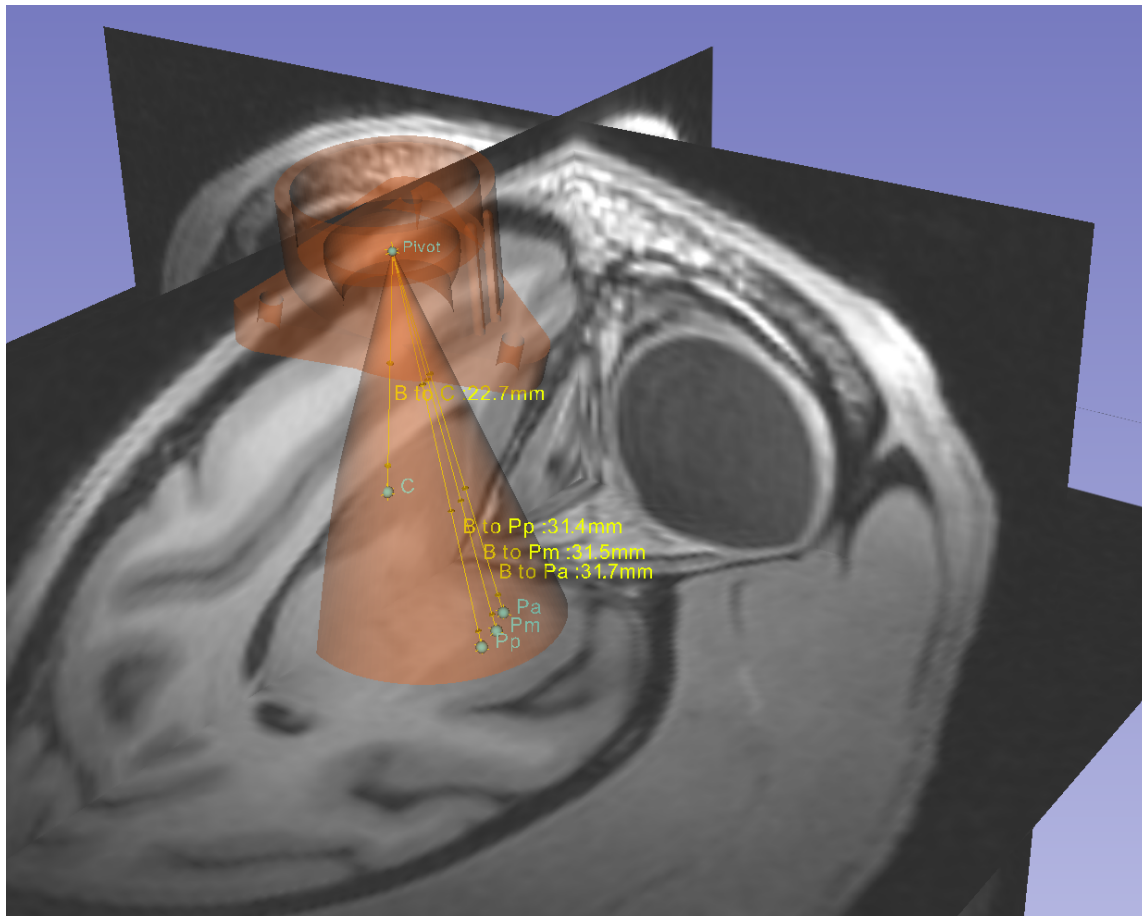


Figure A.26: Olsen2017 Fig. 1

Figure 1: Preoperative MRI of primate head with overlaid 3D model of trajectory guide base and reachable cone (transparent orange). The rulers (yellow) indicate the paths through the trajectory guide base toward the targets (blue) – one in the caudate and three in the putamen near the anterior commissure.

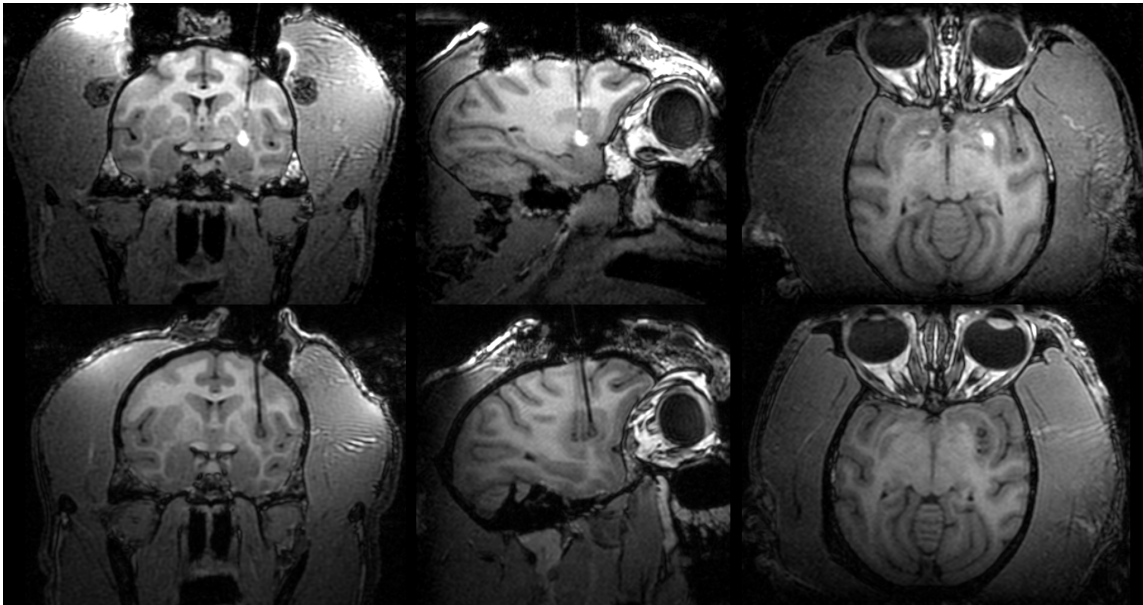


Figure A.27: Olsen2017 Fig. 2

Figure 2: (**Top row**) Example of high conspicuity positive contrast Gd-doped infusate from CED surgery performed in previous work with this platform [4]. (**Bottom row**) negative contrast in iPSC delivery in three separate tracks into the commissural putamen. The cannula is still in place at the most anterior track.

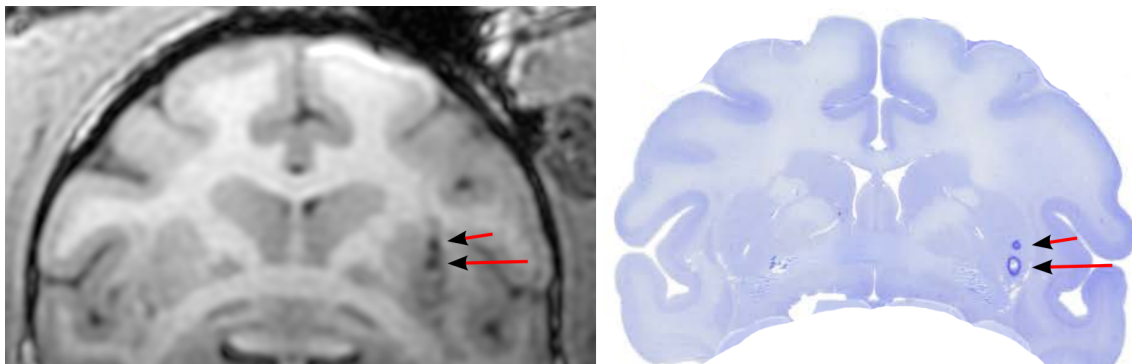


Figure A.28: Olsen2017 Fig. 3

Figure 3: (a) Slice from MR volume acquired after deposits in second insertion (arrowheads). (b) Sectioned and histologically stained brain tissue, matched to coronal slice further confirms the sites of cell deposit in pilot subject.



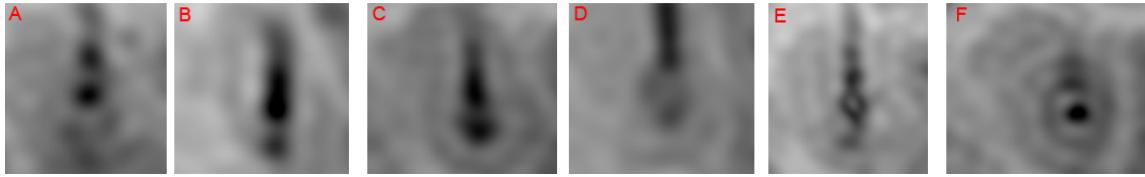


Figure A.29: Olsen2017 Fig. 4

Figure 4: Closeups of right putamen, showing varying degrees of macro scale organization: a hyperintense point is sometimes seen within the hypointense signal of the artificial CSF in a deposit. (A) Clearly separated deposits. (B, C) Cases where two deposits run together. (D) A large diffuse signal, isointense to tissue. (E) A small hyperintensity within hypointensity. (F) A hyperintense ring around the deposit.

## Vermilyea et al. 2017

Abstract reproduced from:

Scott C Vermilyea, Jianfeng Lu, **Miles Olsen**, Scott Guthrie, Yunlong Tao, Eva M Fekete, Marissa K Riedel, Kevin Brunner, Carissa Boettcher, Viktorya Bondarenko, Ethan Brodsky, Walter F Block, Andrew Alexander, Su-Chun Zhang, and Marina E Emborg. “Real-time intraoperative MRI intracerebral delivery of induced pluripotent stem cell-derived neurons”. In: *Cell Transplantation* 26.4 (2017), pp. 613–624

Induced pluripotent stem cell (iPSC)-derived neurons represent an opportunity for cell replacement strategies for neurodegenerative disorders such as Parkinson’s disease (PD). Improvement in cell graft targeting, distribution, and density can be key for disease modification. We have previously developed a trajectory guide system for real-time intraoperative magnetic resonance imaging (RT-IMRI) delivery of infusates, such as viral vector suspensions for gene therapy strategies. Intracerebral delivery of iPSC-derived neurons presents different challenges than viral vectors, including limited cell survival if cells are kept at room temperature for prolonged periods of time, precipitation and aggregation of cells in the cannula, and obstruction during injection, which must be solved for successful application of this delivery approach. To develop procedures suitable for RT-IMRI cell delivery, we first performed in vitro studies to tailor the delivery hardware (e.g., cannula) and defined a range of parameters to be applied (e.g., maximal time span allowable between cell loading in the system and intracerebral injection) to ensure cell survival. Then we performed an in vivo study to evaluate the feasibility of applying the system to nonhuman primates. Our results demonstrate that the RT-IMRI delivery system provides valuable guidance, monitoring, and visualization during

intracerebral cell delivery that are compatible with cell survival.

**DISCARD THIS PAGE**

## COLOPHON

---

This dissertation is set in T<sub>E</sub>X Gyre Pagella, which is based on Zapf's Palatino.

I am grateful to Will Benton (2008) for the L<sup>A</sup>T<sub>E</sub>X UW thesis template that this document uses. Thanks to Steven Baumgart (2012) as well, for improvements to the template. Finally, thanks to Nick Bevins (2012) and John Garrett (2017) of Medical Physics, for more recent updates to the template.

## BIBLIOGRAPHY

- 
- [1] R Hunt Bobo, Douglas W Laske, Aytac Akbasak, Paul F Morrison, Robert L Dedrick, and Edward H Oldfield. "Convection-enhanced delivery of macromolecules in the brain". In: *Proceedings of the National Academy of Sciences* 91.6 (1994), pp. 2076–2080.
- [2] R. G. Thorne and C. Nicholson. "In vivo diffusion analysis with quantum dots and dextrans predicts the width of brain extracellular space". In: *Proceedings of the National Academy of Sciences* 103.14 (Apr. 2006), pp. 5567–5572. ISSN: 0027-8424, 1091-6490. DOI: 10.1073/pnas.0509425103.
- [3] O-W Merten, C Gény-Fiamma, and A M Douar. "Current issues in adeno-associated viral vector production". In: *Gene Therapy* 12.S1 (Oct. 2005), S51–S61. ISSN: 0969-7128, 1476-5462. DOI: 10.1038/sj.gt.3302615.
- [4] Devin K. Binder, Geoff M. Rau, and Philip A. Starr. "Risk Factors for Hemorrhage during Microelectrode-guided Deep Brain Stimulator Implantation for Movement Disorders". In: *Neurosurgery* 56.4 (Apr. 2005), pp. 722–732. ISSN: 0148-396X, 1524-4040. DOI: 10.1227/01.NEU.0000156473.57196.7E.
- [5] Krystof Bankiewicz, Jamie Eberling, Malgorzata Kohutnicka, William Jagust, Phillip Pivrotto, John Bringas, Janet Cunningham, Thomas Budinger, and Judith Harvey-White. "Convection-enhanced delivery of AAV vector in parkinsonian monkeys; in vivo detection of gene expression and restoration of dopaminergic function using pro-drug approach." In: *Experimental neurology* 164.1 (July 2000), pp. 2–14. ISSN: 0014-4886. DOI: 10.1006/exnr.2000.7408.
- [6] Marina E. Emborg, Valerie Joers, Ronald Fisher, Kevin Brunner, Victoria Carter, Chris Ross, Raghu Raghavan, Martin Brady, James Raschke, Ken Kubota, and Andrew Alexander. "Intraoperative Intracerebral MRI-Guided Navigation for Accurate Targeting in Nonhuman Primates". In: *Cell Transplantation* 19.12 (Dec. 2010), pp. 1587–1597. ISSN: 0963-6897, 1555-3892. DOI: 10.3727/096368910X514323.
- [7] Georges Salamon and JM Corbaz. *Atlas of arteries of the human brain*. Sandoz, 1971.
- [8] Perry E Radau, Stefan Pintilie, Roey Flor, Labonny Biswas, Samuel O Oduneye, Venkat Ramanan, Kevan A Anderson, and Graham A Wright. "VURTIGO: visualization platform for real-time, MRI-guided cardiac Electroanatomic mapping". In: *International Workshop on Statistical Atlases and Computational Models of the Heart*. Springer. 2011, pp. 244–253.

- [9] Ethan K. Brodsky, Walter F. Block, Andy L. Alexander, Marina E. Emborg, Chris D. Ross, and Karl A. Sillay. "Intraoperative device targeting using real-time MRI". In: *Proceedings of the 2011 Biomedical Sciences and Engineering Conference: Image Informatics and Analytics in Biomedicine*. Knoxville, TN, USA: IEEE, Mar. 2011, pp. 1–4. ISBN: 978-1-61284-411-4. DOI: 10.1109/BSEC.2011.5872335.
- [10] Piotr Hadaczek, Yoji Yamashita, Hanna Mirek, Laszlo Tamas, Martha C Bohn, Charles Noble, John W Park, and Krystof Bankiewicz. "The "perivascular pump" driven by arterial pulsation is a powerful mechanism for the distribution of therapeutic molecules within the brain". In: *Molecular Therapy* 14.1 (2006), pp. 69–78.
- [11] Martin L Brady, Raghu Raghavan, Andrew Alexander, Ken Kubota, Karl Sillay, and Marina E Emborg. "Pathways of infusate loss during convection-enhanced delivery into the putamen nucleus". In: *Stereotactic and functional neurosurgery* 91.2 (2013), pp. 69–78.
- [12] Samuel Groeschel, Wui Khean Chong, Robert Surtees, and Folker Hanefeld. "Virchow-Robin spaces on magnetic resonance images: normative data, their dilatation, and a review of the literature". In: *Neuroradiology* 48.10 (2006), pp. 745–754.
- [13] Y-C Zhu, Carole Dufouil, Bernard Mazoyer, A Soumaré, F Ricolfi, Christophe Tzourio, and H Chabriat. "Frequency and location of dilated Virchow-Robin spaces in elderly people: a population-based 3D MR imaging study". In: *American Journal of Neuroradiology* 32.4 (2011), pp. 709–713.
- [14] Robert M Kwee and Thomas C Kwee. "Virchow-Robin spaces at MR imaging". In: *Radiographics* 27.4 (2007), pp. 1071–1086.
- [15] Maria del C. Valdés Hernández, Rory J Piper, Xin Wang, Ian J Deary, and Joanna M Wardlaw. "Towards the automatic computational assessment of enlarged perivascular spaces on brain magnetic resonance images: a systematic review". In: *Journal of Magnetic Resonance Imaging* 38.4 (2013), pp. 774–785.
- [16] Philip A. Starr, Alastair J. Martin, and Paul S. Larson. "Implantation of Deep Brain Stimulator Electrodes Using Interventional MRI". In: *Neurosurgery Clinics of North America* 20.2 (Apr. 2009), pp. 207–217. ISSN: 10423680. DOI: 10.1016/j.nec.2009.04.010.

- [17] Paul S. Larson, Philip A. Starr, Geoffrey Bates, Lisa Tansey, R. Mark Richardson, and Alastair J. Martin. "An Optimized System for Interventional Magnetic Resonance Imaging-Guided Stereotactic Surgery: Preliminary Evaluation of Targeting Accuracy". In: *Operative Neurosurgery* 70.suppl\_1 (Mar. 2012), ons95–ons103. ISSN: 2332-4252, 2332-4260. DOI: 10.1227/NEU.0b013e31822f4a91.
- [18] Philip A. Starr, Leslie C. Markun, Paul S. Larson, Monica M. Volz, Alastair J. Martin, and Jill L. Ostrem. "Interventional MRI-guided deep brain stimulation in pediatric dystonia: first experience with the ClearPoint system: Clinical article". In: *Journal of Neurosurgery: Pediatrics* 14.4 (Oct. 2014), pp. 400–408. ISSN: 1933-0707, 1933-0715. DOI: 10.3171/2014.6.PEDS13605.
- [19] Jill L. Ostrem, Nathan Ziman, Nicholas B. Galifianakis, Philip A. Starr, Marta San Luciano, Maya Katz, Caroline A. Racine, Alastair J. Martin, Leslie C. Markun, and Paul S. Larson. "Clinical outcomes using ClearPoint interventional MRI for deep brain stimulation lead placement in Parkinson's disease". In: *Journal of Neurosurgery* 124.4 (Apr. 2016), pp. 908–916. ISSN: 0022-3085, 1933-0693. DOI: 10.3171/2015.4.JNS15173.
- [20] Zulma Tovar-Spinoza, David Carter, David Ferrone, Yaman Eksioglu, and Sean Huckins. "The use of MRI-guided laser-induced thermal ablation for epilepsy". In: *Child's Nervous System* 29.11 (Nov. 2013), pp. 2089–2094. ISSN: 0256-7040, 1433-0350. DOI: 10.1007/s00381-013-2169-6.
- [21] R. Medvid, A. Ruiz, R.J. Komotar, J.R. Jagid, M.E. Ivan, R.M. Quencer, and M.B. Desai. "Current Applications of MRI-Guided Laser Interstitial Thermal Therapy in the Treatment of Brain Neoplasms and Epilepsy: A Radiologic and Neurosurgical Overview". In: *American Journal of Neuroradiology* 36.11 (Nov. 2015), pp. 1998–2006. ISSN: 0195-6108, 1936-959X. DOI: 10.3174/ajnr.A4362.
- [22] John H. Sampson, Raghu Raghavan, James M. Provenzale, David Croteau, David A. Reardon, R. Edward Coleman, Inmaculada Rodríguez Ponce, Ira Pastan, Raj K. Puri, and Christoph Pedain. "Induction of Hyperintense Signal on T2-Weighted MR Images Correlates with Infusion Distribution from Intracerebral Convection-Enhanced Delivery of a Tumor-Targeted Cytotoxin". In: *American Journal of Roentgenology* 188.3 (Mar. 2007), pp. 703–709. ISSN: 0361-803X, 1546-3141. DOI: 10.2214/AJR.06.0428.
- [23] Ankit I. Mehta, Bryan D. Choi, Raghu Raghavan, Martin Brady, Allan H. Friedman, Darell D. Bigner, Ira Pastan, and John H. Sampson. "Imaging of

- Convection Enhanced Delivery of Toxins in Humans". In: *Toxins* 3.3 (Mar. 2011), pp. 201–206. ISSN: 2072-6651. DOI: 10.3390/toxins3030201.
- [24] Ankit I. Mehta, Bryan D. Choi, Divya Ajay, Raghu Raghavan, Martin Brady, Allan H. Friedman, Ira Pastan, Darell D. Bigner, and John H. Sampson. "Convection Enhanced Delivery of Macromolecules for Brain Tumors". In: *Current Drug Discovery Technologies* 9.4 (Oct. 2012), pp. 305–310. ISSN: 15701638. DOI: 10.2174/157016312803305951.
- [25] Raghu Raghavan, Martin L Brady, and John H Sampson. "Delivering therapy to target: improving the odds for successful drug development". In: *Therapeutic Delivery* 7.7 (July 2016), pp. 457–481. ISSN: 2041-5990, 2041-6008. DOI: 10.4155/tde-2016-0016.
- [26] Adrian P. Kells, R. Mark Richardson, Alastair J. Martin, Chan Moon, Krystof S. Bankiewicz, and Paul S. Larson. "iMRI Guided Neurosurgical Gene Delivery for Parkinson's Disease". In: *Proceedings of the 12th Interventional MRI Symposium*. Boston, Massachusetts, USA, Oct. 2018, p. 3.
- [27] Chadwick W. Christine, Krystof S. Bankiewicz, Amber D. Van Laar, R. Mark Richardson, Bernard Ravina, Adrian P. Kells, Brendon Boot, Alastair J. Martin, John Nutt, Marin E. Thompson, and Paul S. Larson. "Magnetic resonance imaging-guided phase 1 trial of putaminal AADC gene therapy for Parkinson's disease". In: *Annals of Neurology* 85.5 (May 2019), pp. 704–714. ISSN: 0364-5134, 1531-8249. DOI: 10.1002/ana.25450.
- [28] Massimo S. Fiandaca, Vanja Varenika, Jamie Eberling, Tracy McKnight, John Bringas, Phillip Pivrotto, Janine Beyer, Piotr Hadaczek, William Bowers, John Park, Howard Federoff, John Forsayeth, and Krystof S. Bankiewicz. "Real-time MR imaging of adeno-associated viral vector delivery to the primate brain". In: *NeuroImage* 47 (Aug. 2009), T27–T35. ISSN: 10538119. DOI: 10.1016/j.neuroimage.2008.11.012.
- [29] Ernesto A. Salegio, Lluís Samaranch, Adrian P. Kells, John Forsayeth, and Krystof Bankiewicz. "Guided delivery of adeno-associated viral vectors into the primate brain". In: *Advanced Drug Delivery Reviews* 64.7 (May 2012), pp. 598–604. ISSN: 0169409X. DOI: 10.1016/j.addr.2011.10.005.
- [30] Waldy San Sebastian, R. Mark Richardson, Adrian P. Kells, Clementine Lamarre, John Bringas, Philip Pivrotto, Ernesto A. Salegio, Stephen J. DeArmond, John Forsayeth, and Krystof S. Bankiewicz. "Safety and Tolerability of Magnetic Resonance Imaging-Guided Convection-Enhanced Delivery of AAV2-hAADC with a Novel Delivery Platform in Nonhuman Primate Stria-



- tum". In: *Human Gene Therapy* 23.2 (Feb. 2012), pp. 210–217. ISSN: 1043-0342, 1557-7422. DOI: 10.1089/hum.2011.162.
- [31] Ned H. Kalin, Andrew S. Fox, Rothem Kovner, Marissa K. Riedel, Eva M. Fekete, Patrick H. Roseboom, Do P.M. Tromp, Benjamin P. Grabow, Miles E. Olsen, Ethan K. Brodsky, Daniel R. McFarlin, Andrew L. Alexander, Marina E. Emborg, Walter F. Block, Julie L. Fudge, and Jonathan A. Oler. "Overexpressing Corticotropin-Releasing Factor in the Primate Amygdala Increases Anxious Temperament and Alters Its Neural Circuit". In: *Biological Psychiatry* 80.5 (Sept. 2016), pp. 345–355. ISSN: 00063223. DOI: 10.1016/j.biopsych.2016.01.010.
- [32] Charles L. Truwit and Haiying Liu. "Prospective stereotaxy: A novel method of trajectory alignment using real-time image guidance". In: *Journal of Magnetic Resonance Imaging* 13.3 (Mar. 2001), pp. 452–457. ISSN: 1053-1807, 1522-2586. DOI: 10.1002/jmri.1065.
- [33] Ethan K. Brodsky, Miles E. Olsen, Jonathan A. Oler, Andrew S. Fox, Rothem Kovner, Marissa K. Riedel, Eva M. Fekete, Patrick H. Roseboom, Do P.M. Tromp, Benjamin P. Grabow, Julie L. Fudge, Andrew L. Alexander, Marina E. Emborg, Ned H. Kalin, and Walter F. Block. "MRI-Guided Delivery of Viral Vectors for Targeted Alteration of Neurochemistry". In: *Proceedings of the 8th National Image-Guided Therapy Workshop*. Bethesda, Maryland, USA, Mar. 2016, p. 28.
- [34] Walter A. Hall, Haiying Liu, and Charles L. Truwit. "Navigus Trajectory Guide". In: *Neurosurgery* 46.2 (Feb. 2000), pp. 502–504. ISSN: 0148-396X, 1524-4040. DOI: 10.1097/00006123-200002000-00051.
- [35] Scott C. Vermilyea, Jianfeng Lu, Miles Olsen, Scott Guthrie, Yunlong Tao, Eva M. Fekete, Marissa K. Riedel, Kevin Brunner, Carissa Boettcher, Viktorya Bondarenko, Ethan Brodsky, Walter F. Block, Andrew Alexander, Su-Chun Zhang, and Marina E. Emborg. "Real-Time Intraoperative MRI Intracerebral Delivery of Induced Pluripotent Stem Cell-Derived Neurons". In: *Cell Transplantation* 26.4 (Apr. 2017), pp. 613–624. ISSN: 0963-6897, 1555-3892. DOI: 10.3727/096368916X692979.
- [36] Matthew Zammit, Yunlong Tao, Miles E. Olsen, Jeanette Metzger, Scott C. Vermilyea, Kathryn Bjornson, Maxim Slesarev, Walter F. Block, Kerri Fuchs, Sean Phillips, Viktorya Bondarenko, Su-Chun Zhang, Marina E. Emborg, and Bradley T. Christian. "[<sup>18</sup>F]FEPPA PET imaging for monitoring CD68-positive microglia/macrophage neuroinflammation in nonhuman primates".

- In: *EJNMMI Research* 10.1 (Dec. 2020), p. 93. ISSN: 2191-219X. DOI: 10.1186/s13550-020-00683-5.
- [37] Yunlong Tao, Scott C. Vermilyea, Matthew Zammit, Jianfeng Lu, Miles Olsen, Jeanette M. Metzger, Lin Yao, Yuejun Chen, Sean Phillips, James E. Holden, Viktoriya Bondarenko, Walter F. Block, Todd E. Barnhart, Nancy Schultz-Darken, Kevin Brunner, Heather Simmons, Bradley T. Christian, Marina E. Emborg, and Su-Chun Zhang. "Autologous transplant therapy alleviates motor and depressive behaviors in parkinsonian monkeys". In: *Nature Medicine* (Mar. 2021). ISSN: 1078-8956, 1546-170X. DOI: 10.1038/s41591-021-01257-1.
- [38] Andrew S. Fox, Tade Souaiaia, Jonathan A. Oler, Rothem Kovner, Jae Mun (Hugo) Kim, Joseph Nguyen, Delores A. French, Marissa K. Riedel, Eva M. Fekete, Matthew R. Rabska, Miles E. Olsen, Ethan K. Brodsky, Andrew L. Alexander, Walter F. Block, Patrick H. Roseboom, James A. Knowles, and Ned H. Kalin. "Dorsal Amygdala Neurotrophin-3 Decreases Anxious Temperament in Primates". In: *Biological Psychiatry* 86.12 (Dec. 2019), pp. 881–889. ISSN: 00063223. DOI: 10.1016/j.biopsych.2019.06.022.
- [39] Patrick H. Roseboom, Sascha A.L. Mueller, Jonathan A. Oler, Andrew S. Fox, Marissa K. Riedel, Victoria R. Elam, Miles E. Olsen, Juan L. Gomez, Matthew A. Boehm, Alexandra H. DiFilippo, Bradley T. Christian, Michael Michaelides, and Ned H. Kalin. "Evidence in primates supporting the use of chemogenetics for the treatment of human refractory neuropsychiatric disorders". In: *Molecular Therapy* (Apr. 2021), S1525001621002094. ISSN: 15250016. DOI: 10.1016/j.ymthe.2021.04.021.
- [40] user1551. *Point closest to a set four of lines in 3D*. <https://math.stackexchange.com/a/55286>. Online; accessed 24 February 2021. 2011.
- [41] Andriy Fedorov, Reinhard Beichel, Jayashree Kalpathy-Cramer, Julien Finet, Jean-Christophe Fillion-Robin, Sonia Pujol, Christian Bauer, Dominique Jennings, Fiona Fennessy, Milan Sonka, John Buatti, Stephen Aylward, James V. Miller, Steve Pieper, and Ron Kikinis. "3D Slicer as an image computing platform for the Quantitative Imaging Network". In: *Magnetic Resonance Imaging* 30.9 (Nov. 2012), pp. 1323–1341. ISSN: 0730725X. DOI: 10.1016/j.mri.2012.05.001.
- [42] Ron Kikinis, Steve D. Pieper, and Kirby G. Vosburgh. "3D Slicer: A Platform for Subject-Specific Image Analysis, Visualization, and Clinical Support". In: *Intraoperative Imaging and Image-Guided Therapy*. Ed. by Ferenc A. Jolesz.

- New York, NY: Springer New York, 2014, pp. 277–289. ISBN: 978-1-4614-7656-6 978-1-4614-7657-3. DOI: 10.1007/978-1-4614-7657-3\_19.
- [43] Andreas Reichert, Michael Bock, Michael Vogele, and Axel Joachim Krafft. “GantryMate: A Modular MR-Compatible Assistance System for MR-Guided Needle Interventions”. In: *Tomography* 5.2 (June 2019), pp. 266–273. ISSN: 2379-139X. DOI: 10.18383/j.tom.2019.00007.
- [44] Prashant Chittiboina, John D. Heiss, and Russell R. Lonser. “Accuracy of direct magnetic resonance imaging-guided placement of drug infusion canulae”. In: *Journal of Neurosurgery* 122.5 (May 2015), pp. 1173–1179. ISSN: 0022-3085, 1933-0693. DOI: 10.3171/2014.11.JNS131888.
- [45] Miles E. Olsen, Scott C. Vermilyea, Jianfeng Lu, Ethan K. Brodsky, Scott Guthrie, Yunlong Tao, Eva M. Fekete, Marissa K. Riedel, Kevin Brunner, Carissa Boettcher, Viktorya Bondarenko, Andrew L. Alexander, Su-Chun Zhang, Marina E. Emborg, and Walter F. Block. “Targeted Delivery of Stem Cells to the Brain using Real Time Interventional MRI”. In: *Proceedings of the 25th Annual Meeting of the International Society for Magnetic Resonance in Medicine*. Honolulu, Hawaii, USA, Apr. 2017, p. 0738.
- [46] J. D. Clark, G. F. Gebhart, J. C. Gonder, M. E. Keeling, and D. F. Kohn. “The 1996 Guide for the Care and Use of Laboratory Animals”. In: *ILAR Journal* 38.1 (Jan. 1997), pp. 41–48. ISSN: 1084-2020. DOI: 10.1093/ilar.38.1.41.
- [47] Andrew S. Fox and Ned H. Kalin. “A Translational Neuroscience Approach to Understanding the Development of Social Anxiety Disorder and Its Pathophysiology”. In: *American Journal of Psychiatry* 171.11 (Nov. 2014), pp. 1162–1173. ISSN: 0002-953X, 1535-7228. DOI: 10.1176/appi.ajp.2014.14040449.
- [48] Rothem Kovner, Jonathan A. Oler, and Ned H. Kalin. “Cortico-Limbic Interactions Mediate Adaptive and Maladaptive Responses Relevant to Psychopathology”. In: *American Journal of Psychiatry* 176.12 (Dec. 2019), pp. 987–999. ISSN: 0002-953X, 1535-7228. DOI: 10.1176/appi.ajp.2019.19101064.
- [49] Xiaomin Su, Adrian P Kells, Ernesto Aguilar Salegio, R Mark Richardson, Piotr Hadaczek, Janine Beyer, John Bringas, Philip Pivrotto, John Forsayeth, and Krystof S Bankiewicz. “Real-time MR Imaging With Gadoteridol Predicts Distribution of Transgenes After Convection-enhanced Delivery of AAV2 Vectors”. In: *Molecular Therapy* 18.8 (Aug. 2010), pp. 1490–1495. ISSN: 15250016. DOI: 10.1038/mt.2010.114.

- [50] Vivek Sudhakar, Amin Mahmoodi, John R. Bringas, Jerusha Naidoo, Adrian Kells, Lluís Samaranch, Massimo S. Fiandaca, and Krystof S. Bankiewicz. “Development of a novel frameless skull-mounted ball-joint guide array for use in image-guided neurosurgery”. In: *Journal of Neurosurgery* 132.2 (Feb. 2020). Published online February 15, 2019; DOI: 10.3171/2018.10.JNS182169., pp. 595–604. ISSN: 0022-3085, 1933-0693. DOI: 10.3171/2018.10.JNS182169.
- [51] Krystof S. Bankiewicz, Tomasz Pasterski, Daniel Kreatsoulas, Jakub Onikijuk, Krzysztof Mozgiel, Vikas Munjal, J. Bradley Elder, Russell R. Lonser, and Mirosław Zabek. “Use of a novel ball-joint guide array for magnetic resonance imaging-guided cannula placement and convective delivery: technical note”. In: *Journal of Neurosurgery* (Oct. 2020), pp. 1–7. ISSN: 0022-3085, 1933-0693. DOI: 10.3171/2020.6.JNS201564.
- [52] R. Mark Richardson, Adrian P. Kells, Alastair J. Martin, Paul S. Larson, Philip A. Starr, Peter G. Piferi, Geoffrey Bates, Lisa Tansey, Kathryn H. Rosenbluth, John R. Bringas, Mitchel S. Berger, and Krystof S. Bankiewicz. “Novel Platform for MRI-Guided Convection-Enhanced Delivery of Therapeutics: Preclinical Validation in Nonhuman Primate Brain”. In: *Stereotactic and Functional Neurosurgery* 89.3 (2011), pp. 141–151. ISSN: 1423-0372, 1011-6125. DOI: 10.1159/000323544.
- [53] Science Museum Group. *Arc for Leksell Stereotactic System*. <https://collection.sciencemuseumgroup.org.uk/objects/co503282/arc-for-leksell-stereotactic-system-sweden-1992-1999-stereotaxic-apparatus>. Online; Accessed March 19, 2021. 1997.
- [54] Bohan Wang, George Matcuk, and Jernej Barbic. *Hand MRI dataset*. University of Southern California. <http://www.jernejbarbic.com/hand-mri-dataset>. Online; accessed 17 November 2021. 2020.
- [55] George Paxinos, Michael Petrides, Xu-Feng Huang, and Arthur W. Toga. *The Rhesus Monkey Brain: in Stereotaxic Coordinates*. 2nd ed. OCLC: 845195997. Amsterdam: Elsevier, Acad. Press, 2009. ISBN: 978-0-12-373619-2 978-0-12-373620-8.
- [56] Brian B. Avants, Nicholas J. Tustison, Gang Song, Philip A. Cook, Arno Klein, and James C. Gee. “A reproducible evaluation of ANTs similarity metric performance in brain image registration”. In: *NeuroImage* 54.3 (Feb. 2011), pp. 2033–2044. ISSN: 10538119. DOI: 10.1016/j.neuroimage.2010.09.025.

- [57] Daniel F Hanley, Richard E Thompson, John Muschelli, Michael Rosenblum, Nichol McBee, Karen Lane, Amanda J Bistran-Hall, Steven W Mayo, Penelope Keyl, Dheeraj Gandhi, et al. "Safety and efficacy of minimally invasive surgery plus alteplase in intracerebral haemorrhage evacuation (MISTIE): a randomised, controlled, open-label, phase 2 trial". In: *The Lancet Neurology* 15.12 (2016), pp. 1228–1237.
- [58] Daniel F Hanley, Richard E Thompson, Michael Rosenblum, Gayane Yenokyan, Karen Lane, Nichol McBee, Steven W Mayo, Amanda J Bistran-Hall, Dheeraj Gandhi, W Andrew Mould, et al. "Efficacy and safety of minimally invasive surgery with thrombolysis in intracerebral haemorrhage evacuation (MISTIE III): a randomised, controlled, open-label, blinded endpoint phase 3 trial". In: *The Lancet* 393.10175 (2019), pp. 1021–1032.